

# Flexible and efficient spatial extremes emulation via variational autoencoders

Likun Zhang, Xiaoyu Ma, Christopher K. Wikle

Department of Statistics, University of Missouri

and

Raphaël Huser

Statistics Program, Computer, Electrical and Mathematical Sciences and Engineering (CEMSE) Division, King Abdullah University of Science and Technology (KAUST)

May 13, 2024

## Abstract

Many real-world processes have complex tail dependence structures that cannot be characterized using classical Gaussian processes. More flexible spatial extremes models exhibit appealing extremal dependence properties but are often exceedingly prohibitive to fit and simulate from in high dimensions. In this paper, we aim to push the boundaries on computation and modeling of high-dimensional spatial extremes via integrating a new spatial extremes model that has flexible and non-stationary dependence properties in the encoding-decoding structure of a variational autoencoder called the XVAE. The XVAE can emulate spatial observations and produce outputs that have the same statistical properties as the inputs, especially in the tail. Our approach also provides a novel way of making fast inference with complex extreme-value processes. Through extensive simulation studies, we show that our XVAE is substantially more time-efficient than traditional Bayesian inference while outperforming many spatial extremes models with a stationary dependence structure. Lastly, we analyze a high-resolution satellite-derived dataset of sea surface temperature in the Red Sea, which includes 30 years of daily measurements at 16703 grid cells. We demonstrate how to use XVAE to identify regions susceptible to marine heatwaves under climate change and examine the spatial and temporal variability of the extremal dependence structure.

*Keywords:* Variational Bayes, Deep learning, Spatial extremes, Tail dependence, Climate emulation

Emulating large spatial datasets is very valuable in producing a large ensemble of realistic replicates, quantifying uncertainty of various inference targets, and assessing risks associated with rare events such as joint high-threshold exceedances (Arpat and Caers, 2007). The efficacy of an emulator hinges greatly on its ability to characterize complex patterns of spatial variability in the studied phenomenon, especially the dependence structure in the tail. However, handling statistical computations for spatial models accommodating extremes remains a significant challenge for large datasets (Huser and Wadsworth, 2022).

Spatial emulation is particularly useful in climate science, where an abundance of simulations with high regional resolutions is often needed for detailed field-level insights and for uncertainty quantification (UQ). For example, watershed modeling (e.g., Sharma et al., 2021) requires a great number of simulations of heavy precipitation to assess regional riverine flood inundation hazards. In addition, numerous high-resolution sea surface temperature (SST) field replicates can aid in the identification of marine heatwaves (MHW) and the detection of coral reef zones prone to bleaching (Hughes et al., 2017). Current MHW detection methods, as described in Geneviev et al. (2019), involve spatial averaging over predefined regions with extensive coral bleaching records, followed by calculating a daily percentile threshold using an 11-day window around the date of interest. To avoid relying on predefined subdomains or spatial averaging, we need a refined methodology to enhance the accuracy of spatial threshold exceedance estimations with better UQ.

Furthermore, emulators can be used as surrogate models to speed up and simplify mechanic-based deterministic models such as Earth system models (ESMs). These models typically rely on deterministic partial differential equations, featuring numerous parameters and requiring significant computational resources. In recent years, surrogate models have proven to produce realistic synthetic data with much less computational expense (see Gramacy, 2020, for an overview). They are also useful for inverse problems, model calibration and the specification of realistic model parameterizations for coupled processes.

However, traditional methods for emulation such as those based on Gaussian processes (e.g., Gu et al., 2018), polynomial chaos expansions (e.g., Sargsyan, 2017), proper orthogonal decomposition (e.g., Iuliano and Quagliarella, 2013) and more recently, deep neural networks used in generative models such as generative adversarial networks (Goodfellow et al., 2014, GANs) and variational autoencoders (Kingma and Welling, 2013, VAEs), do not naturally accommodate extreme values, and certainly not dependent extreme values.

Classical asymptotic max-stable processes exhibit dependence structures that are too rigid for environmental datasets and thus lead to overestimation of the spatial extent and intensity of extreme events (Huser et al., 2024). Recent spatial extremes models have addressed some of these limitations and offer more realistic tail dependence structures. Examples of such models include Gaussian scale mixtures (e.g., Opitz, 2016; Huser and Wadsworth, 2019) or  $r$ -Pareto processes (e.g., Thibaud and Opitz, 2015; de Fondeville and Davison, 2018), applied in the peaks-over-threshold framework, and max-infinitely divisible (max-id) models (e.g., Reich and Shaby, 2012; Padoan, 2013; Huser et al., 2021; Bopp et al., 2021; Zhong et al., 2022), applied in the block-maxima framework. However, these models often assume a stationary dependence structure across space and time, and the computational demands are significant even for moderately-sized datasets (up to about 500

locations; Zhang et al., 2022), limiting the applicability to high-resolution climate datasets.

In this work, we adopt a statistics-of-extremes perspective (Davison and Huser, 2015) and introduce a novel max-id model for spatial extremes with nonstationary dependence properties over space and time to explicitly accommodate concurrent and locally dependent extremes. We provide a detailed proof of these properties and propose embedding this flexible spatial extremes model within a variational autoencoder engine, referred to as the XVAE. This surrogate modeling framework facilitates rapid and efficient spatial modeling and data emulation in dimensions never explored before for dependent extremes. Moreover, we present a validation framework with wide applicability to assess emulation quality across low, moderate, and high values. A novel metric with theoretical guarantees is proposed, specifically tailored to evaluate the skill of a spatial model in fitting joint tail behavior.

The paper proceeds as follows. First, in Section 1, we detail how our novel max-id process can be embedded into the encoder-decoder VAE construction and study its highly flexible extremal dependence properties. Next, in Section 2, we introduce several model evaluation approaches to assess the emulation of spatial fields with dependent extremes. In Section 3, we validate the emulating power of our XVAE by simulation and demonstrate its advantages over a commonly used Gaussian process emulator. Then, in Section 4, we apply our XVAE to high-resolution Red Sea surface temperature extremes. Lastly, in Section 5, we conclude the paper and discuss perspectives for future work.

## 1 Methodology

This section provides background on VAEs, a presentation of our novel max-id model for spatial extremes, and a description of the construction of our XVAE. A detailed discussion on the tail properties of the model is also included. Hereafter, we shall denote random variables with capital letters and fixed or observed quantities with lowercase letters.

### 1.1 Variational autoencoder background

Bayesian hierarchical models characterized by a lower-dimensional latent process are amenable to use of the variational autoencoder for inference and generative simulation. Specifically, consider the joint distribution

$$p_{\theta}(\mathbf{x}, \mathbf{z}) = p_{\theta}(\mathbf{x} \mid \mathbf{z})p_{\theta}(\mathbf{z}),$$

where  $\mathbf{x}$  and  $\mathbf{z}$  are observations of a (e.g., physical) process  $\mathbf{X} \in \mathbb{R}^{n_s}$  and realizations of a latent process  $\mathbf{Z} \in \mathbb{R}^K$ , respectively, and  $K \ll n_s$ . The data model  $p_{\theta}(\mathbf{x} \mid \mathbf{z})$  and the latent process model  $p_{\theta}(\mathbf{z})$  may depend on different subsets of parameters  $\theta$ . In the case of spatial data, the vector  $\mathbf{X}$  may be observations of a spatial process  $\{X(\mathbf{s}) : \mathbf{s} \in \mathcal{S}\}$  at  $n_s$  locations, and  $\mathbf{Z}$  may be random coefficients from a low-rank basis expansion representation of  $\mathbf{X}$ . To emulate an observed high-dimensional data  $\mathbf{x}$  (i.e., generate new realizations of  $\mathbf{X}$ ), an ideal probabilistic framework would be to: (1) obtain a good estimate  $\hat{\theta}$  of the parameters

$\theta$  given the observations  $\mathbf{x}$  and generate independent (latent) variables  $\mathbf{Z}^1, \dots, \mathbf{Z}^L$  from the posterior density  $p_{\hat{\theta}}(\mathbf{z} | \mathbf{x})$ ; (2) generate  $\mathbf{X}^l$  from the data model (posterior predictive distributions)  $p_{\hat{\theta}}(\mathbf{x} | \mathbf{Z}^l)$ ,  $l = 1, \dots, L$ . If the characterization of the distributions is reasonable, the resulting emulated replicates  $\{\mathbf{X}^1, \dots, \mathbf{X}^L\}$  should resemble the original input  $\mathbf{x}$ , with meaningful variations among the emulated samples.

Unfortunately, the posterior density  $p_{\theta}(\mathbf{z} | \mathbf{x})$  is often intractable because the marginal likelihood  $p_{\theta}(\mathbf{x}) = \int p_{\theta}(\mathbf{x}, \mathbf{z})d\mathbf{z}$ , a  $K$ -dimensional integral, typically does not have an analytical form. This makes the maximum likelihood estimation of the parameters  $\theta$  difficult even for a moderately complicated data model  $p_{\theta}(\mathbf{x} | \mathbf{z})$ . Imposing another prior model on  $\theta$  and implementing a Markov chain Monte Carlo (MCMC) algorithm to draw samples of  $(\mathbf{Z}, \theta)$  simultaneously can be a possible solution; the draws of  $\mathbf{Z}$  from the Markov chain are treated as the samples from  $p_{\theta}(\mathbf{z} | \mathbf{x})$  which can then be fed in  $p_{\theta}(\mathbf{x} | \mathbf{z})$  to generate new  $\mathbf{X}$ . But MCMC can be computationally intensive when the likelihood  $p_{\theta}(\mathbf{x}, \mathbf{z})$  is expensive to evaluate, and algorithm tuning can be challenging when the dimension of  $(\mathbf{Z}, \theta)$  is large, particularly in the case of complex spatial and/or temporal dependence in the data.

In variational Bayesian inference, the true posterior  $p_{\theta}(\mathbf{z} | \mathbf{x})$  is approximated by a so-called variational distribution that is relatively easy to evaluate. The variational autoencoder (VAE) proposed by Kingma and Welling (2013) formulates the variational distribution (which they call a probabilistic *encoder*) as a multilayer perceptron (MLP) neural network denoted by  $q_{\phi_e}(\mathbf{z} | \mathbf{x})$ , in which  $\mathbf{x}$  is the input,  $\mathbf{z}$  is the output and  $\phi_e$  are the so-called weights and biases of the neural network. This construction greatly facilitates fast non-linear encoding of a high-dimensional process  $\mathbf{X}$  to lower-dimensional  $\mathbf{Z}$  in the latent space. Next, to generate emulated data replicates from  $p_{\theta}(\mathbf{x} | \mathbf{Z})$ , Kingma and Welling (2013) use another MLP neural network (which they call a probabilistic *decoder*) acting as an estimator for the model parameters  $\theta$ . Denoting the weights and biases of the decoder by  $\phi_d$ , we write  $\hat{\theta}_{\text{NN}} = \text{DecoderNeuralNet}_{\phi_d}(\mathbf{z})$  and denote through an abuse of notation

$$p_{\phi_d}(\mathbf{x}, \mathbf{z}) \equiv p_{\hat{\theta}_{\text{NN}}}(\mathbf{x}, \mathbf{z}), \quad p_{\phi_d}(\mathbf{x}) \equiv \int p_{\hat{\theta}_{\text{NN}}}(\mathbf{x}, \mathbf{z})d\mathbf{z},$$

and  $p_{\phi_d}(\mathbf{z} | \mathbf{x}) = p_{\phi_d}(\mathbf{x}, \mathbf{z})/p_{\phi_d}(\mathbf{x})$ .

The encoding parameters  $\phi_e$  and decoding parameters  $\phi_d$  can be estimated by maximizing the evidence lower bound (ELBO), which is defined by

$$\mathcal{L}_{\phi_e, \phi_d}(\mathbf{x}) = \log p_{\phi_d}(\mathbf{x}) - D_{KL} \{q_{\phi_e}(\mathbf{z} | \mathbf{x}) || p_{\phi_d}(\mathbf{z} | \mathbf{x})\}, \quad (1)$$

in which  $\log p_{\phi_d}(\mathbf{x})$  is called the *evidence* for  $\mathbf{x}$  under  $\hat{\theta}_{\text{NN}}$ , and the second term in (1) is the Kullback–Leibler (KL) divergence between  $q_{\phi_e}(\mathbf{z} | \mathbf{x})$  and  $p_{\phi_d}(\mathbf{z} | \mathbf{x})$ , which is non-negative. Therefore, maximizing the ELBO with respect to  $\phi_e$  and  $\phi_d$  is equivalent to maximizing the log-likelihood  $\log p_{\phi_d}(\mathbf{x})$  while minimizing the difference between the approximate posterior density  $q_{\phi_e}(\mathbf{z} | \mathbf{x})$  and the true posterior density  $p_{\phi_d}(\mathbf{z} | \mathbf{x})$  (under  $\hat{\theta}_{\text{NN}}$ ).



Since  $p_{\phi_d}(\mathbf{z} \mid \mathbf{x})$  is unknown, we rewrite the marginal likelihood  $p_{\phi_d}(\mathbf{x})$  as follows

$$\log p_{\phi_d}(\mathbf{x}) = \mathbb{E}_{\mathbf{Z} \sim q_{\phi_e}(\mathbf{z} \mid \mathbf{x})} \left\{ \log \frac{p_{\phi_d}(\mathbf{x}, \mathbf{Z})}{q_{\phi_e}(\mathbf{Z} \mid \mathbf{x})} \right\} + D_{KL} \{q_{\phi_e}(\mathbf{z} \mid \mathbf{x}) \parallel p_{\phi_d}(\mathbf{z} \mid \mathbf{x})\}.$$

Therefore, the ELBO can be approximated by Monte Carlo as

$$\mathcal{L}_{\phi_e, \phi_d}(\mathbf{x}) \approx \frac{1}{L} \sum_{l=1}^L \log \frac{p_{\phi_d}(\mathbf{x}, \mathbf{Z}^l)}{q_{\phi_e}(\mathbf{Z}^l \mid \mathbf{x})}, \quad (2)$$

where  $\mathbf{Z}^1, \dots, \mathbf{Z}^L$  are independent draws from  $q_{\phi_e}(\cdot \mid \mathbf{x})$ . If there are replicates of the process,  $\mathbf{x}_1, \dots, \mathbf{x}_{n_t}$ , then  $\sum_{t=1}^{n_t} \mathcal{L}_{\phi_e, \phi_d}(\mathbf{x}_t)$  is considered. In traditional VAEs (e.g., [Kingma et al., 2019](#); [Cartwright et al., 2023](#)), Gaussianity is assumed for both the data model  $p_{\phi_d}(\mathbf{x}_t \mid \mathbf{z}_t)$  and the encoder  $q_{\phi_e}(\mathbf{z}_t \mid \mathbf{x}_t)$ , with the prior  $p_{\phi_d}(\mathbf{z}_t)$  often set as a simple multivariate normal distribution  $N(\mathbf{0}, \mathbf{I}_K)$ . However, the Gaussian assumptions limit the VAE's ability to capture heavy-tailed distributions and intricate dependence structures.

## 1.2 A nonstationary max-id model for VAE-based emulation

To better emulate spatial data with extremes, we define  $p_{\theta}(\mathbf{x} \mid \mathbf{z})$  indirectly through the construction of a novel flexible nonstationary spatial extremes model that can easily be incorporated into a VAE. The flexible spatial extremes model is described in Section 1.2.1, followed by a detailed description the XVAE in Section 1.2.2. Note that implementation details related to the XVAE neural networks are provided in the Supplementary Material.

### 1.2.1 Flexible nonstationary max-id spatial extremes model

Our model builds upon the max-id process introduced by [Reich and Shaby \(2012\)](#) and extended by [Bopp et al. \(2021\)](#). Importantly, a novel extension of our model is its ability to realistically capture both short-range asymptotic dependence (AD), mid-range asymptotic independence (AI), and long-range exact independence, as explained in more detail in Section 1.3, and it can accommodate nonstationary in space and time. As in these earlier works, we start by defining the spatial observation model as

$$X(\mathbf{s}) = \epsilon(\mathbf{s})Y(\mathbf{s}), \quad \mathbf{s} \in \mathcal{S}, \quad (3)$$

where  $\mathcal{S} \in \mathbb{R}^2$  is the domain of interest and  $\epsilon(\mathbf{s})$  is a noise process with independent Fréchet(0,  $\tau$ ,  $1/\alpha_0$ ) marginal distributions; that is,  $\Pr\{\epsilon(\mathbf{s}) \leq x\} = \exp\{-(x/\tau)^{1/\alpha_0}\}$ , where  $x > 0$ ,  $\tau > 0$  and  $\alpha_0 > 0$ . Then,  $Y(\mathbf{s})$  is constructed using a low-rank representation:

$$Y(\mathbf{s}) = \left\{ \sum_{k=1}^K \omega_k(\mathbf{s})^{\frac{1}{\alpha}} Z_k \right\}^{\alpha_0}, \quad (4)$$

where  $\alpha \in (0, 1)$ ,  $\{\omega_k(\mathbf{s}) : k = 1, \dots, K\}$  are fixed compactly-supported radial basis functions centered at  $K$  pre-specified knots such that  $\sum_{k=1}^K \omega_k(\mathbf{s}) = 1$  for any  $\mathbf{s} \in \mathcal{S}$ , and  $\{Z_k : k = 1, \dots, K\}$  are latent variables independently distributed as exponentially-tilted positive-stable (PS) random variables (Hougaard, 1986). We write  $Z_k \stackrel{\text{ind}}{\sim} \text{expPS}(\alpha, \gamma_k)$ ,  $k = 1, \dots, K$ , in which  $\alpha \in (0, 1)$  determines the rate at which the power-law tail of  $\text{expPS}(\alpha, 0)$  tapers off, and the tilting parameters  $\gamma_k \geq 0$  determine the extent of tilting, with larger values of  $\gamma_k$  leading to lighter-tailed  $Z_k$  (see Section B.1 of the Supplementary Material).

Our model, inspired by Reich and Shaby (2012) and Bopp et al. (2021), presents a novel class of spatial extremes models. In Reich and Shaby (2012) and Bopp et al. (2021), the basis functions lack compact support and all tilting parameters are fixed at either  $\gamma_k \equiv 0$  or  $\gamma_k \equiv \gamma > 0$ , resulting in only AI or AD for all pairs of locations, respectively. In contrast, the use of compactly-supported basis function and spatially-varying tilting parameters creates a spatial-scale aware extremal dependence model, enabling local asymptotic dependence (AD) or asymptotic independence (AI) for nearby locations while ensuring long-range AI for distant locations, which is a significant advancement in spatial extremes.

Moreover, while both previous works use a noise process with Fréchet(0, 1, 1/α) marginals (i.e.,  $\alpha_0 = \alpha$ ), our approach decouples noise variance from tail heaviness, providing better noise control for each time point, while keep the appealing property of being max-id as shown below in Section 1.3. Additionally, we embed our model in a VAE, leveraging variational-Bayes-based parameter estimation for rapid computation, modeling, and emulation of high-dimensional spatial extremes (on the order of more than 10,000 locations) without distributing the model parameter estimation over a number of subdomains. Furthermore, we allow different concentration parameters  $\alpha_t$  and tilting parameters  $\gamma_t = \{\gamma_{kt} : k = 1, \dots, K\}$ , at different time points  $t = 1, \dots, n_t$ , which automatically ensures a temporally non-stationary spatial extremes model.

To the best of our knowledge, our XVAE is the first attempt to capture both spatially and temporally varying extremal dependence structures simultaneously in one model at the scale that we consider here. Zhong et al. (2022) achieved it at a much smaller scale and using a quite rigid covariate-based approach. In Section A of the Supplementary Material, we compare our max-id model with other existing models more in depth.

### 1.2.2 XVAE: A VAE incorporating the proposed max-id spatial model

For notational simplicity hereafter, we denote by  $\mathbf{X}_t = \{X_t(\mathbf{s}_j) : j = 1, \dots, n_s\}$  the observations of process (3) at time  $t = 1, \dots, n_t$ , and by  $\mathbf{Z}_t = \{Z_{kt} : k = 1, \dots, K\}$  the corresponding latent variables.

Inference for our flexible extremes model on large spatial datasets poses challenges. A streamlined Metropolis–Hastings MCMC algorithm would be time-consuming and hard to monitor when confronted with the scale of our spatial data in Section 4, where a considerable number of local basis functions  $K$  is necessary to capture intricate local extremes accurately. Additionally, when there are many time replicates, inferring the parameters  $(\alpha_t, \gamma_t, \mathbf{Z}_t)$  for all time points becomes extremely challenging. Moreover, with a large sample size  $n_s$ , evaluating the likelihood  $p_\theta(\mathbf{x} \mid \mathbf{z})$  for a single iteration becomes computationally expensive,

and updating different parameters iteratively further exacerbates this issue. To overcome these challenges, we employ the encoding-decoding VAE paradigm described in Section 1.1 and modify it to account for our extremes framework. For  $t = 1, \dots, n_t$ , our encoder  $q_{\phi_e}(\mathbf{z}_t | \mathbf{x}_t)$  maps each observed replicate  $\mathbf{x}_t$  to the latent space and allows fast random sampling of  $\{\mathbf{Z}_t^1, \dots, \mathbf{Z}_t^L\}$  that will be approximately distributed according to the true posterior  $p_{\theta_t}(\cdot | \mathbf{x}_t)$  because of the ELBO regularization, in which  $\theta_t = (\alpha_0, \tau, \alpha_t, \gamma_t^T)^T$ ; recall Eqs. (1) and (2). The details of this approach are provided below.

**Approximate Posterior/Encoder ( $q_{\phi_e}(\mathbf{z}_t | \mathbf{x}_t)$ ):** The encoder is defined through

$$\begin{aligned} \mathbf{z}_t &= \boldsymbol{\mu}_t + \boldsymbol{\zeta}_t \odot \boldsymbol{\eta}_t, \\ \eta_{kt} &\stackrel{\text{i.i.d.}}{\sim} \text{Normal}(0, 1), \\ (\boldsymbol{\mu}_t^T, \log \boldsymbol{\zeta}_t^T)^T &= \text{EncoderNeuralNet}_{\phi_e}(\mathbf{x}_t), \end{aligned} \quad (5)$$

where we use a standard reparameterization trick with an auxiliary variable  $\boldsymbol{\eta}_t = \{\eta_{kt} : k = 1, \dots, K\}$  and  $\odot$  is the elementwise product (Kingma and Welling, 2013). This trick enables fast computation of Monte Carlo estimates of  $\nabla_{\phi_e} \mathcal{L}_{\phi_e, \phi_d}$ , the gradient of the ELBO with respect to  $\phi_e$  (see Section D.1 for details). Also, by controlling the mean  $\boldsymbol{\mu}_t$  and variance  $\boldsymbol{\zeta}_t^2$ , the distributions  $q_{\phi_e}(\mathbf{z}_t | \mathbf{x}_t)$  are enforced to be close to  $p_{\phi_d}(\mathbf{z}_t | \mathbf{x}_t)$  for each  $t$ . This is the primary role of the deep neural network in (5) — i.e., to learn the complex relationship between the inputs  $\mathbf{x}_t$  and the latent process,  $\mathbf{z}_t$ . The specific neural network architecture and implementation details are given in Section D of the Supplementary Material.

**Prior on Latent Process ( $p_{\phi_d}(\mathbf{z}_t)$ ):** This is determined by our model construction. Specifically, denoting the density function of the expPS( $\alpha, \gamma_k$ ) distribution by  $h(z; \alpha, \gamma_k)$ , the prior on  $\mathbf{z}_t$  can be written as

$$p_{\phi_d}(\mathbf{z}_t) = \prod_{k=1}^K h(z_{kt}; \alpha_t, \gamma_{kt}), \quad (6)$$

which depends on parameters  $(\alpha_t, \gamma_{kt} : t = 1, \dots, T; k = 1, \dots, K)$ .

**Data Model/Decoder ( $p_{\phi_d}(\mathbf{x}_t | \mathbf{z}_t)$ ):** Our decoder is based on the flexible max-id spatial extremes model described in Section 1.2.1. Specifically, recall from Eq. (4) that  $\Pr(\mathbf{X}_t \leq \mathbf{x}_t | \mathbf{Z}_t = \mathbf{z}_t) = \exp\{-\sum_{j=1}^{n_s} (\tau/x_{jt})^{1/\alpha_0} \sum_{k=1}^K \omega_{kj}^{1/\alpha_t} z_{kt}\}$ . Differentiating this conditional distribution function gives the exact form of the decoder:

$$p_{\phi_d}(\mathbf{x}_t | \mathbf{z}_t) = \left(\frac{1}{\alpha_0}\right)^{n_s} \left\{ \prod_{j=1}^{n_s} \frac{1}{x_{jt}} \left(\frac{x_{jt}}{\tau y_{jt}}\right)^{-1/\alpha_0} \right\} \exp\left\{-\sum_{j=1}^{n_s} \left(\frac{x_{jt}}{\tau y_{jt}}\right)^{-1/\alpha_0}\right\}, \quad (7)$$

where  $y_{jt} = \sum_{k=1}^K \omega_{kj}^{1/\alpha_t} z_{kt}$ . This distribution depends on the Fréchet parameters  $(\alpha_0, \tau)^T$  and the dependence parameters  $(\alpha_t, \boldsymbol{\gamma}_t^T)^T$  inherited from the prior distribution of  $\mathbf{z}_t$ . The

decoder neural network estimates these dependence parameters as

$$(\hat{\alpha}_t, \hat{\gamma}_t^T)^T = \text{DecoderNeuralNet}_{\phi_{d,0}}(\mathbf{Z}_t) \quad (8)$$

where  $\phi_{d,0}$  are the bias and weight parameters of this neural network (see Eqs. (D.1) and (D.3) of the Supplementary Material for more details). Combining  $\phi_{d,0}$  with the Fréchet parameters  $(\alpha_0, \tau)^T$ , we write  $\phi_d = (\alpha_0, \tau, \phi_{d,0}^T)^T$ . We must use the variational procedure to find estimates of parameters  $\phi_d$  and the encoder neural network parameters,  $\phi_e$ .

**Encoder/Decoder Estimation:** By drawing  $L$  independent samples  $\mathbf{Z}_t^1, \dots, \mathbf{Z}_t^L$  using Eq. (5), we can derive the Monte Carlo estimate of the ELBO,  $\mathcal{L}_{\phi_e, \phi_d}(\mathbf{x}_t)$ , as in Eq. (2). In Section D.3 of the Supplementary Material, we detail the stochastic gradient search used to find the  $\phi_e$  and  $\phi_d$  that maximize  $\sum_{t=1}^{n_t} \mathcal{L}_{\phi_e, \phi_d}(\mathbf{x}_t)$ . We stress that our XVAE is an example of “amortized inference” (Zammit-Mangion et al., 2024): there is a substantial training cost up front, but once the XVAE is trained, posterior simulation of new latent variables  $\mathbf{Z}_t$  can be performed very efficiently following Eq. (5) and synthetic data can be generated extremely quickly by passing them through the decoder (8) and sampling from the model  $p_{\hat{\theta}_t}(\mathbf{x} | \mathbf{Z}_t)$  specified by Eqs. (3) and (4), in which  $\hat{\theta}_t = (\hat{\alpha}_0, \hat{\tau}, \hat{\alpha}_t, \hat{\gamma}_t^T)^T$ .

The data reconstruction process relies on compactly supported local basis functions at pre-determined knot points, which are not updated with  $\phi_d$  of the decoder. Although one could choose the knots using a certain space-filling design, we propose a data-driven way to determine the number of knots, their locations, and the radius of basis functions as described in Section D.2 of the Supplementary Material, and show by simulation that this compares favorably to the XVAE initialized with the true knots/radii. Our XVAE implementation in R is publicly accessible on GitHub at <https://github.com/likun-stat/XVAE>.

### 1.3 Marginal and dependence properties

One major advantage of our approach over typical machine learning generative models is that we can explicitly derive the marginal and dependence properties of our spatial extremes model integrated within the VAE. In this section, we temporarily omit the subscript  $t$  and examine the marginal and joint tail behavior of the model (3) at one specific time point. For notational simplicity, we write  $X_j = X(\mathbf{s}_j)$ ,  $\omega_{kj} = \omega_k(\mathbf{s}_j)$ ,  $k = 1, \dots, K$ ,  $j = 1, \dots, n_s$ , and define  $\mathcal{C}_j = \{k : \omega_{kj} \neq 0, k = 1, \dots, K\}$ . We require that any location  $\mathbf{s} \in \mathcal{S}$  be covered by at least one basis function, thereby  $\mathcal{C}_j$  cannot be empty for any  $j$ .

In spatial extremes, extremal dependence is commonly described by the measure

$$\chi_{ij}(u) = \Pr\{F_j(X_j) > u \mid F_i(X_i) > u\} = \frac{\Pr\{F_j(X_j) > u, F_i(X_i) > u\}}{\Pr\{F_i(X_i) > u\}} \in [0, 1], \quad (9)$$

in which  $u \in (0, 1)$  is a (high) threshold and  $F_i$  and  $F_j$  are the continuous marginal distribution functions for  $X_i$  and  $X_j$ , respectively. When  $u$  is close to one,  $\chi_{ij}(u)$  quantifies the probability that one variable is extreme given that the other variable is similarly extreme. If  $\chi_{ij} = \lim_{u \rightarrow 1} \chi_{ij}(u) = 0$ ,  $X_i$  and  $X_j$  are said to be *asymptotically independent* (AI), and

if  $\chi_{ij} = \lim_{u \rightarrow 1} \chi_{ij}(u) > 0$ ,  $X_i$  and  $X_j$  are *asymptotically dependent* (AD).

### 1.3.1 Marginal distributions

To examine  $\chi_{ij} = \lim_{u \rightarrow 1} \chi_{ij}(u)$ , we first study the marginal distributions of the process (3).

**Proposition 1.1.** *Let  $\mathcal{D} = \{k : \gamma_k = 0, k = 1, \dots, K\}$  and  $\bar{\mathcal{D}}$  be the complement of  $\mathcal{D}$ . For process (3), the marginal distribution function of  $X_j = X(\mathbf{s}_j)$  can be written as*

$$F_j(x) = \exp \left\{ \sum_{k \in \bar{\mathcal{D}}} \gamma_k^\alpha - \sum_{k=1}^K \left( \gamma_k + \tau^{\frac{1}{\alpha_0}} \omega_{kj}^\alpha x^{-\frac{1}{\alpha_0}} \right)^\alpha \right\}. \quad (10)$$

As  $x \rightarrow \infty$ , the survival function  $\bar{F}_j(x) = 1 - F_j(x)$  satisfies

$$\bar{F}_j(x) = c'_j x^{-\frac{\alpha}{\alpha_0}} + c_j x^{-\frac{1}{\alpha_0}} + \left( d_j - \frac{c_j^2}{2} \right) x^{-\frac{2}{\alpha_0}} - \frac{c_j^2}{2} x^{-\frac{2\alpha}{\alpha_0}} - c'_j c_j x^{-\frac{\alpha+1}{\alpha_0}} + o\left(x^{-\frac{2}{\alpha_0}}\right), \quad (11)$$

where  $c_j = \alpha \tau^{1/\alpha_0} \sum_{k \in \bar{\mathcal{D}}} \gamma_k^{\alpha-1} \omega_{kj}^{1/\alpha}$ ,  $c'_j = \tau^{\alpha/\alpha_0} \sum_{k \in \mathcal{D}} \omega_{kj}$ , and  $d_j = \frac{\alpha(\alpha-1)}{2} \tau^{2/\alpha_0} \sum_{k \in \bar{\mathcal{D}}} \gamma_k^{\alpha-2} \omega_{kj}^{2/\alpha}$ .

The proof of this result can be found in Section B.2 of the Supplementary Material. It indicates that the process (3) has Pareto-like marginal tails at any location in the domain  $\mathcal{S}$ . If  $\mathcal{C}_j \cap \mathcal{D} \neq \emptyset$ , that is, if the  $j$ th location is impacted by an ‘‘un-tilted knot’’ (i.e., a knot with  $\gamma_k = 0$  in the  $\text{expPS}(\alpha, \gamma_k)$  distribution of the corresponding latent variable  $Z_k$ ), then  $\bar{F}_j(x) \sim c'_j x^{-\frac{\alpha}{\alpha_0}}$  as  $x \rightarrow \infty$  since  $\alpha \in (0, 1)$ . If, however, the location is not within the reach of an un-tilted knot, then instead  $\bar{F}_j(x) \sim c_j x^{-\frac{1}{\alpha_0}}$  as  $x \rightarrow \infty$ , which is less heavy-tailed.

The following result directly delineates how the quantile level changes as  $u \rightarrow 1$ .

**Corollary 1.1.1.** *As  $t \rightarrow \infty$ , the marginal quantile function  $q_j(t) = F_j^{-1}(1 - 1/t)$  can be approximated as follows under the assumptions of Proposition 1.1:*

$$q_j(t) = \begin{cases} c_j^{\alpha_0/\alpha} t^{\alpha_0/\alpha} \left\{ 1 + \frac{\alpha_0 c_j t^{1-1/\alpha}}{\alpha c_j^{1/\alpha}} - \frac{\alpha_0 t^{-1}}{2\alpha} + O(t^{-1/\alpha}) \right\}, & \text{if } \mathcal{C}_j \cap \mathcal{D} \neq \emptyset, \\ c_j^{\alpha_0} t^{\alpha_0} \left\{ 1 + \alpha_0 \left( \frac{d_j}{c_j^2} - \frac{1}{2} \right) t^{-1} + o(t^{-1}) \right\}, & \text{if } \mathcal{C}_j \cap \mathcal{D} = \emptyset. \end{cases}$$

The proof of this result can also be found in Section B.2 of the Supplementary Material. It will be used to derive the tail dependence structure for two arbitrary spatial locations.

### 1.3.2 Joint distribution

To derive the extremal dependence structure, we first calculate the joint distribution function of a  $n_s$ -variate random vector  $(X_1, \dots, X_{n_s})^T$  drawn from the process (3).

**Proposition 1.2.** *Under the definitions and notation as established in the previous sections, for locations  $\mathbf{s}_1, \dots, \mathbf{s}_{n_s} \in \mathcal{S}$ , the exact form of the joint distribution function of the*

random vector  $(X_1, \dots, X_{n_s})^T$  can be written as

$$F(x_1, \dots, x_{n_s}) = \exp \left\{ \sum_{k \in \mathcal{D}} \gamma_k^\alpha - \sum_{k=1}^K \left( \gamma_k + \tau^{\frac{1}{\alpha_0}} \sum_{j=1}^{n_s} \omega_{kj}^{\frac{1}{\alpha}} x_j^{-\frac{1}{\alpha_0}} \right)^\alpha \right\}. \quad (12)$$

The proof of Proposition 1.2 is given in Section B.3 of the Supplementary Material. Eq. (12) ensures that  $F^{1/r}(x_1, \dots, x_{n_s})$  is a valid distribution function on  $\mathbb{R}^{n_s}$  for any real  $r > 0$ , of the same form as (12) but with tilting indices  $\{\gamma_1/r^{1/\alpha}, \dots, \gamma_K/r^{1/\alpha}\}$  and scale parameter  $\tau/r^{\alpha_0/\alpha}$ . By definition, the process  $\{X_t(\mathbf{s}) : \mathbf{s} \in \mathcal{D}\}$  is thus max-infinitely divisible. It becomes max-stable only when it remains within the same location-scale family, i.e., when  $\gamma_1 = \dots = \gamma_K = 0$ .

### 1.3.3 Tail dependence properties

We now characterize the tail dependence structure of process (3) using both  $\chi_{ij}$  defined in Eq. (9) and the complementary measure  $\eta_{ij}$  defined by  $\Pr\{X_i > F_i^{-1}(u), X_j > F_j^{-1}(u)\} = \mathcal{L}\{(1-u)^{-1}\}(1-u)^{1/\eta_{ij}}$ , where  $\mathcal{L}$  is slowly varying at infinity, i.e.,  $\mathcal{L}(tx)/\mathcal{L}(t) \rightarrow 1$  as  $t \rightarrow \infty$  for all  $x > 0$ . The value of  $\eta_{ij} \in (0, 1]$  is used to differentiate between the different levels of dependence exhibited by an AI pair  $(X_i, X_j)^T$ . When  $\eta_{ij} = 1$  and  $\mathcal{L}(t) \not\rightarrow 0$  as  $t \rightarrow \infty$ ,  $(X_i, X_j)^T$  is AD ( $\chi_{ij} > 0$ ), and the remaining cases are all AI ( $\chi_{ij} = 0$ ; see Ledford and Tawn, 1996), with stronger tail dependence for larger values of  $\eta_{ij}$ .

**Theorem 1.3.** *Under the assumptions of Propositions 1.1 and 1.2, the process  $\{X(\mathbf{s})\}$  defined in (3) has a tail dependence structure characterized as follows:*

- (a) *If  $\mathcal{C}_i \cap \mathcal{D} = \emptyset$  and  $\mathcal{C}_j \cap \mathcal{D} = \emptyset$ , we have  $\chi_{ij} = 0$  and  $\eta_{ij} = 1/2$ .*
- (b) *If  $\mathcal{C}_i \cap \mathcal{D} = \emptyset$  and  $\mathcal{C}_j \cap \mathcal{D} \neq \emptyset$ , we have*

$$t \Pr\{X_i > q_i(t), X_j > q_j(t)\} = \begin{cases} c_{ij} t^{-\frac{1}{\alpha}} / (c_i c_j^{\frac{1}{\alpha}}) + o(t^{-\frac{1}{\alpha}}), & \text{if } \mathcal{C}_i \cap \mathcal{C}_j \neq \emptyset, \\ t^{-1}, & \text{if } \mathcal{C}_i \cap \mathcal{C}_j = \emptyset, \end{cases}$$

where  $c_{ij} = \alpha(\alpha - 1)\tau^{2/\alpha_0} \sum_{k \in \mathcal{C}_i \cap \mathcal{C}_j} \theta_k^{\alpha-2} \omega_{ki}^{1/\alpha} \omega_{kj}^{1/\alpha}$ . This leads to  $\chi_{ij} = 0$ ,  $\eta_{ij} = \frac{\alpha}{\alpha+1}$  when  $\mathcal{C}_i \cap \mathcal{C}_j \neq \emptyset$  and  $1/2$  when  $\mathcal{C}_i \cap \mathcal{C}_j = \emptyset$ .

- (c) *If  $\mathcal{C}_i \cap \mathcal{D} \neq \emptyset$  and  $\mathcal{C}_j \cap \mathcal{D} \neq \emptyset$ , we have*

$$t \Pr\{X_i > q_i(t), X_j > q_j(t)\} = 2 - d_{ij} - (c_i/c_i'^{1/\alpha} + c_j/c_j'^{1/\alpha})t^{1-\frac{1}{\alpha}} - O(t^{2-\frac{2}{\alpha}}),$$

where  $d_{ij} = \tau^{\alpha/\alpha_0} \sum_{k \in \mathcal{D}} \{(\omega_{ki}/c_i')^{1/\alpha} + (\omega_{kj}/c_j')^{1/\alpha}\}^\alpha \in (1, 2)$ . Thus,  $(X_i, X_j)^T$  is AD with  $\chi_{ij} = 2 - d_{ij}$  when  $\mathcal{C}_i \cap \mathcal{C}_j \neq \emptyset$ , and AI with  $\eta_{ij} = \alpha$  and  $\chi_{ij} = 0$  when  $\mathcal{C}_i \cap \mathcal{C}_j = \emptyset$ .

The proof of this result can be found in Section B.4 of the Supplementary Material. The local dependence strength is proportional to the tail-heaviness of the latent variable of the closest knot. There is local AD if  $\gamma_k = 0$  and there is local AI if  $\gamma_k > 0$ , as expected. Similar to Eq. (10), the sets  $\mathcal{C}_j \cap \mathcal{D}$ ,  $j = 1, \dots, n_s$ , are crucial to the behavior of the so-called

exponent function which occurs in the limiting distribution for normalized maxima (Huser and Wadsworth, 2019); see Remark 5 in Section B.4 for more discussion.

The compactness of the basis functions’ support yields long-range exact independence (thus, also AI) for two far-apart stations that are impacted by disjoint sets of basis functions; this is similar in spirit to the Cauchy convolution process of Krupskii and Huser (2022), though their model construction is different and less computationally tractable than ours.

## 2 Validation framework for extremes emulation

We propose a new validation framework that is tailored to assess skill in fitting both the full range of data and joint tail behavior in model outputs. This comprehensive framework can be used to evaluate the quality of emulations from any generative spatial extremes model and represents one of the contributions of this paper to the extremes literature.

### 2.1 Full range evaluation

To examine the quality of the emulation from the XVAE, we will predict at  $n_h$  locations  $\{\mathbf{h}_i : i = 1, \dots, n_h\}$  held out from the analyses. To perform these predictions, we calculate the basis function values at these locations, with which we can mix the encoded variables from Eq. (5) to get predicted values. For each time  $t$  and holdout location  $\mathbf{h}_i$ , denote the true observation of  $X_t(\mathbf{h}_i)$  by  $x_{it}$  and the emulated prediction by  $x_{it}^*$ . Then the mean squared prediction error (MSPE) for time  $t$  is

$$\text{MSPE}_t = \frac{1}{n_h} \sum_{i=1}^{n_h} (x_{it} - x_{it}^*)^2,$$

where  $t = 1, \dots, n_t$ . All MSPEs from different time replicates can be summarized in a boxplot; see Section 3 for example. Similarly, we can calculate the continuously ranked probability score (CRPS; Matheson and Winkler, 1976; Gneiting and Raftery, 2007) across time for each location, i.e.,

$$\text{CRPS}_i = \frac{1}{n_t} \sum_{t=1}^{n_t} \int_{-\infty}^{\infty} (F_i(z) - \mathbb{1}(x_{it}^* \leq z))^2 dz,$$

where  $F_i$  is the marginal distribution estimated using parameters at the holdout location  $\mathbf{h}_i$ ,  $i = 1, \dots, n_h$ , and again  $x_{it}^*$  is the emulated value. Smaller CRPS indicates that the distribution  $F_i$  is concentrated around  $x_{it}^*$ , and thus can be used to measure how well the distribution fits all emulated values. Section 3 also shows how we present the CRPS values from all holdout locations for each emulation. In addition, we will examine the quantile-quantile (QQ)-plots obtained by pooling the spatial data into the same plot to check if the spatial input and the emulation have similar ranges and quantiles.



## 2.2 Empirical tail dependence measures

To assess the tail dependence structure of the emulated fields, we will estimate  $\chi_{ij}(u)$  defined in Eq. (9) empirically in two ways. First, to examine the overall dependence strength, we treat  $\{X(\mathbf{s})\}$  as if it had a stationary and isotropic dependence structure so that  $\chi_{ij}(u) \equiv \chi_h(u)$ , with  $h = \|\mathbf{s}_i - \mathbf{s}_j\|$  being the distance between locations. Then for a fixed  $h$ , we find all pairs of locations with similar distances (within a small tolerance, say  $\epsilon = 0.001$ ), and compute the empirical conditional probabilities  $\widehat{\chi}_h(u)$  at a grid of  $u$  values. Confidence envelopes can be calculated by regarding the outcome (i.e., simultaneously exceed  $u$  or not) of each pair as a Bernoulli variable and computing pointwise binomial confidence intervals, assuming that all pairs of points are independent from each other. Examples in Section 3 demonstrate how this empirical measure can be used to compare the extremal dependence structures between the spatial data input and realizations from the emulator. While this metric does not completely characterize the non-stationarity in the process, it is still well-defined as a summary statistic and carries important information about the average decay of dependence with distance irrespective of the direction.

Second, to avoid the stationary assumption, we can choose a reference point denoted by  $\mathbf{s}_0$  and estimate the pairwise  $\chi_{0j}(u)$  empirically between  $\mathbf{s}_0$  and all observed locations  $\mathbf{s}_j$  in the spatial domain  $\mathcal{S}$ . These pairwise estimates can then be presented using a raster plot (if gridded) or a heat plot. Section 4 shows examples of the empirical  $\chi_{0j}(u)$ ,  $u = 0.85$ , estimated from the real and emulated datasets, where  $\mathbf{s}_0$  is the center of  $\mathcal{S}$ .

## 2.3 Areal radius of exceedance

We further propose a tail dependence coefficient that formally summarizes the overall dependence strength over the entire spatial domain. This metric characterizes the spatial extent of extreme events conditional on an arbitrary reference point in the domain (e.g., the center of  $\mathcal{S}$ ) exceeding a particular quantile  $u$ . Zhang et al. (2023) formulated the metric on an empirical basis and named it the averaged radius of exceedances (ARE).

Given a large number of independent replicates (say  $n_r$ ) from  $\{X(\mathbf{s})\}$  on a dense regular grid  $\mathcal{G} = \{\mathbf{g}_i \in \mathcal{S} : i = 1, \dots, n_g\}$  over the domain  $\mathcal{S}$  with side length  $\psi > 0$ , denote the replicates by  $\mathbf{X}_r = \{X_r(\mathbf{g}_i) : i = 1, \dots, n_g\}$ ,  $r = 1, \dots, n_r$ . The empirical marginal distribution functions at  $\mathbf{g}_i$  can then be obtained as  $\widehat{F}_i(x) = n_r^{-1} \sum_{r=1}^{n_r} \mathbb{1}(X_{ir} \leq x)$ , where  $X_{ir} = X_r(\mathbf{g}_i)$  and  $\mathbb{1}\{\cdot\}$  is the indicator function. We then transform  $(X_{i1}, \dots, X_{in_r})^T$  to the uniform scale via  $U_{ir} = \widehat{F}_i(X_{ir})$ ,  $r = 1, \dots, n_r$ . Let  $\mathbf{U}_r = \{U_{ir} : i = 1, \dots, n_g\}$  and  $U_{0r} = \widehat{F}_0\{X_r(\mathbf{s}_0)\}$ . The ARE metric at the threshold  $u$  is defined by

$$\widehat{\text{ARE}}_\psi(u) = \left\{ \frac{\psi^2 \sum_{r=1}^{n_r} \sum_{i=1}^{n_g} \mathbb{1}(U_{ir} > u, U_{0r} > u)}{\pi \sum_{r=1}^{n_r} \mathbb{1}(U_{0r} > u)} \right\}^{1/2}. \quad (13)$$

The summation  $\psi^2 \sum_{i=1}^{n_g} \mathbb{1}(U_{ir} > u, U_{0r} > u)$  in Eq. (13) calculates the area of all grid cells exceeding the extremeness level  $u$  at the same replicate  $r$  as the reference location  $\mathbf{s}_0$ ; dividing it by  $\pi$  and taking the square root thus yields the “radius” of a circular exceedance

region that has the same spatial extent. Additionally, Eq. (13) averages over all replicates with the reference location exceeding the extremeness level  $u$ . Therefore,  $\widehat{\text{ARE}}_\psi(u)$  has the same units as  $\psi$ , or the distance metric used on the domain  $\mathcal{S}$ , which makes it a more straightforward metric for domain scientists because it reflects the average length scale of the extreme events (e.g., warm pool size in SST data).

If there is an infinite number of independent replicates, the following result ensures that  $\widehat{\text{ARE}}_\psi(u)$  almost surely converges to

$$\text{ARE}_\psi(u) = \left( \psi^2 \sum_{i=1}^{n_g} \chi_{0i}(u) / \pi \right)^{1/2}, \quad (14)$$

where  $\chi_{0i}(u)$  is here the  $\chi$ -measure between locations  $\mathbf{s}_0$  and  $\mathbf{g}_i$  defined in Eq. (9).

**Theorem 2.1.** *For a fixed regular grid  $\mathcal{G}$  with side length  $\psi$ , a reference location  $\mathbf{s}_0$  and  $u \in (0, 1)$ , we have  $\widehat{\text{ARE}}_\psi(u) \rightarrow \text{ARE}_\psi(u)$  almost surely as  $n_r \rightarrow \infty$ .*

From this result, we see that  $\widehat{\text{ARE}}_\psi(u)$  and its limit, which do not require stationarity or isotropy, quantify the square root of spatial average of  $\chi_{0i}(u)$ . Due to the presence of the white noise term  $\epsilon(\mathbf{s})$  form, there is no version of the process  $\{X(\mathbf{s})\}$  that has measurable paths, which means that  $X(\mathbf{s}) \not\rightarrow X(\mathbf{s}_0)$  (in probability) as  $\mathbf{s} \rightarrow \mathbf{s}_0$ . However, from Theorem 1.3, we know that there is continuity in the dependence measure  $\chi_{0i}$  because  $\epsilon(\mathbf{s})$  has little impact on the dependence structure of the mixture  $Y(\mathbf{s})$ . That is,  $\chi_{\mathbf{s}_0, \mathbf{s}}$ , denoting the  $\chi$ -measure between location  $\mathbf{s}_0$  and  $\mathbf{s} \in \mathcal{S}$ , is a continuous function of  $\mathbf{s} \in \mathcal{S}$  when fixing the reference location  $\mathbf{s}_0$ ; we define this property to be *tail-continuous* for  $\mathbf{s}_0$ . The following result further confirms that under the tail-continuity,  $\widehat{\text{ARE}}_\psi(u)$  also converges to the square root of spatial integration of  $\chi_{\mathbf{s}_0, \mathbf{s}}$  as  $u \rightarrow 1$  and as  $\mathcal{G}$  becomes infinitely dense.

**Theorem 2.2.** *Let the domain  $\mathcal{S}$  be bounded (i.e., its area  $|\mathcal{S}| < \infty$ ) and process  $\{X(\mathbf{s}) : \mathbf{s} \in \mathcal{S}\}$  be tail-continuous for  $\mathbf{s}_0$  (i.e.,  $\chi_{\mathbf{s}_0, \mathbf{s}}$  is a continuous function of  $\mathbf{s}$  in  $\mathcal{S}$ ). Then,*

$$\lim_{\psi \rightarrow 0, u \rightarrow 1} \psi \left( \sum_{i=1}^{n_g} \chi_{0i}(u) \right)^{1/2} = \left\{ \int_{\mathcal{S}} \chi_{\mathbf{s}_0, \mathbf{s}} d\mathbf{s} \right\}^{1/2}. \quad (15)$$

**Remark 1.** *Tail-continuity is met by many spatial extremes models, like max-stable, inverted-max-stable, and others (e.g., Opitz, 2016; Huser and Wadsworth, 2019; Wadsworth and Tawn, 2022). Our model (3) also adheres to tail-continuity, as indicated by Theorem 1.3.*

**Remark 2.** *Together, Theorems 2.1 and 2.2 ensure that  $\widehat{\text{ARE}}_\psi(u) \approx \left\{ \int_{\mathcal{S}} \chi_{\mathbf{s}_0, \mathbf{s}} d\mathbf{s} \right\}^{1/2} / \pi^{1/2}$  if there are a large number of replicates from the process  $\{X(\mathbf{s})\}$  on a very dense grid  $\mathcal{G}$ .*

Similarly, we can estimate  $\text{ARE}_\psi(u)$  for the emulator by running the decoder repeatedly to obtain emulated replicates of  $\{X(\mathbf{s})\}$  on the same grid. By comparing the  $\text{ARE}_\psi(u)$  estimates at a series of  $u$  levels, we can evaluate whether the spatially-aggregated exceedance is consistent between the spatial data inputs and their XVAE emulation counterparts.

## 2.4 Uncertainty quantification

The decoder (8) functions as a neural estimator for  $(\alpha_t, \boldsymbol{\gamma}_t^T)^T$ . Examining its inferential power is crucial, as accurate emulation heavily relies on precise characterization of spatial inputs. Drawing a substantial number of samples from the variational distribution  $q_{\phi_e}(\cdot | \mathbf{x}_t)$  (which is close to  $p_{\phi_d}(\cdot | \mathbf{x}_t)$ ; recall Section 1.1) allows us to obtain Monte Carlo estimates of the dependence parameters  $(\alpha_t, \boldsymbol{\gamma}_t^T)^T$  using the decoder (8). Aggregating these estimates provides approximate samples of the posterior  $(\alpha_t, \boldsymbol{\gamma}_t^T)^T | \{\mathbf{x}_t : t = 1, \dots, n_t\}$ , which enables the calculation of point estimates (posterior mean or maximum *a posteriori*) and the construction of approximate confidence regions for uncertainty quantification.

## 3 Simulation study

In this section, we simulate data from five different parametric models that have varying levels of extremal dependence across space. By examining the diagnostics introduced in Section 2, we validate the efficacy of our XVAE to analyze and emulate data from both model (3) and misspecified models.

### 3.1 General setting

To assess the performance of our XVAE, we conduct a simulation study in which data are generated at  $n_s = 2,000$  random locations uniformly sampled over the square  $[0, 10] \times [0, 10]$ . We simulate  $n_t = 100$  replicates of the process from each of the following different models:

- I. Gaussian process with zero mean, unit variance, and Matérn correlation  $C(\mathbf{s}_j, \mathbf{s}_j; \phi, \nu)$ , in which  $\phi = 3$  and  $\nu = 5/2$  are range and smoothness parameters;
- II. Max-id process (3) with  $K = 25$  basis functions and  $|\mathcal{D}| = 0$  un-tilted knots;
- III. Max-id process (3) with  $K = 25$  basis functions and  $0 < |\mathcal{D}| < K$  un-tilted knots;
- IV. Max-id process (3) with  $K = 25$  basis functions and  $|\mathcal{D}| = K$  un-tilted knots;
- V. Max-stable Reich and Shaby (2012) model with  $K = 25$  basis functions.

When simulating from Models II–IV, we use time-invariant dependence parameters  $\alpha_t \equiv \alpha$  and  $\boldsymbol{\gamma}_t \equiv \boldsymbol{\gamma}$ ; see Figure 1 for the knot locations and  $\boldsymbol{\gamma}$  values. Recall that  $K$  is the number of basis functions and  $\mathcal{D} = \{k : \gamma_k = 0\}$ . Models I–V gradually exhibit increasingly stronger extremal dependence, and they can help us test whether the XVAE can capture spatially-varying dependence structures that exhibit local AD and/or local AI. Since the proposed process (3) allows  $\gamma_k$  to change at different knots ( $k = 1, \dots, K$ ), a well-trained XVAE should be able to differentiate between local AD ( $\gamma_k = 0$ ) and local AI ( $\gamma_k > 0$ ).

Model I is a stationary and isotropic Gaussian process with a Matérn covariance function. It is known that the joint distribution of the Gaussian process at any two locations  $\mathbf{s}_i$  and  $\mathbf{s}_j$  is light-tailed and leads to AI unless the correlation equals one. For Models II, III and IV, we simulate data from the max-id model (3) with  $K = 25$  evenly-spread knots

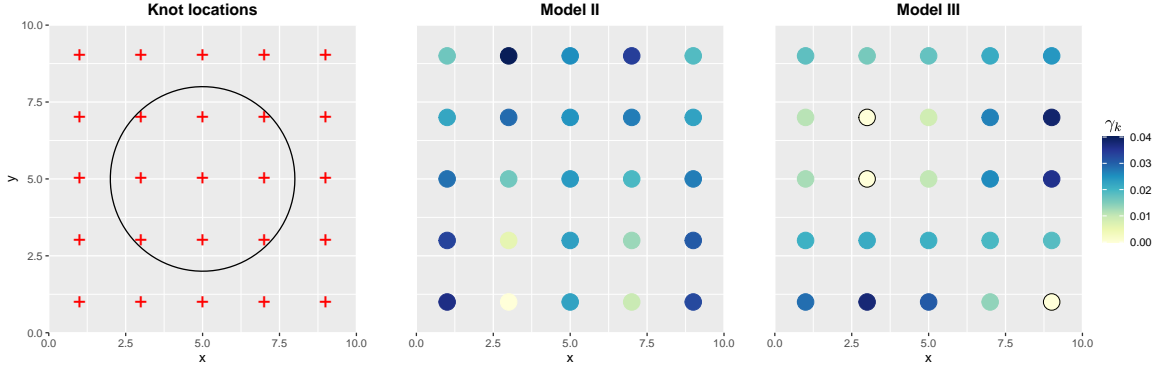


Figure 1: The left panel presents knot locations used for simulating data under Models II–IV, and we only show the support of the one Wendland basis function centered at knot in the middle of the domain. Model V uses the same set of knots but the basis functions are not compactly supported. The middle and right panels display the  $\gamma_k$  values,  $k = 1, \dots, K$ , used in the exponentially-tilted PS variables at each knot for Models II and III respectively. The circled knots signify  $\gamma_k = 0$ , which induces local AD.

across the grid, denoted by  $\{\tilde{\mathbf{s}}_1, \dots, \tilde{\mathbf{s}}_K\}$ . Setting the range parameter to  $r = 3$ , we use compactly supported Wendland basis functions  $\omega_k(\mathbf{s}, r) \propto \{1 - d(\mathbf{s}, \tilde{\mathbf{s}}_k)/r\}_+^2$  centered at each knot (Wendland, 1995),  $k = 1, \dots, K$ ; see Figure 1. The basis function values are standardized so that for each  $\mathbf{s}$ ,  $\sum_{k=1}^K \omega_k(\mathbf{s}, r) = 1$ . The main difference between Models II, III and IV lies in the  $\gamma_k$  values: Model II has no zero  $\gamma_k$ 's (i.e.,  $|\mathcal{D}| = 0$ ), whereas Model III has a mix of positive and zero  $\gamma_k$ 's, and Model IV has only zero  $\gamma_k$ 's (i.e.,  $|\mathcal{D}| = K$ ). By Theorem 1.3, we know Model II gives only local AI and Model IV gives only local AD. In contrast, Model III gives both local AD and local AI. By contrast, Model V adopts the same set of knots but it uses Gaussian radial basis functions which are not compactly supported. Therefore, Model V is the Reich and Shaby (2012) max-stable model, and has stronger extremal dependence than Models I–IV.

When simulating from Models II–V, we choose the parameter  $\alpha = 1/2$  and then sample the latent variables  $\mathbf{Z}_t$  from the exponentially-tilted PS distribution for each time replicate. Additionally, for Models II–IV, the white noise process  $\epsilon_t(\mathbf{s})$  follows the same independent Fréchet(0,  $\tau$ ,  $1/\alpha_0$ ) distribution with  $\tau = 1$  and  $\alpha_0 = 1/4$ .

For each space-time simulated dataset, we randomly set aside 100 locations as a validation set. Subsequently, we analyze the dependency structure of the remaining 1,900 locations using both the proposed XVAE (initialized with data-driven knots unless specified otherwise) and a Gaussian process regression with heteroskedastic noise implemented in the R package `hetGP` (Binois and Gramacy, 2021). We then perform predictions at the 100 holdout locations as outlined in Section 2.1. In the following result sections, we show that both emulators will have good performances when emulating datasets from Models I and II, but only XVAE appropriately captures AD in Models III–V.

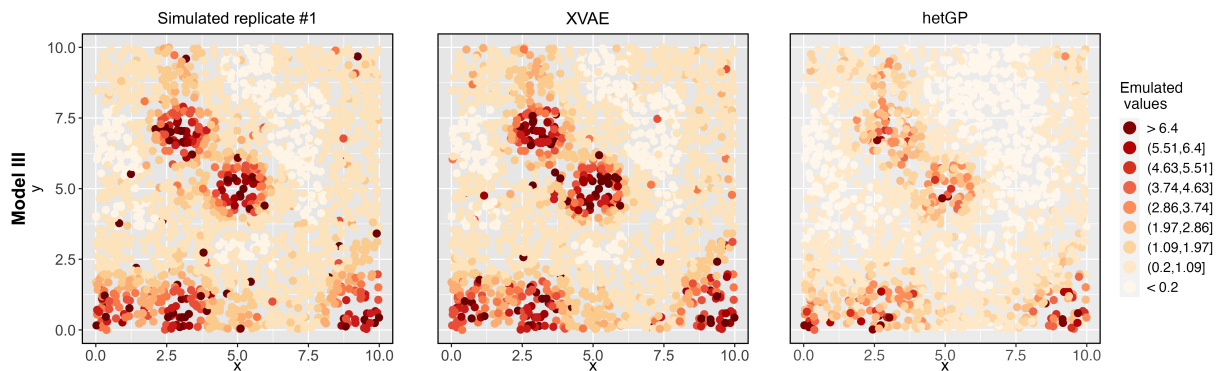


Figure 2: Data replicate (left) and its corresponding emulated fields (XVAE, middle; **hetGP**, right) from Model III. See Figure E.1 of the Supplementary Material for comparisons for the other models. In all cases, we use data-driven knots for emulation using XVAE.

### 3.2 Emulation results

Figure 2 and Figure E.1 of the Supplementary Material compare emulated replicates from XVAE and **hetGP** with data replicates from Models I–V, while Figure E.2 displays QQ-plots that align well with the 1-1 line in all cases for XVAE but not for **hetGP**. Since the Gaussian process has much weaker extremal dependence, the resulting  $\gamma_t$  estimated in (8) after convergence is consistently far greater than 0.1, indicating light tails in the exponentially-tilted PS variables and thus, local AI at all knots. Similarly, for Model II, there is AI everywhere in the domain. However, the  $\gamma_t$  values we used for Model II are much smaller than 0.1 (see Figure 1) and thus the fitted exponentially-tilted PS variables are heavier-tailed than the ones from Model I. Therefore, **hetGP** has difficulty in capturing the extremal dependence and the QQ-plot shows that large values in the tail tend to be underestimated, even though Model II still exhibits AI only.

For Models III–V, there is local AD, and we see that **hetGP** completely fails at emulating the co-occurrence of extreme values. Because **hetGP** focuses on the bulk of the distribution, it ignores spatial extremal dependence. This validates the need to incorporate a flexible spatial model in the emulator to capture tail dependence accurately.

Figure 3 compares the performance of spatial predictions at the 100 holdout locations. For Model I, **hetGP** has lower CRPS and MSPE scores, indicating higher predictive power, as expected since the true process is Gaussian. However, the XVAE model still performs quite well in this case. For Models II–V, XVAE uniformly outperforms **hetGP**. Also, the CRPS and MSPE for **hetGP** are significantly higher for time replicates with extreme events.

The left three panels of Figure 4 and Figure E.3 of the Supplementary Material compare nonparametric estimates of the upper tail dependence  $\chi_h(u)$  from the data replicates and emulations at three different distances  $h \in \{0.5, 2, 5\}$  under the working assumption of stationarity. In general, we see that the dependence strength decays as  $h$  and  $u$  increase, with varying levels of positive limits as  $u \rightarrow 1$  for Models III–V. The results in Figure 4

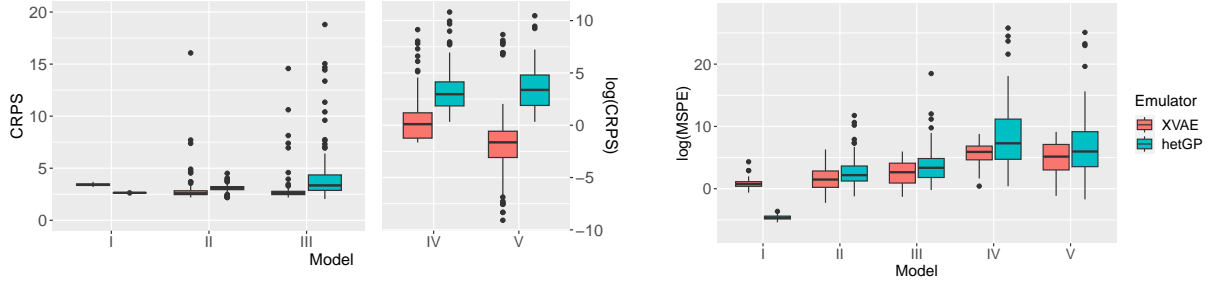


Figure 3: The CRPS (left) and MSPE (right) values from two emulation approaches on the datasets simulated from Models I–V. For both metrics, lower values indicate better emulation results. Also, for Models IV and V, we plot the CRPS values on the log scale since the AD in the data generating process causes the margins to be very heavy-tailed.

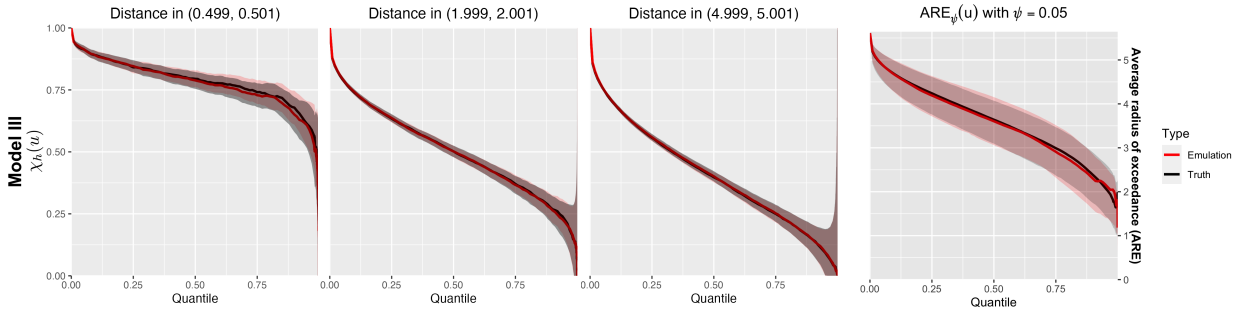


Figure 4: From left to right, we show the empirically-estimated  $\chi_h(u)$  at  $h = 0.5, 2, 5$ , and  $ARE_\psi(u)$  with  $\psi = 0.05$  for Model III based on data replicates (black) and XVAE emulated data (red). The  $\chi_h(u)$  and  $ARE_\psi(u)$  estimates for the other models are shown in Figures E.3 and E.4 of the Supplementary Material, respectively.

demonstrate that our XVAE manages to accurately emulate the dependence behavior at both low and high quantiles and the empirical confidence envelopes of  $\chi_h(u)$  are essentially indistinguishable between the simulated and emulated data.

Choosing  $(5, 5)$  as the reference point, the rightmost panel of Figure 4 displays estimates of  $ARE_\psi(u)$ ,  $\psi = 0.05$ , for both data replicates and emulated data under Models I–V. We see that the empirical AREs from the XVAE are consistent with the ones estimated from the data except for Model V, where  $ARE(u)$  is slightly underestimated at low thresholds  $u$  but overestimated at high  $u$ . As expected, the limit of  $ARE(u)$  as  $u \rightarrow 1$  is non-negative for Models III–V when there is local AD, and the limit increases from Model III to V.

To showcase the inferential capabilities of our approach, we initialize the XVAE with true knots and rerun it on datasets simulated from Models II and III. Figure 5 displays  $\gamma_t$  estimates obtained by running the decoder (i.e., Eq. (8)) 1000 times at  $t = 1$ . The results highlight the XVAE’s ability to produce accurate estimates of  $\gamma_t = \{\gamma_{kt} : k = 1, \dots, K\}$ , and correctly identify the extremal dependence class, with satisfactory agreement between



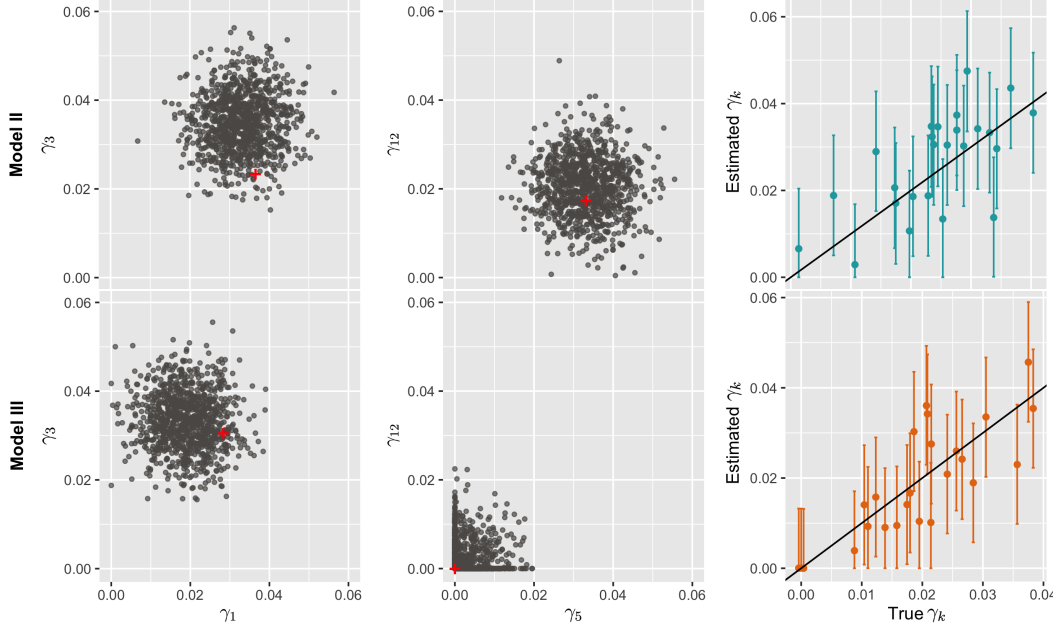


Figure 5: Initializing the XVAE using the true knots from Models II (top) and III (bottom), we show the estimates of  $(\gamma_{1t}, \gamma_{3t})^T$  (left) and  $(\gamma_{5t}, \gamma_{12t})^T$  (middle) from 1,000 samples generated with the trained decoder ( $t = 1$ ). On the right, we also show the medians, 2.5% and 97.5% quantiles of the  $n_t$  estimates of  $\{\gamma_{kt} : k = 1, \dots, K\}$  for  $t = 1$ , from the decoder (8), in which the 1-1 line is displayed in black for reference.

true and estimated values, accounting for uncertainty. Additionally, we perform a coverage analysis by simulating 99 more datasets with  $n_s = 2000$  and  $n_t = 100$  from Models II and III, running the XVAE on each to generate empirical credible intervals for  $\gamma_t$ . Figure E.5 of the Supplementary Material shows the coverage probabilities of  $\{\gamma_{kt} : k = 1, \dots, K\}$  for  $t = 1$ . Most estimated probabilities align closely with the nominal 95% level, except when  $\gamma_{kt} = 0$ , where coverage is poorer due to the true value residing on the parameter space boundary. Nevertheless, these promising results endorse the XVAE as a fast and robust inference tool for estimating parameters in the max-id process (3) and for Bayesian UQ.

## 4 Application to Red Sea surface temperature data

The Red Sea, a biodiversity hot spot, is susceptible to coral bleaching due to climate change and rising SST anomalies (Furby et al., 2013). Corals are unlikely to survive once the temperature exceeds a bleaching threshold annually, which in turn causes disruption in fish migration and slow decline in fish abundance. Here, we analyze and emulate a Red Sea surface temperature dataset, which consists of satellite-derived daily SST estimates at 16,703 locations on a  $1/20^\circ$  grid from 1985/01/01 to 2015/12/31 (11,315 days in total); see Donlon et al. (2012). This yields about 189 million correlated spatio-temporal data points. Through our analysis, we demonstrate the importance of generating realistic realizations



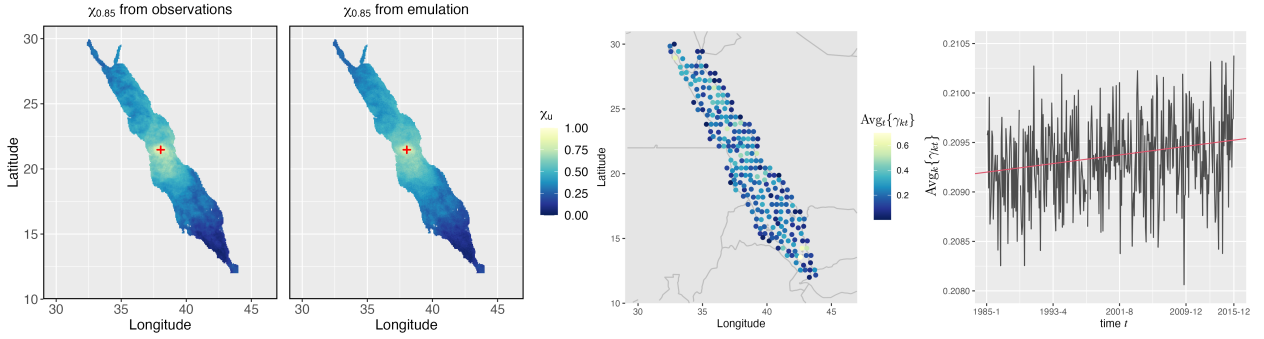


Figure 6: In the left two panels, we show empirically-estimated pairwise tail dependence measure  $\chi_{0j}(u)$ ,  $u = 0.85$ , between  $\mathbf{s}_0 = (38.104, 21.427)$ , marked using a red cross, and all  $\mathbf{s}_j \in \mathcal{S}$ , from observations and emulated data. In the right two panels, we show the estimated tilting parameters at  $K = 243$  data-driven knots averaged over time (i.e.,  $n_t^{-1} \sum_{k=1}^{n_t} \gamma_{kt}$ ,  $k = 1, \dots, K$ ), and the estimated tilting parameters averaged over space (i.e.,  $K^{-1} \sum_{k=1}^K \gamma_{kt}$ ,  $t = 1, \dots, n_t$ ) with the best linear regression fit (red line).

and quantifying uncertainty associated with threshold exceedances—they could for example be used to accurately assess marine heatwave (MHW) risks and identify regions susceptible to coral bleaching by refining the threshold for MHW detection with improved UQ.

This dataset has previously been analyzed (sometimes partially) by [Hazra and Huser \(2021\)](#), [Simpson and Wadsworth \(2021\)](#), [Simpson et al. \(2023\)](#), [Oesting and Huser \(2022\)](#), and [Sainsbury-Dale et al. \(2024\)](#). The latter three studies focused on a small portion of the Red Sea using the summer months only to eliminate the effects of seasonality. For example, [Sainsbury-Dale et al. \(2024\)](#) retained a dataset with only 678 spatial locations and 141 replicates. By contrast, [Hazra and Huser \(2021\)](#) extensively studied weekly data over the entire spatial domain using a Dirichlet process mixture of low-rank spatial Student’s  $t$  processes to account for spatial dependence. However, their model is AD across the entire domain (i.e., for any pair of locations), limiting its flexibility in capturing extreme behavior.

Since the daily SST at each location exhibits a clear trend and seasonality across seasons and years and the temporal dependence strength varies at different locations, we first de-trend and remove the seasonality before applying our model (see Section F.1 of the Supplementary Material for details). Despite the successful performance of our XVAE in Section 3 when the data input is not generated from the process (3), we opt to extract monthly maxima from the renormalized data to better comply with the assumed max-infinite divisibility and to enhance the modeling accuracy of marginal distributions for station records. In Section F.2, we perform various goodness-of-fit tests using the generalized extreme value (GEV) distribution and the general non-central  $t$  distribution, and find that the former performs better than the latter and it fits the monthly maxima very well at almost all grid points (99.99% of the 16,703 locations). Therefore, we fit a GEV distribution at each location and transform the sitewise records to the Pareto scale on which we then apply the XVAE; see Section F.3 for specifics.

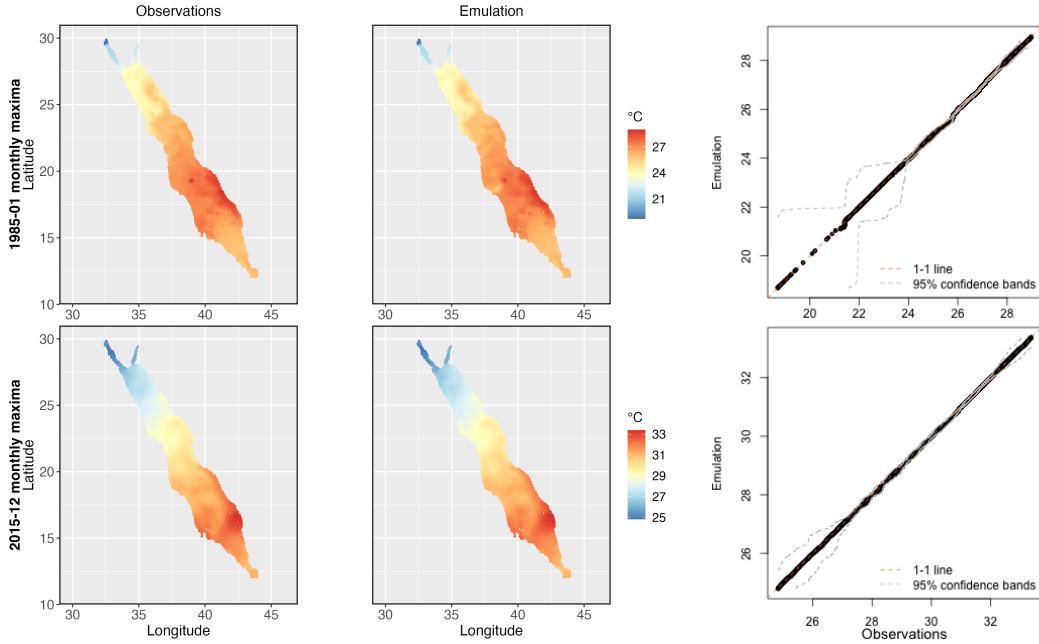


Figure 7: Observed (left) and emulated (middle) Red Sea SST monthly maxima, for the 1985/01 (top) and 2015/12 (bottom) months. From the emulation maps and QQ plots (right), we see that the emulated fields from the XVAE match the observations very well.

The third panel of Figure 6 displays the locations of the data-driven knots chosen by our algorithm ( $K = 243$ ), and the initial radius shared by the Wendland basis functions is  $1.2^\circ$ . Figure 7 shows emulated replicates of the original monthly maxima field for the first and last months (1985/01 and 2015/12, respectively). Here, we convert the emulated values back to the original data scale using the estimated GEV parameters fitted from the previous step. Figure 7 demonstrates that the XVAE is able to capture the detailed features of the temperature fields and to accurately characterize spatial dependence, while the QQ-plot shows an almost perfect alignment with the 1-1 line.

Similar to Figure 4, we then estimate  $\chi_h(u)$  empirically for the original monthly maxima and emulated fields, under the working assumption of stationarity and isotropy. Figure F.2 of the Supplementary Material attests once more that our XVAE characterizes the extremal dependence structure accurately from low to high quantiles. As introduced in Section 2, we

also examine the pairwise  $\chi$  measure without assuming spatial stationarity. Specifically, we choose the center of the Red Sea (38.104°E, 21.427°N) as a reference point denoted by  $\mathbf{s}_0$ . For all observed locations  $\mathbf{s}_j \in \mathcal{S}$  in the Red Sea, we estimate the pairwise  $\chi_{0j}(u)$  empirically only using the values from  $\mathbf{s}_j$  and  $\mathbf{s}_0$ . The left two panels of Figure 6 include raster plots of the pairwise measure evaluated at the level  $u = 0.85$ , in which the  $\chi_{0j}(u)$  values estimated from the observed and emulated data are very similar to each other.

One other major advantage of our XVAE framework is that it allows the dependence parameters  $\{\gamma_k : k = 1, \dots, K\}$  and  $\alpha$  to change over time, which makes the extremal dependence structure non-stationary. The right two panels of Figure 6 show the estimated tilting parameters  $\{\gamma_{kt} : k = 1, \dots, K, t = 1, \dots, n_t\}$  averaged over time/space. We see that the  $\gamma_{kt}$  values are generally lower near the coast compared to the interior of the Red Sea, indicating that SST tends to be more heavy-tailed on the coast. Also,  $\gamma_{kt}$  tends to increase over time, indicating that extreme events are becoming more localized. This is consistent with the findings in [Genevier et al. \(2019\)](#).

To examine what the SST fields look like without the noise, the left panels of Figure 8 display realizations of the latent field  $\{Y_t(\mathbf{s})\}$  using the fitted XVAE at two time points, 1985/9 and 2015/9. To focus on the extreme values, we transform  $Y_t(\mathbf{s})$  to the original SST scale using the estimated GEV parameters and censor the simulations with a fixed thermal threshold of 31°C, resulting in threshold exceedances primarily in the southern region. This is expected: the southern Red Sea experiences higher SSTs compared to the northern area. However, coral reefs in different parts of the Red Sea have developed varying levels of thermal tolerance ([Hazra and Huser, 2021](#)). To explore regional variation in marine heatwave (MHW) and coral bleaching risk, we divide the Red Sea into four regions based on [Raitzos et al. \(2013\)](#) and [Genevier et al. \(2019\)](#): North (25.5–30°N), North central (22–25.5°N), South central (17.5–22°N) and South (12.5–17.5°N).

A useful quantity is the areal exceedance probability, which represents the spatial extent of a region being simultaneously at extreme risk of MHW. To accurately estimate these joint probabilities (and uncertainties thereof) based on the trained XVAE, we generate 30,000 independent SST emulations for each time point and calculate the total area exceeding the designated threshold of 31°C. One could easily define a different, potentially spatially-varying, thermal threshold (e.g., with fixed marginal probability of exceedances). The middle panels of Figure 8 report the results, namely the density of the total area at risk of MHW within each region. The curves for the south central and south regions concentrate around larger areas, while the north central and north regions show little or no exceeded areas, confirming that surface temperatures decrease with increasing latitude. Additionally, the middle panels illustrate that under rising SST conditions, simultaneous exceedances of 31°C across larger areas may become more likely over time for all subregions except the north, where 31°C still surpasses the highest possible temperature in September 2015.

In order to provide a more detailed description of the spatial extent of areas of joint threshold exceedances at different extreme levels, we then estimate the SST threshold required for an array of fixed spatial extents of exceedances. For each fixed spatial extent, we calculate the minimal threshold needed to reach that area of joint exceedances from each emulated replicate, and we then group all 30,000 estimated thresholds together to

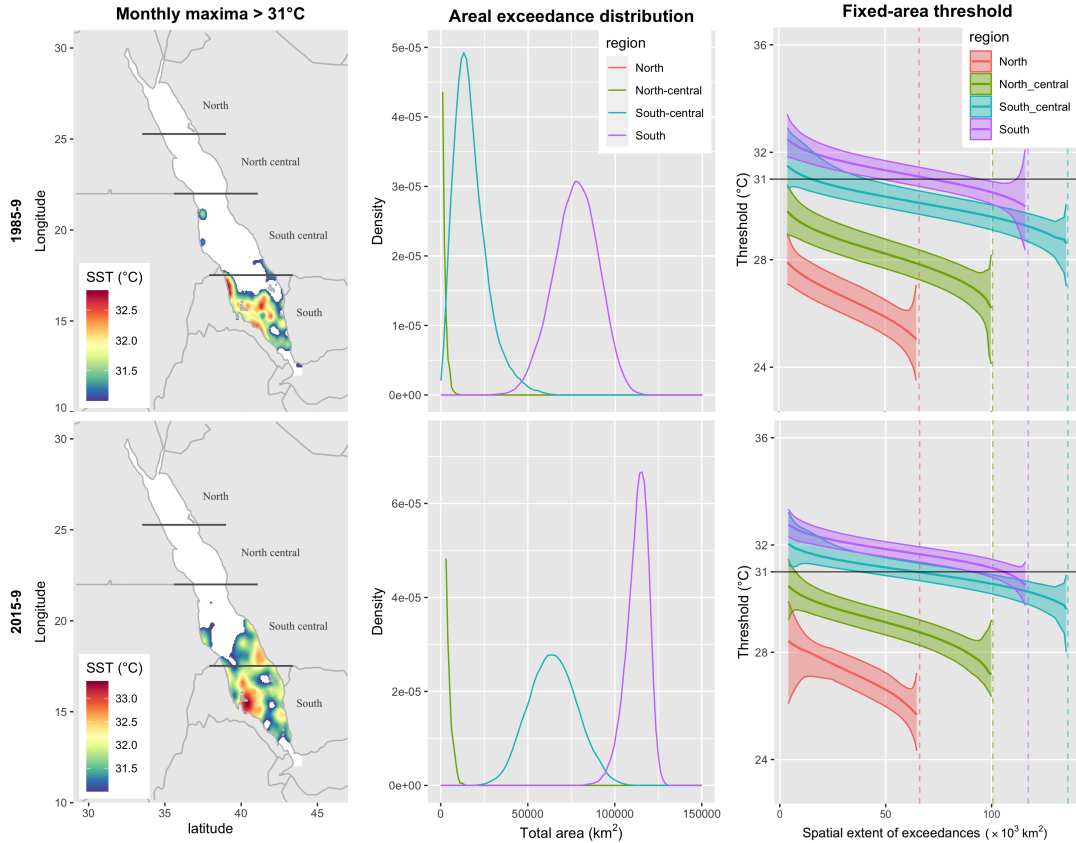


Figure 8: The left panels show realizations of Red Sea SST monthly maxima emulated with fitted parameters from the XVAE for 1985/9 (top) and 2015/9 (bottom) months. The emulations are censored with a threshold of 31°C. From 30,000 such emulations, we estimate the distribution of total area exceeding 31°C within each region. On the right, we estimate the threshold it takes to have a fixed area of exceedance. The 95% confidence intervals are also shown. The vertical dashed lines are total areas of each subregion, and the horizontal slices at 31°C yield results that align with the middle panels.

derive 95% empirical confidence intervals. We repeat this process for all spatial extents of exceedances in between 100 km<sup>2</sup> and  $1.4 \times 10^5$  km<sup>2</sup>. Note that this can be computed quite

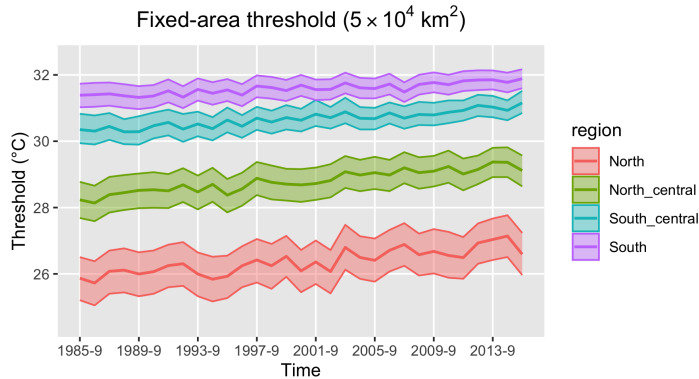


Figure 9: Similar to Figure 8, we emulate 30,000 independent SST fields for each September from 1985 to 2015. For a fixed areal exceedance of  $5 \times 10^4 \text{ km}^2$ , we estimate its associated required threshold along with the 95% Monte Carlo confidence intervals.

fast thanks to the amortized nature of our XVAE. The right panels of Figure 8 illustrate a consistent rise in SST thresholds across all extreme levels from 1985 to 2015. This trend is further confirmed in Figure 9, reporting the same results for a specific area of  $5 \times 10^4 \text{ km}^2$ . Slicing the confidence bands at the  $31^\circ\text{C}$  threshold aligns with the middle panel results, demonstrating that we can provide sensible uncertainty quantification when evaluating the spatial extent of exceedances at any extreme level. This also shows that the joint tail of SSTs exhibits a weakening dependence structure within each subregion, with the spatial extent of exceedances decreasing as the threshold increases and extreme events becoming more localized as they get more extreme. Furthermore, as the spatial extent approaches zero, the threshold estimates represent the highest possible SST for a specific month in a subregion, a valuable metric for studying phytoplankton bloom.

To directly assess the impact of climate change, we determine the threshold necessary for one specific spatial extent of exceedances (i.e.,  $5 \times 10^4 \text{ km}^2$ ) across all September months from 1985 to 2015. Here, we also emulate 30,000 SST fields for each September month in this period. Figure 9 reveals that the fixed-area SST threshold increased steadily by  $0.7^\circ$  in all four subregions on average over the studied time period, corroborating the warming trend in the Red Sea and the localized nature of extremes shown in Figures 6 and 8.

## 5 Concluding remarks

In this paper, we propose XVAE, a new variational autoencoder, which integrates a novel max-id model for spatial extremes that exhibits flexible extremal dependence properties. It greatly advances the ability to model extremes in high-dimensional spatial problems and expands the frontier on computation and modeling of complex extremal processes. The encoder and decoder construction and the trained distributions of the latent variables allow for parameter estimation and uncertainty quantification within a variational Bayesian framework. We also provide general guidance on evaluating emulator performance when

applied to spatial data with dependent extremes.

We note that our emulator extends beyond emulating large datasets for UQ. As highlighted in the introduction, the XVAE can serve as a surrogate model for mechanic-based computer models. It can also be applied to areas other than climate-related problems. For example, turbulent buoyant plume can be simulated from a system of compressible Euler conservative equations in flux formulation, but the computational cost is prohibitively expensive with increasing Reynolds number (Bhimireddy and Bhaganagar, 2021). Our XVAE can provide a promising avenue for efficiently emulating the chaotic and irregular turbulence observations in high resolutions.

One possible model improvement is that the latent exponentially-tilted PS variables are independent over space and time, which is unrealistic for physical processes that exhibit diffusive dynamics at short-time scales. In future work, we are planning to include a time component with data-driven dynamic learning based on a stochastic dynamic spatio-temporal model. Hence, the latent variables in the encoded space will evolve smoothly over time while retaining heavy tails and thus simultaneously ensuring local extremal dependence. Also, it is possible to improve the XVAE by allowing spatially-varying radii  $r_k$ ,  $k = 1, \dots, K$ , and estimate them by optimizing the ELBO together with other parameters.

Another promising direction for future work is to implement a *conditional* VAE (CVAE; Sohn et al., 2015) with a similar underlying max-id model; in such a model, we can allow the parameters of both the encoder and decoder to change conditioning on different climate scenarios (e.g., radiative forcings, seasons, soil conditions, etc.). This will allow us to simulate new data under different conditions. We will need to ensure that the CVAE emulates  $\mathbf{x}_t$  differently according to different input states (e.g., tuning parameters and/or forcing variables). In doing so, we will allow changes to the parameters for both the encoder and decoder conditioning on different scenarios (e.g., different climate states).

## References

- Arpat, G. B. and Caers, J. (2007), ‘Conditional simulation with patterns’, *Mathematical Geology* **39**, 177–203.
- Bhimireddy, S. R. and Bhaganagar, K. (2021), ‘Implementing a new formulation in WRF-LES for Buoyant Plume Simulations: bPlume-WRF-LES model’, *Monthly Weather Review* **149**(7), 2299–2319.
- Binois, M. and Gramacy, R. B. (2021), ‘hetGP: Heteroskedastic Gaussian process modeling and sequential design in R’, *Journal of Statistical Software* **98**(13), 1–44.
- Bopp, G. P., Shaby, B. A. and Huser, R. (2021), ‘A hierarchical max-infinitely divisible spatial model for extreme precipitation’, *Journal of the American Statistical Association* **116**(533), 93–106.
- Cartwright, L., Zammit-Mangion, A. and Deutscher, N. M. (2023), ‘Emulation of greenhouse-gas sensitivities using variational autoencoders’, *Environmetrics* **34**(2).
- Cotsakis, R., Di Bernardino, E. and Opitz, T. (2022), ‘On the perimeter estimation of

- pixelated excursion sets of 2D anisotropic random fields’, *Hal Science preprint: hal-03582844v2*.
- Davison, A. C. and Huser, R. (2015), ‘Statistics of extremes’, *Annual Review of Statistics and its Application* **2**, 203–235.
- Davison, A. C., Huser, R. and Thibaud, E. (2019), Spatial extremes, in ‘Handbook of Environmental and Ecological Statistics’, editors A. E. Gelfand, M. Fuentes, J. A. Hoeting and R. L. Smith, CRC Press, pp. 711–744.
- Davison, A. C., Padoan, S. A. and Ribatet, M. (2012), ‘Statistical Modeling of Spatial Extremes’, *Statistical Science* **27**(2), 161–186.
- de Fondeville, R. and Davison, A. C. (2018), ‘High-dimensional peaks-over-threshold inference’, *Biometrika* **105**(3), 575–592.
- Donlon, C. J., Martin, M., Stark, J., Roberts-Jones, J., Fiedler, E. and Wimmer, W. (2012), ‘The operational sea surface temperature and sea ice analysis (OSTIA) system’, *Remote Sensing of Environment* **116**, 140–158.
- Falbel, D. and Luraschi, J. (2023), *torch: Tensors and Neural Networks with ‘GPU’ Acceleration*. **URL:** <https://github.com/mlverse/torch>.
- Ferreira, A. and de Haan, L. (2014), ‘The generalized Pareto process; with a view towards application and simulation’, *Bernoulli* **20**(4), 1717–1737.
- Furby, K. A., Bouwmeester, J. and Berumen, M. L. (2013), ‘Susceptibility of central Red Sea corals during a major bleaching event’, *Coral Reefs* **32**, 505–513.
- Genevier, L. G., Jamil, T., Raitsos, D. E., Krokos, G. and Hoteit, I. (2019), ‘Marine heatwaves reveal coral reef zones susceptible to bleaching in the Red Sea’, *Global Change Biology* **25**(7), 2338–2351.
- Gneiting, T. and Raftery, A. E. (2007), ‘Strictly proper scoring rules, prediction, and estimation’, *Journal of the American statistical Association* **102**(477), 359–378.
- Goodfellow, I., Pouget-Abadie, J., Mirza, M., Xu, B., Warde-Farley, D., Ozair, S., Courville, A. and Bengio, Y. (2014), ‘Generative adversarial nets’, *Advances in Neural Information Processing Systems* **27**.
- Gramacy, R. B. (2020), *Surrogates: Gaussian Process Modeling, Design, and Optimization for the Applied Sciences*, Chapman and Hall/CRC.
- Gu, M., Wang, X. and Berger, J. O. (2018), ‘Robust Gaussian stochastic process emulation’, *The Annals of Statistics* **46**(6A), 3038–3066.
- Hartigan, J. A. and Wong, M. A. (1979), ‘Algorithm AS 136: A k-means clustering algorithm’, *Journal of the Royal Statistical Society: Series C* **28**(1), 100–108.
- Hazra, A. and Huser, R. (2021), ‘Estimating high-resolution Red Sea surface temperature hotspots, using a low-rank semiparametric spatial model’, *The Annals of Applied Statistics* **15**(2), 572–596.
- Hougaard, P. (1986), ‘Survival models for heterogeneous populations derived from stable distributions’, *Biometrika* **73**(2), 387–396.
- Hughes, T. P., Kerry, J. T., Álvarez-Noriega, M., Álvarez-Romero, J. G., Anderson, K. D., Baird, A. H., Babcock, R. C., Beger, M., Bellwood, D. R., Berkelmans, R. et al. (2017),



- ‘Global warming and recurrent mass bleaching of corals’, *Nature* **543**(7645), 373–377.
- Huser, R. (2021), ‘EVA 2019 data competition on spatio-temporal prediction of Red Sea surface temperature extremes’, *Extremes* **24**, 91–104.
- Huser, R., Opitz, T. and Thibaud, E. (2017), ‘Bridging asymptotic independence and dependence in spatial extremes using Gaussian scale mixtures’, *Spatial Statistics* **21**, 166–186.
- Huser, R., Opitz, T. and Thibaud, E. (2021), ‘Max-infinitely divisible models and inference for spatial extremes’, *Scandinavian Journal of Statistics* **48**(1), 321–348.
- Huser, R., Opitz, T. and Wadsworth, J. L. (2024), ‘Modeling of spatial extremes in environmental data science: Time to move away from max-stable processes’, *arXiv preprint arXiv:2401.17430* .
- Huser, R., Stein, M. L. and Zhong, P. (2023), ‘Vecchia likelihood approximation for accurate and fast inference with intractable spatial max-stable models’, *Journal of Computational and Graphical Statistics* . To appear.
- Huser, R. and Wadsworth, J. L. (2019), ‘Modeling spatial processes with unknown extremal dependence class’, *Journal of the American Statistical Association* **114**(525), 434–444.
- Huser, R. and Wadsworth, J. L. (2022), ‘Advances in statistical modeling of spatial extremes’, *Wiley Interdisciplinary Reviews: Computational Statistics* **14**(1), e1537.
- Iuliano, E. and Quagliarella, D. (2013), ‘Proper orthogonal decomposition, surrogate modelling and evolutionary optimization in aerodynamic design’, *Computers & Fluids* **84**, 327–350.
- Keydana, S. (2023), *Deep Learning and Scientific Computing with R torch*, CRC Press.
- Kingma, D. P. and Welling, M. (2013), ‘Auto-encoding variational Bayes’, *arXiv preprint arXiv:1312.6114* .
- Kingma, D. P., Welling, M. et al. (2019), ‘An introduction to variational autoencoders’, *Foundations and Trends® in Machine Learning* **12**(4), 307–392.
- Krupskii, P. and Huser, R. (2022), ‘Modeling spatial tail dependence with cauchy convolution processes’, *Electronic Journal of Statistics* **16**(2), 6135–6174.
- Ledford, A. W. and Tawn, J. A. (1996), ‘Statistics for near independence in multivariate extreme values’, *Biometrika* **83**(1), 169–187.
- Matheson, J. E. and Winkler, R. L. (1976), ‘Scoring rules for continuous probability distributions’, *Management Science* **22**(10), 1087–1096.
- Nolan, J. P. (2020), ‘Univariate stable distributions’, *Springer Series in Operations Research and Financial Engineering*, DOI **10**, 978–3.
- Oesting, M. and Huser, R. (2022), ‘Patterns in spatio-temporal extremes’, *arXiv preprint arXiv:2212.11001* .
- Opitz, T. (2016), ‘Modeling asymptotically independent spatial extremes based on Laplace random fields’, *Spatial Statistics* **16**, 1–18.
- Padoan, S. A. (2013), ‘Extreme dependence models based on event magnitude’, *Journal of Multivariate Analysis* **122**, 1–19.

- Polyak, B. T. (1964), ‘Some methods of speeding up the convergence of iteration methods’, *USSR Computational Mathematics and Mathematical Physics* **4**(5), 1–17.
- Raitsos, D. E., Pradhan, Y., Brewin, R. J., Stenchikov, G. and Hoteit, I. (2013), ‘Remote sensing the phytoplankton seasonal succession of the Red Sea’, *PLoS One* **8**(6), e64909.
- Reich, B. J. and Shaby, B. A. (2012), ‘A hierarchical max-stable spatial model for extreme precipitation’, *The Annals of Applied Statistics* **6**(4), 1430–1451.
- Resnick, S. I. (2008), *Extreme Values, Regular Variation, and Point Processes*, Vol. 4, Springer Science & Business Media.
- Richards, J., Sainsbury-Dale, M., Zammit-Mangion, A. and Huser, R. (2023), ‘Likelihood-free neural Bayes estimators for censored peaks-over-threshold models’, *arXiv preprint arXiv:2306.15642*.
- Ruymgaart, F. H. (1974), ‘Asymptotic normality of nonparametric tests for independence’, *The Annals of Statistics* pp. 892–910.
- Ruymgaart, F. H. and van Zuijlen, M. (1978), ‘Asymptotic normality of multivariate linear rank statistics in the non-iid case’, *The Annals of Statistics* **6**(3), 588–602.
- Sainsbury-Dale, M., Zammit-Mangion, A. and Huser, R. (2024), ‘Likelihood-free parameter estimation with neural Bayes estimators’, *The American Statistician* **78**, 1–14.
- Sargsyan, K. (2017), Surrogate models for uncertainty propagation and sensitivity analysis, in ‘Handbook of uncertainty quantification’, Springer, pp. 673–698.
- Sen, P. K. and Puri, M. L. (1967), ‘On the theory of rank order tests for location in the multivariate one sample problem’, *The Annals of Mathematical Statistics* **38**(4), 1216–1228.
- Sharma, S., Gomez, M., Keller, K., Nicholas, R. E. and Mejia, A. (2021), ‘Regional flood risk projections under climate change’, *Journal of Hydrometeorology* **22**(9), 2259–2274.
- Simpson, E. S., Opitz, T. and Wadsworth, J. L. (2023), ‘High-dimensional modeling of spatial and spatio-temporal conditional extremes using INLA and Gaussian Markov random fields’, *Extremes* pp. 1–45.
- Simpson, E. S. and Wadsworth, J. L. (2021), ‘Conditional modelling of spatio-temporal extremes for Red Sea surface temperatures’, *Spatial Statistics* **41**, 100482.
- Sohn, K., Lee, H. and Yan, X. (2015), ‘Learning structured output representation using deep conditional generative models’, *Advances in Neural Information Processing Systems* **28**.
- Thibaud, E. and Opitz, T. (2015), ‘Efficient inference and simulation for elliptical Pareto processes’, *Biometrika* **102**(4), 855–870.
- Wadsworth, J. L. and Tawn, J. (2022), ‘Higher-dimensional spatial extremes via single-site conditioning’, *Spatial Statistics* **51**, 100677.
- Wendland, H. (1995), ‘Piecewise polynomial, positive definite and compactly supported radial functions of minimal degree’, *Advances in Computational Mathematics* **4**, 389.
- Zammit-Mangion, A., Sainsbury-Dale, M. and Huser, R. (2024), ‘Neural methods for amortised parameter inference’, *arXiv preprint arXiv:2404.12484*.

- Zhang, L., Risser, M. D., Molter, E. M., Wehner, M. F. and O'Brien, T. A. (2023), 'Accounting for the spatial structure of weather systems in detected changes in precipitation extremes', *Weather and Climate Extremes* **38**, 100499.
- Zhang, L., Shaby, B. A. and Wadsworth, J. L. (2022), 'Hierarchical transformed scale mixtures for flexible modeling of spatial extremes on datasets with many locations', *Journal of the American Statistical Association* **117**(539), 1357–1369.
- Zhong, P., Huser, R. and Opitz, T. (2022), 'Modeling nonstationary temperature maxima based on extremal dependence changing with event magnitude', *Annals of Applied Statistics* **16**, 272–299.

## A Comparison to existing spatial extremes models

Max-stable (Davison et al., 2012, 2019) or generalized Pareto processes (Ferreira and de Haan, 2014; Thibaud and Opitz, 2015) have the property that  $\chi_{ij}$  is always positive (Huser and Wadsworth, 2022). Conversely, Gaussian processes (or multivariate Gaussian distributions) have the property that  $\chi_{ij}(u)$  always converges to 0 as  $u \rightarrow 1$ , unless  $X_i$  and  $X_j$  are perfectly dependent.

By contrast, tail dependence in observed environmental processes often seems to decay as events get more extreme and rare events often tend to be more spatially localized as the intensity increases (Huser and Wadsworth, 2019). This was observed in numerous studies, including Dutch wind gust maxima (Huser et al., 2021), threshold exceedances of the daily Fosberg fire index (Zhang et al., 2022), and winter maximum precipitation data over the Midwest of the U.S. (Zhang et al., 2023), just to name a few examples. The stability property of max-stable and generalized Pareto models is thus often a physically inappropriate restriction in the joint tail. However, a weakening  $\chi_{ij}(u)$  as  $u$  increases does not necessarily lead to AI. As we extrapolate into the joint tail beyond the observed data, mis-classifying the tail dependence regime inevitably leads to inaccurate risk assessments. Therefore, we seek models that exhibit much more flexible tail characteristics and do not assume an extremal a dependence class *a priori*.

Bopp et al. (2021) proposed a max-id model that exhibits AI ( $\gamma_k \equiv \gamma > 0$ ) or AD ( $\gamma_k \equiv 0$ ) for all pairs of locations, depending on the tail dependence strength in the data. This is an improvement over Reich and Shaby (2012) in which the tilting parameters are set to  $\gamma_k \equiv 0$ ,  $k = 1, \dots, K$ . In both cases, they used the radial basis functions which are not compactly supported and the tilting parameters are fixed as a single constant at all knots. As a result, these processes only exhibit one dependence class for all pairs of locations and induce a form of long-range dependence; that is, they cannot capture a change of asymptotic dependence class as a function of distance.

In addition, both Reich and Shaby (2012) and Bopp et al. (2021) set  $\alpha_0 = \alpha$ , and their noise process  $\{\epsilon(\mathbf{s})\}$  has independent  $(1/\alpha)$ -Fréchet marginals, i.e., Fréchet(0, 1,  $1/\alpha$ ). While  $\alpha$  also determines the dependence properties of the process through the exponentially-tilted PS variables in  $\{Y(\mathbf{s})\}$ , the Fréchet(0, 1,  $1/\alpha$ ) variables usually end up being too noisy compared to the  $\{Y(\mathbf{s})\}$  process.

In our modification, we decouple the noise variance and the tail heaviness of latent variables. Specifically, the Fréchet(0,  $\tau$ ,  $1/\alpha_0$ ) distribution concentrates around  $\tau$  when the shape  $1/\alpha_0 > 1$  and scale  $\tau > 1$ , so that  $\epsilon(\mathbf{s})$  truly acts as a scaling factor that accounts for measurement errors for each time  $t$ . Moreover, the spatially-varying tilting parameters introduce tail dependence for two close-by locations, when they are covered by the same basis function. The local dependence strength is proportional to the tail-heaviness of the latent variable at the closest knot. As we show in Section 1.3, there is local AD if  $\gamma_k = 0$ , and there is local AI if  $\gamma_k > 0$ , as expected. In addition, the compactness of the basis function support automatically introduces long-range exact independence (thus, also asymptotic independence) for two far-apart stations that are impacted by disjoint sets of basis functions. Overall, the dependence structure of our model is thus both non-stationary

and highly flexible.

More importantly, the combination of the nonstationary max-id model with the VAE technique allows us to fit complicated spatial extremes process in exceptionally high dimensions. Beyond certain specific isolated exceptions, it is currently not possible to fit existing max-stable, inverted-max-stable, and other spatial extremes models using a full likelihood or Bayesian approach on a dataset of more than approximately 1,000 locations. Recent successes include [Huser et al. \(2023\)](#), who used the Vecchia approximation to make efficient inference on a 1000-dimensional max-stable process, [Simpson et al. \(2023\)](#) who used INLA to fit the spatial conditional extremes model in high dimensions, and [Sainsbury-Dale et al. \(2024\)](#) and [Richards et al. \(2023\)](#), who performed likelihood-free inference with neural Bayes estimators to fit various spatial extremes models on big data sets. However, [Sainsbury-Dale et al. \(2024\)](#) illustrated their method with a stationary process observed at about 700 locations, while [Richards et al. \(2023\)](#) fitted local stationary models to data sets of size up to about 1,000. By contrast, our approach considers fitting and simulating a globally non-stationary spatial extremes process, with parameters evolving over time, to a data set of unprecedented spatial dimension of more than 16,000 locations.

## B Technical details

### B.1 Properties of exponentially-tilted positive-stable variables

Before we proceed to prove Proposition 1.1, we first recall some useful results in [Hougaard \(1986\)](#) about positive-stable (PS) distributions and their exponentially-tilted variation. If  $Z \sim \text{expPS}(\alpha, 0)$ , we denote the density function by  $f_\alpha(z)$ ,  $z > 0$ . Then for  $\alpha \in (0, 1]$ , it has Laplace transform

$$L(s) = \mathbb{E}e^{-sZ} = \exp(-s^\alpha), \quad s \geq 0.$$

For an exponentially-tilted variable  $Z \sim \text{expPS}(\alpha, \gamma)$ , the Laplace transform becomes

$$L(s) = \mathbb{E}e^{-sZ} = \exp[-\{(\gamma + s)^\alpha - \gamma^\alpha\}], \quad s \geq 0, \quad \gamma \geq 0 \quad (\text{B.1})$$

and its density is

$$h(x; \alpha, \gamma) = \frac{f_\alpha(x) \exp(-\gamma x)}{\exp(-\gamma^\alpha)}, \quad x > 0.$$

**Lemma B.1.** *If  $Z \sim \text{expPS}(\alpha, 0)$  and  $\alpha \in (0, 1)$ , then  $Z \sim \text{Stable}\{\alpha, 1, \cos^{1/\alpha}(\pi\alpha/2), 0\}$  in the 1-parameterization ([Nolan, 2020](#)).*

*Proof.* From Proposition 3.2 of [Nolan \(2020\)](#), we know that the Laplace transform of  $Z \sim \text{Stable}(\alpha, 1, \xi, 0; 1)$ ,  $\alpha \in (0, 2]$ , is

$$\mathbb{E}e^{-sZ} = \begin{cases} \exp\{-\xi^\alpha (\sec \frac{\pi\alpha}{2}) s^\alpha\}, & \alpha \in (0, 1) \cup (1, 2], \\ \exp\{-\xi \frac{2}{\pi} s \log s\}, & \alpha = 1. \end{cases}$$

When  $\xi = |\cos \frac{\pi\alpha}{2}|^{1/\alpha}$ , the Laplace transform becomes

$$\mathbb{E}e^{-sZ} = \begin{cases} \exp(-s^\alpha), & \alpha \in (0, 1), \\ \exp(s^\alpha), & \alpha \in (1, 2]. \end{cases}$$

That is,  $Z \sim \text{expPS}(\alpha, 0)$  when  $\alpha \in (0, 1)$ .  $\square$

**Remark 3.** If  $\alpha = 1/2$ , then  $|\cos \frac{\pi\alpha}{2}|^{1/\alpha} = 1/2$  and  $Z \sim \text{Stable}(1/2, 1, 1/2, 0; 1)$ , which is equivalent to  $Z \sim \text{Lévy}(0, 1/2)$  or  $Z \sim \text{InvGamma}(1/2, 1/4)$ .

**Remark 4.** To facilitate the computation of the prior in Eq. (6), we follow the Monte Carlo integration steps in Section 4 of the Supplementary Material of [Bopp et al. \(2021\)](#) to calculate the density  $h(\cdot; \alpha, \gamma)$ .

## B.2 Proof of Proposition 1.1

*Proof of Proposition 1.1.* Since at the location  $\mathbf{s}_j$ ,

$$\begin{aligned} \Pr(X(\mathbf{s}_j) \leq x) &= \mathbb{E} \left\{ \Pr \left( \epsilon(\mathbf{s}_j) \leq \frac{x}{Y(\mathbf{s}_j)} \mid Z_1, \dots, Z_K \right) \right\} = \mathbb{E} \left[ \exp \left\{ - \left( \frac{\tau Y(\mathbf{s}_j)}{x} \right)^{\frac{1}{\alpha_0}} \right\} \mid Z_1, \dots, Z_K \right] \\ &= \mathbb{E} \exp \left\{ - \left( \frac{\tau}{x} \right)^{\frac{1}{\alpha_0}} \sum_{k=1}^K \omega_k(\mathbf{s}_j, r_k)^{\frac{1}{\alpha}} Z_k \right\} = \exp \left[ \sum_{k \in \mathcal{D}} \gamma_k^\alpha - \sum_{k=1}^K \left\{ \gamma_k + \left( \frac{\tau}{x} \right)^{\frac{1}{\alpha_0}} \omega_{kj}^{\frac{1}{\alpha}} \right\}^\alpha \right]. \end{aligned}$$

To study the tail decay of the survival function, we apply Taylor's expansion with the Peano remainder:

$$(1+t)^\alpha = 1 + \alpha t + \frac{\alpha(\alpha-1)}{2} t^2 + o(t^2), \text{ as } t \rightarrow 0. \quad (\text{B.2})$$

Then, as  $x \rightarrow \infty$ , we have

$$\begin{aligned} \sum_{k \in \mathcal{D}} \left\{ \gamma_k + \left( \frac{\tau}{x} \right)^{\frac{1}{\alpha_0}} \omega_{kj}^{\frac{1}{\alpha}} \right\}^\alpha &= \sum_{k \in \mathcal{D}} \gamma_k^\alpha \left\{ 1 + \left( \frac{\tau}{x} \right)^{\frac{1}{\alpha_0}} \frac{\omega_{kj}^{1/\alpha}}{\gamma_k} \right\}^\alpha \\ &= \sum_{k \in \mathcal{D}} \gamma_k^\alpha + \alpha \left( \frac{\tau}{x} \right)^{\frac{1}{\alpha_0}} \sum_{k \in \mathcal{D}} \frac{\omega_{kj}^{1/\alpha}}{\gamma_k^{1-\alpha}} + \frac{\alpha(\alpha-1)}{2} \left( \frac{\tau}{x} \right)^{\frac{2}{\alpha_0}} \sum_{k \in \mathcal{D}} \frac{\omega_{kj}^{2/\alpha}}{\gamma_k^{2-\alpha}} + o \left( x^{-\frac{2}{\alpha_0}} \right), \end{aligned}$$

which leads to

$$\begin{aligned} \sum_{k \in \mathcal{D}} \gamma_k^\alpha - \sum_{k=1}^K \left\{ \gamma_k + \left( \frac{\tau}{x} \right)^{\frac{1}{\alpha_0}} \omega_{kj}^{\frac{1}{\alpha}} \right\}^\alpha &= - \left( \frac{\tau}{x} \right)^{\frac{\alpha}{\alpha_0}} \sum_{k \in \mathcal{D}} \omega_{kj} - \alpha \left( \frac{\tau}{x} \right)^{\frac{1}{\alpha_0}} \sum_{k \in \mathcal{D}} \frac{\omega_{kj}^{1/\alpha}}{\gamma_k^{1-\alpha}} - \\ \frac{\alpha(\alpha-1)}{2} \left( \frac{\tau}{x} \right)^{\frac{2}{\alpha_0}} \sum_{k \in \mathcal{D}} \frac{\omega_{kj}^{2/\alpha}}{\gamma_k^{2-\alpha}} + o \left( x^{-\frac{2}{\alpha_0}} \right) &= -c'_j x^{-\frac{\alpha}{\alpha_0}} - c_j x^{-\frac{1}{\alpha_0}} - d_j x^{-\frac{2}{\alpha_0}} + o \left( x^{-\frac{2}{\alpha_0}} \right), \end{aligned} \quad (\text{B.3})$$

where the constants  $c'_j$ ,  $c_j$  and  $d_j$  are defined in Proposition 1.1.

Next we apply the following Taylor expansion:

$$1 - \exp(-t) = t - \frac{t^2}{2} + o(t^2), \text{ as } t \rightarrow 0. \quad (\text{B.4})$$

Combining (10) and (B.3) gives

$$\bar{F}_j(x) = c'_j x^{-\frac{\alpha}{\alpha_0}} + c_j x^{-\frac{1}{\alpha_0}} + d_j x^{-\frac{2}{\alpha_0}} - \frac{(c'_j x^{-\frac{\alpha}{\alpha_0}} + c_j x^{-\frac{1}{\alpha_0}} + d_j x^{-\frac{2}{\alpha_0}})^2}{2} + o\left(x^{-\frac{2}{\alpha_0}}\right),$$

from which we can expand the squared term and discard the terms with higher decaying rates than  $o(x^{-2/\alpha_0})$  to establish (11).  $\square$

*Proof of Corollary 1.1.1.* By definition,  $t^{-1} = \bar{F}_j\{q_j(t)\}$ . When  $\mathcal{C}_j \cap \mathcal{D} \neq \emptyset$ , (11) leads to

$$\begin{aligned} t^{-1} = c'_j q_j^{-\frac{\alpha}{\alpha_0}}(t) & \left[ 1 + \frac{c_j}{c'_j} q_j^{-\frac{1-\alpha}{\alpha_0}}(t) + \frac{1}{c'_j} \left( d_j - \frac{c_j^2}{2} \right) q_j^{-\frac{2-\alpha}{\alpha_0}}(t) - \right. \\ & \left. \frac{c'_j}{2} q_j^{-\frac{\alpha}{\alpha_0}}(t) - c_j q_j^{-\frac{1}{\alpha_0}}(t) + o\left\{ q_j^{-\frac{2-\alpha}{\alpha_0}}(t) \right\} \right] \text{ as } t \rightarrow \infty. \end{aligned} \quad (\text{B.5})$$

Since  $q_j(t) \rightarrow \infty$  as  $t \rightarrow \infty$ , the term in the square bracket of the previous display can simply be approximated by  $1 + o(1)$ . Thus, we have

$$q_j(t) = c'_j \frac{\alpha_0}{\alpha} t^{\frac{\alpha_0}{\alpha}} \{1 + o(1)\}. \quad (\text{B.6})$$

Since  $\alpha \in (0, 1)$ , we can also re-organize (B.5) to obtain

$$\begin{aligned} q_j(t) - c'_j \frac{\alpha_0}{\alpha} t^{\frac{\alpha_0}{\alpha}} & = q_j(t) \left( 1 - \left[ 1 + \frac{c_j}{c'_j} q_j^{-\frac{1-\alpha}{\alpha_0}}(t) - \frac{c'_j}{2} q_j^{-\frac{\alpha}{\alpha_0}}(t) + O\left\{ q_j^{-\frac{1}{\alpha_0}}(t) \right\} \right]^{-\frac{\alpha_0}{\alpha}} \right) \\ & = q_j(t) \left[ \frac{\alpha_0 c_j}{\alpha c'_j} q_j^{-\frac{1-\alpha}{\alpha_0}}(t) - \frac{\alpha_0 c'_j}{2\alpha} q_j^{-\frac{\alpha}{\alpha_0}}(t) + O\left\{ q_j^{-\frac{1}{\alpha_0}}(t) \right\} \right]. \end{aligned} \quad (\text{B.7})$$

On the last line, we applied the Taylor expansion in (B.2) again. Then we combine (B.6) and (B.7) to get

$$\begin{aligned} q_j(t) - c'_j \frac{\alpha_0}{\alpha} t^{\frac{\alpha_0}{\alpha}} & = c'_j \frac{\alpha_0}{\alpha} t^{\frac{\alpha_0}{\alpha}} \{1 + o(1)\} \left\{ \frac{\alpha_0 c_j}{\alpha c'_j{}^{1/\alpha}} t^{1-\frac{1}{\alpha}} - \frac{\alpha_0}{2\alpha} t^{-1} + O\left(t^{-\frac{1}{\alpha}}\right) \right\} \\ & = c'_j \frac{\alpha_0}{\alpha} t^{\frac{\alpha_0}{\alpha}} \left\{ \frac{\alpha_0 c_j}{\alpha c'_j{}^{1/\alpha}} t^{1-\frac{1}{\alpha}} - \frac{\alpha_0}{2\alpha} t^{-1} + O\left(t^{-\frac{1}{\alpha}}\right) \right\}, \end{aligned}$$

which concludes the proof for the first case.



Similarly, when  $\mathcal{C}_j \cap \mathcal{D} = \emptyset$ , we have

$$c_j^{\alpha_0} t^{\alpha_0} = q_j(t) \left[ 1 + \left( \frac{d_j}{c_j} - \frac{c_j}{2} \right) q_j^{-\frac{1}{\alpha_0}}(t) + o \left\{ q_j^{-\frac{1}{\alpha_0}}(t) \right\} \right]^{-\alpha_0} \text{ as } t \rightarrow \infty,$$

which ensures  $q_j(t) = c_j^{\alpha_0} t^{\alpha_0} \{1 + o(1)\}$ , and

$$\begin{aligned} q_j(t) - c_j^{\alpha_0} t^{\alpha_0} &= q_j(t) \left( 1 - \left[ 1 + \left( \frac{d_j}{c_j} - \frac{c_j}{2} \right) q_j^{-\frac{1}{\alpha_0}}(t) + o \left\{ q_j^{-\frac{1}{\alpha_0}}(t) \right\} \right]^{-\alpha_0} \right) \\ &= c_j^{\alpha_0} t^{\alpha_0} \{1 + o(1)\} \left[ \alpha_0 \left( \frac{d_j}{c_j} - \frac{c_j}{2} \right) q_j^{-\frac{1}{\alpha_0}}(t) + o \left\{ q_j^{-\frac{1}{\alpha_0}}(t) \right\} \right] \\ &= c_j^{\alpha_0} t^{\alpha_0} \left\{ \alpha_0 \left( \frac{d_j}{c_j} - \frac{1}{2} \right) t^{-1} + o(t^{-1}) \right\}. \end{aligned}$$

□

### B.3 Proof of Proposition 1.2

*Proof of Proposition 1.2.* The joint distribution for the discretization of  $\{X(\mathbf{s})\}$  is

$$\begin{aligned} F(x_1, \dots, x_n) &= \Pr(X(\mathbf{s}_1) \leq x_1, \dots, X(\mathbf{s}_{n_s}) \leq x_n) \\ &= \mathbb{E} \left\{ \Pr \left( \epsilon(\mathbf{s}_1) \leq \frac{x_1}{Y(\mathbf{s}_1)}, \dots, \epsilon(\mathbf{s}_{n_s}) \leq \frac{x_n}{Y(\mathbf{s}_{n_s})} \middle| Z_1, \dots, Z_K \right) \right\} \\ &= \mathbb{E} \left[ \prod_{j=1}^{n_s} \exp \left\{ - \left( \frac{\tau Y(\mathbf{s}_j)}{x_j} \right)^{\frac{1}{\alpha_0}} \right\} \middle| Z_1, \dots, Z_K \right] \\ &= \prod_{k=1}^K \mathbb{E} \exp \left\{ - \sum_{j=1}^{n_s} \omega_{kj}^{\frac{1}{\alpha_0}} \left( \frac{\tau}{x_j} \right)^{\frac{1}{\alpha_0}} Z_k \right\} = \exp \left[ \sum_{k \in \mathcal{D}} \gamma_k^\alpha - \sum_{k=1}^K \left\{ \gamma_k + \tau^{\frac{1}{\alpha_0}} \sum_{j=1}^{n_s} \frac{\omega_{kj}^{1/\alpha}}{x_j^{1/\alpha_0}} \right\}^\alpha \right], \end{aligned}$$

in which we utilized the Laplace transform of the exponentially-tilted PS variables displayed in Eq. (B.1). □

## B.4 Proof of Theorem 1.3

*Proof of Theorem 1.3.* By definitions of the tail dependence measures  $\chi_{ij}$  and  $\eta_{ij}$ ,

$$\begin{aligned}
\chi_{ij} &= \lim_{u \rightarrow 1} \frac{\Pr\{X(\mathbf{s}_i) > F_i^{-1}(u), X(\mathbf{s}_j) > F_j^{-1}(u)\}}{1 - u} \\
&= \lim_{t \rightarrow \infty} t \Pr\{X(\mathbf{s}_i) > q_i(t), X(\mathbf{s}_j) > q_j(t)\} \\
&= \lim_{t \rightarrow \infty} t \left[ 1 - 2 \left( 1 - \frac{1}{t} \right) + \Pr\{X(\mathbf{s}_i) \leq q_i(t), X(\mathbf{s}_j) \leq q_j(t)\} \right] \\
&= \lim_{t \rightarrow \infty} 2 - t [1 - F_{ij}\{q_i(t), q_j(t)\}],
\end{aligned} \tag{B.8}$$

and

$$\Pr\{X(\mathbf{s}_i) > q_i(t), X(\mathbf{s}_j) > q_j(t)\} = \mathcal{L}(t)t^{-1/\eta_{ij}}, \quad t \rightarrow \infty.$$

Further,

$$\lim_{t \rightarrow \infty} \frac{\log \Pr\{X(\mathbf{s}_i) > q_i(t), X(\mathbf{s}_j) > q_j(t)\}}{\log t} = -\frac{1}{\eta_{ij}}, \tag{B.9}$$

provided that

$$\lim_{t \rightarrow \infty} \frac{\log \mathcal{L}(t)}{\log t} = 0$$

for the slowly varying function  $\mathcal{L}$ . This can be easily shown using the Karamata Representation theorem (Resnick, 2008).

- (a) If  $\mathcal{C}_i \cap \mathcal{D} = \emptyset$  and  $\mathcal{C}_j \cap \mathcal{D} = \emptyset$ , we know from Corollary 1.1.1 that  $q_i(t) = c_i^{\alpha_0} t^{\alpha_0} \{1 + R_i(t) + o(t^{-1})\}$  and  $q_j(t) = c_j^{\alpha_0} t^{\alpha_0} \{1 + R_j(t) + o(t^{-1})\}$ , in which  $R_i(t) = \alpha_0(d_i/c_i^2 - 1/2)t^{-1}$  and  $R_j(t) = \alpha_0(d_j/c_j^2 - 1/2)t^{-1}$ . Similarly to Proposition 1.1, we first deduce

$$\begin{aligned}
\log F_{ij}\{q_i(t), q_j(t)\} &= \sum_{k \in \bar{\mathcal{D}}} \gamma_k^\alpha - \sum_{k=1}^K \left[ \gamma_k + \frac{\tau^{1/\alpha_0} \omega_{ki}^{1/\alpha}}{c_i t \{1 + R_i(t) + o(t^{-1})\}} + \frac{\tau^{1/\alpha_0} \omega_{kj}^{1/\alpha}}{c_j t \{1 + R_j(t) + o(t^{-1})\}} \right]^\alpha \\
&= \sum_{k \in \bar{\mathcal{D}}} \gamma_k^\alpha - \sum_{k \in \bar{\mathcal{D}}} \left[ \gamma_k + \frac{\tau^{1/\alpha_0} \omega_{ki}^{1/\alpha}}{c_i t} \{1 - R_i(t)\} + \frac{\tau^{1/\alpha_0} \omega_{kj}^{1/\alpha}}{c_j t} \{1 - R_j(t)\} + o\left(\frac{1}{t^2}\right) \right]^\alpha \\
&= \sum_{k \in \bar{\mathcal{D}}} \gamma_k^\alpha - \sum_{k \in \bar{\mathcal{D}}} \gamma_k^\alpha \left[ 1 + \frac{\alpha \tau^{1/\alpha_0} \omega_{ki}^{1/\alpha} / \gamma_k}{c_i t} \{1 - R_i(t)\} + \frac{\alpha \tau^{1/\alpha_0} \omega_{kj}^{1/\alpha} / \gamma_k}{c_j t} \{1 - R_j(t)\} + o\left(\frac{1}{t^2}\right) \right],
\end{aligned}$$

in which the Taylor expansion in Eq. (B.2) is applied. Recall the definitions of  $c_i$

and  $c_j$  in Proposition 1.1, and we find

$$\log F_{ij}\{q_i(t), q_j(t)\} = -\frac{2}{t} + \frac{R_i(t) + R_j(t)}{t} - o\left(\frac{1}{t^2}\right) \text{ as } t \rightarrow \infty.$$

Then it follows from Eq. (B.4) that

$$\begin{aligned} 1 - F_{ij}\{q_i(t), q_j(t)\} &= 1 - \exp\left\{-\frac{2}{t} + \frac{R_i(t) + R_j(t)}{t} - o\left(\frac{1}{t^2}\right)\right\} \\ &= \frac{2}{t} - \frac{R_i(t) + R_j(t)}{t} + o\left(\frac{1}{t^2}\right). \end{aligned}$$

Plugging this result into (B.8), we have  $\chi_{ij} = \lim_{t \rightarrow \infty} R_i(t) + R_j(t) + o(t^{-1}) = 0$ .

In the meantime,

$$\log \Pr\{X(\mathbf{s}_i) > q_i(t), X(\mathbf{s}_j) > q_j(t)\} \sim \log \frac{R_i(t) + R_j(t)}{t} = \log \alpha_0 \left( \frac{d_i}{c_i^2} + \frac{d_j}{c_j^2} - 1 \right) - 2 \log t$$

as  $t \rightarrow \infty$ . By Eq. (B.9),  $\eta_{ij} = 1/2$ .

- (b) If  $\mathcal{C}_i \cap \mathcal{D} = \emptyset$  and  $\mathcal{C}_j \cap \mathcal{D} \neq \emptyset$ , we know from Corollary 1.1.1 that  $q_i(t) \sim c_i^{\alpha_0} t^{\alpha_0} \{1 + R_i(t) + o(t^{-1})\}$  and  $q_j(t) \sim c_j^{\alpha_0/\alpha} t^{\alpha_0/\alpha} \{1 + R_j^*(t) + O(t^{-1/\alpha})\}$  as  $t \rightarrow \infty$ , in which  $R_i(t) = \alpha_0(d_i/c_i^2 - 1/2)t^{-1}$  and  $R_j^*(t) = \alpha_0 c_j t^{1-1/\alpha} / (\alpha c_j^{1/\alpha}) - \alpha_0 t^{-1} / (2\alpha)$ . Then

$$\begin{aligned} \log F_{ij}\{q_i(t), q_j(t)\} &= \sum_{k \in \bar{\mathcal{D}}} \gamma_k^\alpha - \sum_{k=1}^K \left\{ \gamma_k + \frac{\tau^{1/\alpha_0} \omega_{ki}^{1/\alpha}}{q_i^{1/\alpha_0}(t)} + \frac{\tau^{1/\alpha_0} \omega_{kj}^{1/\alpha}}{q_j^{1/\alpha_0}(t)} \right\}^\alpha \\ &= \sum_{k \in \bar{\mathcal{D}}} \gamma_k^\alpha - \sum_{k \in \bar{\mathcal{D}}} \left\{ \gamma_k + \frac{\tau^{1/\alpha_0} \omega_{ki}^{1/\alpha}}{q_i^{1/\alpha_0}(t)} + \frac{\tau^{1/\alpha_0} \omega_{kj}^{1/\alpha}}{q_j^{1/\alpha_0}(t)} \right\}^\alpha - \sum_{k \in \mathcal{D}} \frac{\tau^{\alpha/\alpha_0} \omega_{kj}}{q_j^{\alpha/\alpha_0}(t)} \\ &= \log F_j\{q_j(t)\} + \sum_{k \in \bar{\mathcal{D}}} \left\{ \gamma_k + \frac{\tau^{1/\alpha_0} \omega_{kj}^{1/\alpha}}{q_j^{1/\alpha_0}(t)} \right\}^\alpha - \sum_{k \in \bar{\mathcal{D}}} \left\{ \gamma_k + \frac{\tau^{1/\alpha_0} \omega_{ki}^{1/\alpha}}{q_i^{1/\alpha_0}(t)} + \frac{\tau^{1/\alpha_0} \omega_{kj}^{1/\alpha}}{q_j^{1/\alpha_0}(t)} \right\}^\alpha. \end{aligned} \tag{B.10}$$

For the two summations on the right, we split  $\bar{\mathcal{D}}$  into  $\mathcal{C}_j \cap \bar{\mathcal{D}}$  and  $\bar{\mathcal{D}} \setminus (\mathcal{C}_j \cap \bar{\mathcal{D}})$ :

$$\begin{aligned} &\sum_{k \in \mathcal{C}_j \cap \bar{\mathcal{D}}} \left\{ \gamma_k + \frac{\tau^{1/\alpha_0} \omega_{kj}^{1/\alpha}}{q_j^{1/\alpha_0}(t)} \right\}^\alpha - \sum_{k \in \mathcal{C}_j \cap \bar{\mathcal{D}}} \left\{ \gamma_k + \frac{\tau^{1/\alpha_0} \omega_{ki}^{1/\alpha}}{q_i^{1/\alpha_0}(t)} + \frac{\tau^{1/\alpha_0} \omega_{kj}^{1/\alpha}}{q_j^{1/\alpha_0}(t)} \right\}^\alpha = \\ &- \sum_{k \in \mathcal{C}_j \cap \bar{\mathcal{D}}} \frac{\alpha \tau^{1/\alpha_0} \omega_{ki}^{1/\alpha}}{\gamma_k^{1-\alpha} q_i^{1/\alpha_0}(t)} - \frac{\alpha(\alpha-1)}{2} \sum_{k \in \mathcal{C}_j \cap \bar{\mathcal{D}}} \frac{\tau^{2/\alpha_0}}{\gamma_k^{2-\alpha}} \left\{ \frac{\omega_{ki}^{2/\alpha}}{q_i^{2/\alpha_0}(t)} + \frac{2\omega_{ki}^{1/\alpha} \omega_{kj}^{1/\alpha}}{q_i^{1/\alpha_0}(t) q_j^{1/\alpha_0}(t)} \right\} + o\left(t^{-1-\frac{1}{\alpha}}\right) \end{aligned} \tag{B.11}$$

and

$$\begin{aligned} & \sum_{k \in \bar{\mathcal{D}} \setminus (\mathcal{C}_j \cap \bar{\mathcal{D}})} \left\{ \gamma_k + \frac{\tau^{1/\alpha_0} \omega_{kj}^{1/\alpha}}{q_j^{1/\alpha_0}(t)} \right\}^\alpha - \sum_{k \in \bar{\mathcal{D}} \setminus (\mathcal{C}_j \cap \bar{\mathcal{D}})} \left\{ \gamma_k + \frac{\tau^{1/\alpha_0} \omega_{ki}^{1/\alpha}}{q_i^{1/\alpha_0}(t)} + \frac{\tau^{1/\alpha_0} \omega_{kj}^{1/\alpha}}{q_j^{1/\alpha_0}(t)} \right\}^\alpha \\ & \sum_{k \in \bar{\mathcal{D}} \setminus (\mathcal{C}_j \cap \bar{\mathcal{D}})} \gamma_k^\alpha - \sum_{k \in \bar{\mathcal{D}} \setminus (\mathcal{C}_j \cap \bar{\mathcal{D}})} \left\{ \gamma_k + \frac{\tau^{1/\alpha_0} \omega_{ki}^{1/\alpha}}{q_i^{1/\alpha_0}(t)} \right\}^\alpha. \end{aligned} \quad (\text{B.12})$$

Feeding Eqs. (B.11) and (B.12) back into (B.10), we have

$$\log F_{ij}\{q_i(t), q_j(t)\} = \log F_j\{q_j(t)\} + \log F_i\{q_i(t)\} + \frac{c_{ij}}{q_i^{1/\alpha_0}(t)q_j^{1/\alpha_0}(t)} + o\left(t^{-1-\frac{1}{\alpha}}\right) \text{ as } t \rightarrow \infty,$$

in which  $c_{ij} = \alpha(\alpha - 1)\tau^{2/\alpha_0} \sum_{k \in \mathcal{C}_i \cap \mathcal{C}_j} \gamma_k^{\alpha-2} \omega_{ki}^{1/\alpha} \omega_{kj}^{1/\alpha}$ .

Then it follows from Eqs. (B.4) and (B.8) that

$$\begin{aligned} 1 - F_{ij}\{q_i(t), q_j(t)\} &= 1 - \exp \left[ \log F_j\{q_j(t)\} + \log F_i\{q_i(t)\} + \frac{c_{ij}}{q_i^{1/\alpha_0}(t)q_j^{1/\alpha_0}(t)} + o\left(t^{-1-\frac{1}{\alpha}}\right) \right] \\ &= -\log F_j\{q_j(t)\} - \log F_i\{q_i(t)\} - \frac{c_{ij}}{q_i^{1/\alpha_0}(t)q_j^{1/\alpha_0}(t)} + o\left(t^{-1-\frac{1}{\alpha}}\right) \\ &= -\log\left(1 - \frac{1}{t}\right) - \log\left(1 - \frac{1}{t}\right) - \frac{c_{ij}}{q_i^{1/\alpha_0}(t)q_j^{1/\alpha_0}(t)} + o\left(t^{-1-\frac{1}{\alpha}}\right) \\ &= \frac{2}{t} - \frac{c_{ij}}{c_i c_j^{1/\alpha} t^{1+1/\alpha}} + o\left(t^{-1-\frac{1}{\alpha}}\right) \end{aligned}$$

Therefore,  $\Pr\{X(\mathbf{s}_i) > q_i(t), X(\mathbf{s}_j) > q_j(t)\} = \frac{c_{ij}}{c_i c_j^{1/\alpha}} t^{-1-1/\alpha} + o\left(t^{-1-1/\alpha}\right)$ . Then it follows from Eqs. (B.8) and (B.9) that  $\xi_{ij} = 0$  and  $\eta_{ij} = 1/2$ .

(c) When  $\mathcal{C}_i \cap \mathcal{D} \neq \emptyset$  and  $\mathcal{C}_j \cap \mathcal{D} \neq \emptyset$ , we have  $q_i(t) \sim c_i^{\alpha_0/\alpha} t^{\alpha_0/\alpha} \{1 + O(t^{1-1/\alpha})\}$  and

$q_j(t) \sim c_j^{\prime\alpha_0/\alpha} t^{\alpha_0/\alpha} \{1 + O(t^{1-1/\alpha})\}$  as  $t \rightarrow \infty$ . Then

$$\begin{aligned}
\log F_{ij}\{q_i(t), q_j(t)\} &= \sum_{k \in \bar{\mathcal{D}}} \gamma_k^\alpha - \sum_{k=1}^K \left\{ \gamma_k + \frac{\tau^{1/\alpha_0} \omega_{ki}^{1/\alpha}}{q_i^{1/\alpha_0}(t)} + \frac{\tau^{1/\alpha_0} \omega_{kj}^{1/\alpha}}{q_j^{1/\alpha_0}(t)} \right\}^\alpha \\
&= \sum_{k \in \bar{\mathcal{D}}} \gamma_k^\alpha - \sum_{k=1}^K \left[ \gamma_k + \frac{\tau^{1/\alpha_0} \omega_{ki}^{1/\alpha} t^{-1/\alpha}}{c_i^{\prime 1/\alpha} \{1 + O(t^{1-1/\alpha})\}^{1/\alpha_0}} + \frac{\tau^{1/\alpha_0} \omega_{kj}^{1/\alpha} t^{-1/\alpha}}{c_j^{\prime 1/\alpha} \{1 + O(t^{1-1/\alpha})\}^{1/\alpha_0}} \right]^\alpha \\
&= \sum_{k \in \bar{\mathcal{D}}} \gamma_k^\alpha - \sum_{k=1}^K \left[ \gamma_k + \tau^{\frac{1}{\alpha_0}} \left( \frac{\omega_{ki}^{1/\alpha}}{c_i^{\prime 1/\alpha}} + \frac{\omega_{kj}^{1/\alpha}}{c_j^{\prime 1/\alpha}} \right) t^{-\frac{1}{\alpha}} + O\left(t^{1-\frac{2}{\alpha}}\right) \right]^\alpha \\
&= \sum_{k \in \bar{\mathcal{D}}} \gamma_k^\alpha - \sum_{k \in \bar{\mathcal{D}}} \left[ \gamma_k^\alpha + \frac{\alpha \tau^{1/\alpha_0}}{\gamma_k^{1-\alpha}} \left( \frac{\omega_{ki}^{1/\alpha}}{c_i^{\prime 1/\alpha}} + \frac{\omega_{kj}^{1/\alpha}}{c_j^{\prime 1/\alpha}} \right) t^{-\frac{1}{\alpha}} + O\left(t^{1-\frac{2}{\alpha}}\right) \right] - \\
&\quad \tau^{\frac{\alpha}{\alpha_0}} \sum_{k \in \mathcal{D}} \left( \frac{\omega_{ki}^{1/\alpha}}{c_i^{\prime 1/\alpha}} + \frac{\omega_{kj}^{1/\alpha}}{c_j^{\prime 1/\alpha}} \right)^\alpha t^{-1} - O(t^{1-\frac{2}{\alpha}}) \\
&= -d_{ij} t^{-1} - \left( \frac{c_i}{c_i^{\prime 1/\alpha}} + \frac{c_j}{c_j^{\prime 1/\alpha}} \right) t^{-\frac{1}{\alpha}} - O(t^{1-\frac{2}{\alpha}}), \text{ as } t \rightarrow \infty.
\end{aligned}$$

It follows from (B.8) that

$$\begin{aligned}
1 - F_{ij}\{q_i(t), q_j(t)\} &= 1 - \exp \left\{ -d_{ij} t^{-1} - \left( \frac{c_i}{c_i^{\prime 1/\alpha}} + \frac{c_j}{c_j^{\prime 1/\alpha}} \right) t^{-\frac{1}{\alpha}} - O(t^{1-\frac{2}{\alpha}}) \right\} \\
&= d_{ij} t^{-1} + \left( \frac{c_i}{c_i^{\prime 1/\alpha}} + \frac{c_j}{c_j^{\prime 1/\alpha}} \right) t^{-\frac{1}{\alpha}} + O(t^{1-\frac{2}{\alpha}}),
\end{aligned}$$

and

$$t \Pr\{X(\mathbf{s}_i) > q_i(t), X(\mathbf{s}_j) > q_j(t)\} = 2 - d_{ij} - \left( \frac{c_i}{c_i^{\prime 1/\alpha}} + \frac{c_j}{c_j^{\prime 1/\alpha}} \right) t^{1-\frac{1}{\alpha}} - O(t^{2-\frac{2}{\alpha}}),$$

as  $t \rightarrow \infty$ , in which  $d_{ij} = \tau^{\alpha/\alpha_0} \sum_{k \in \mathcal{D}} \{(\omega_{ki}/c_i^{\prime})^{1/\alpha} + (\omega_{kj}/c_j^{\prime})^{1/\alpha}\}^\alpha \in (1, 2)$ .

If  $\mathcal{C}_i \cap \mathcal{C}_j \neq \emptyset$ , we know from (B.8) that  $\chi_{ij} = 2 - d_{ij} \in (0, 1)$  and

$$\chi_{ij}(u) - \chi_{ij} = \left( \frac{c_i}{c_i^{\prime 1/\alpha}} + \frac{c_j}{c_j^{\prime 1/\alpha}} \right) (1-u)^{\frac{1}{\alpha}-1} + O\left\{(1-u)^{\frac{2}{\alpha}-2}\right\}.$$

□

**Remark 5.** *The exponent function, defined by*

$$V(x_1, \dots, x_{n_s}) = \lim_{t \rightarrow \infty} t(1 - F[F_1^{-1}\{1 - (tx_1)^{-1}\}, \dots, F_{n_s}^{-1}\{1 - (tx_{n_s})^{-1}\}]),$$

is a limiting measure that occurs in the limiting distribution for normalized maxima. It is used to describe the multivariate extremal dependence of a spatial process, and the  $n_s$ -dimensional extremal coefficient  $V(1, \dots, 1)$  is of particular interest. This extremal coefficient has a range of  $[1, n_s]$ , with the lower and upper ends indicating, respectively, perfect dependence and independence. As a polarized case, if  $\gamma_k > 0$ , for all  $k = 1, \dots, K$ , then  $\mathcal{C}_j \cap \mathcal{D} = \emptyset$  for all  $j$ 's, and thus we have

$$\gamma_k^\alpha - \left\{ \gamma_k + \tau^{\frac{1}{\alpha_0}} \sum_{j=1}^{n_s} \frac{\omega_{kj}^{1/\alpha}}{q_j^{1/\alpha_0}(t)} \right\}^\alpha \sim \alpha \tau^{\frac{1}{\alpha_0}} \gamma_k^{\alpha-1} \sum_{j=1}^{n_s} \frac{\omega_{kj}^{1/\alpha}}{q_j^{1/\alpha_0}(t)}, \quad t \rightarrow \infty.$$

Here, we can approximate  $q_j(t)$  using the results from Corollary 1.1.1. From Proposition 1.1, we can deduce that  $V(1, \dots, 1) = n_s$ , which corresponds to joint extremal independence. By contrast, if all  $\gamma_k = 0$  and one knot covers the entire spatial domain, we have  $V(1, \dots, 1) \in (1, n_s)$ , which corresponds to joint extremal dependence.

## C Areal radius of exceedance

### C.1 Monte Carlo estimates of $\text{ARE}_{\psi}(u)$

*Proof of Theorem 2.1.* It suffices to prove that

$$\lim_{n_r \rightarrow \infty} \frac{\sum_{r=1}^{n_r} \mathbb{1}(U_{ir} > u, U_{0r} > u)}{\sum_{r=1}^{n_r} \mathbb{1}(U_{0r} > u)} = \chi_{\mathbf{s}_0, \mathbf{g}_i}(u), \quad \text{a.s.} \quad (\text{C.1})$$

for all  $i = 1, \dots, n_g$ .

First, since  $U_{0r'} = \hat{F}_0(X_{0r'})$ , it is clear that

$$n_r U_{0r'} = \sum_{r=1}^{n_r} \mathbb{1}\{X_{0r} \leq X_{0r'}\}$$

is the rank of  $X_{0r'}$  in  $\mathbf{X}_0$ ,  $r' = 1, \dots, n_r$ . Thus,

$$\frac{1}{n_r} \sum_{r=1}^{n_r} \mathbb{1}(U_{0r} > u) = \frac{\lfloor n_r(1-u) \rfloor}{n_r} \rightarrow 1-u, \quad \text{as } n_r \rightarrow \infty, \quad (\text{C.2})$$

in which  $\lfloor \cdot \rfloor$  is the floor function.

Second, denote the rank of  $X_{ir'}$  in  $\mathbf{X}_i$  by  $R_{ir'}$ ,  $r' = 1, \dots, n_r$ ,  $i = 1, \dots, n_g$ . Then we know  $R_{ir'} = n_r U_{ir'}$  and

$$S_{i0} := \frac{1}{n_r} \sum_{r=1}^{n_r} \mathbb{1}(U_{ir} > u, U_{0r} > u) = \frac{1}{n_r} \sum_{r=1}^{n_r} \mathbb{1} \left\{ \frac{R_{ir}}{n_r} > u \right\} \mathbb{1} \left\{ \frac{R_{0r}}{n_r} > u \right\},$$

This is thus a bivariate linear rank statistics of  $\mathbf{X}_i$  and  $\mathbf{X}_0$ , for which the regression constants as defined in [Sen and Puri \(1967\)](#) all have a value of 1 and the scores have a product structure with each term being generated by  $\phi(x) = \mathbb{1}\{x > u\}$ ,  $x \in (0, 1)$ . [Sen and Puri \(1967\)](#) and [Ruymgaart \(1974\)](#) established the asymptotic normality of the multivariate linear rank statistics under weak restrictions that asymptotically no individual regression constant is much larger than the other constants and that  $\phi$  is square integrable on  $(0, 1)^2$ ; that is,

$$0 < \int_{(0,1)^2} \{\phi(u_1, u_2) - \bar{\phi}\}^2 du_1 du_2 < \infty \text{ with } \bar{\phi} = \int_0^1 \phi(u) du,$$

in which  $\phi(u_1, u_2) = \phi(u_1)\phi(u_2)$ . Since our regression constants are all 1's, the restriction on the regression constants is easily satisfied. Also, for  $\phi(u_1, u_2) = \mathbb{1}\{u_1 > u, u_2 > u\}$ ,  $\int_0^1 \int_0^1 \{\phi(u_1, u_2) - \bar{\phi}\}^2 du_1 du_2 = \bar{\phi} - \bar{\phi}^2$  with  $\bar{\phi} = (1 - u)^2$ . Therefore,

$$n^{1/2}\{S_{i0} - \mu_{i0}\} \rightarrow_d N(0, \sigma_{i0}^2) \quad (\text{C.3})$$

as  $n_r \rightarrow \infty$ , in which  $\mu_{i0}$  and  $\sigma_{i0}^2$  can be derived using Eq. (1.3) and (3.5) in [Ruymgaart \(1974\)](#) as

$$\begin{aligned} \mu_{i0} &= \int \int \phi(F_i(x))\phi(F_0(y))dF_{i0}(x, y) = \Pr\{F_i(X_i) > u, F_0(X_0) > u\}, \\ \sigma_{i0}^2 &= \text{Var}(\mathbb{1}\{F_i(X_i) > u, F_0(X_0) > u\} + [\mathbb{1}\{F_i(X_i) \leq u\} - u]\Pr\{F_0(X_0) > u \mid F_i(X_i) = u\} \\ &\quad + [\mathbb{1}\{F_0(X_0) \leq u\} - u]\Pr\{F_i(X_i) > u \mid F_0(X_0) = u\}). \end{aligned} \quad (\text{C.4})$$

Since  $\mu_{i0}/(1 - u) = \chi_{0i}(u)$ , we know from Expressions (C.2) and (C.3) that as  $n_r \rightarrow \infty$ ,

$$n^{\frac{1}{2}} \left\{ \frac{\sum_{r=1}^{n_r} \mathbb{1}(U_{ir} > u, U_{0r} > u)}{\sum_{r=1}^{n_r} \mathbb{1}(U_{0r} > u)} - \chi_{s_0, g_i}(u) \right\} \rightarrow_d N \left\{ 0, \frac{\sigma_{i0}^2}{(1 - u)^2} \right\}, \quad (\text{C.5})$$

which ensures Expression (C.1). □

**Remark 6.** From Expression (C.5), we see that the asymptotic normality of  $n^{1/2}\{\widehat{\text{ARE}}_{\psi}(u) - \text{ARE}_{\psi}(u)\}$  is also guaranteed. However, the exact expression of its asymptotic variance requires a much more careful examination of the correlations among the ranks of  $\mathbf{X}_i$ ,  $i = 0, 1, \dots, n_g$ ; that is, we need to devise a multivariate linear rank statistics of  $\mathbf{X}_i$ ,  $i = 0, 1, \dots, n_g$ ; see [Ruymgaart and van Zuijlen \(1978\)](#).

## C.2 Convergence of $\text{ARE}_{\psi}(u)$

*Proof of Theorem 2.2.* By the definition of the tail dependence measure in Eq. (9),

$$\lim_{u \rightarrow 1} \sum_{i=1}^{n_g} \chi_{0i}(u) = \sum_{i=1}^{n_g} \chi_{0i}.$$

It is clear that the right-hand side is the Riemann sum of  $\chi_{\mathbf{s}_0, \mathbf{s}}$  as a function of  $\mathbf{s}$  with respect to the grid. Since  $\chi_{\mathbf{s}_0, \mathbf{s}}$  is a continuous function of  $\mathbf{s}$  (i.e., Riemann-integrable), we have

$$\lim_{\psi \rightarrow 0} \psi^2 \sum_{i=1}^{n_g} \chi_{0i} = \int_{\mathcal{S}} \chi_{\mathbf{s}_0, \mathbf{s}} d\mathbf{s}.$$

Therefore, we have

$$\lim_{\psi \rightarrow 0, u \rightarrow 1} \psi \left( \sum_{i=1}^{n_g} \chi_{0i}(u) \right)^{1/2} = \left\{ \int_{\mathcal{S}} \chi_{\mathbf{s}_0, \mathbf{s}} d\mathbf{s} \right\}^{1/2}.$$

□

**Remark 7.** In the spatial extremes literature, many models that have a spatially-invariant set of dependence parameter  $\phi_d$  and they satisfy

$$\chi_{\mathbf{s}_0, \mathbf{s}}(u) - \chi_{\mathbf{s}_0, \mathbf{s}} = c(\mathbf{s}_0, \mathbf{s}, \phi_d)(1-u)^{d(\phi_d)}\{1+o(1)\},$$

where  $c(\mathbf{s}_0, \mathbf{s}, \phi_d)$  is multiplicative constant defined by  $\mathbf{s}$ ,  $\mathbf{s}_0$  and  $\phi_d$ . Also, the rate of decay  $d(\phi_d)$  is independent of  $\mathbf{s}$  and  $\mathbf{s}_0$ . Such examples include the models proposed by [Huser et al. \(2017\)](#), [Huser and Wadsworth \(2019\)](#) and [Bopp et al. \(2021\)](#). In this case,

$$\pi \widehat{\text{ARE}}_{\psi}^2(u) - \psi^2 \sum_{i=1}^{n_g} \chi_{\mathbf{s}_0, \mathbf{g}_i} \approx \left\{ \psi^2 \sum_{i=1}^{n_g} c(\mathbf{s}_0, \mathbf{g}_i, \phi_d) \right\} (1-u)^{d(\phi_d)}\{1+o(1)\}.$$

That is,  $\widehat{\text{ARE}}_{\psi}(u)$  has similar decaying behaviors as  $\chi_{\mathbf{s}_0, \mathbf{s}}(u)$ , which was observed empirically in Figure 3(b) and 4(b) in [Zhang et al. \(2023\)](#).

**Remark 8.** We note that [Cotsakis et al. \(2022\)](#) proposed a similar metric which measures the length of the perimeter of excursion sets of anisotropic random fields on  $\mathbb{R}^2$  under some smoothness assumptions. This estimator acts on the empirically accessible binary digital images of the excursion regions and computes the length of a piecewise linear approximation of the excursion boundary. In their work, the main focus is to prove strong consistency of the perimeter estimator as the image pixel size tends to zero. In comparison, we show that our estimator of  $\text{ARE}_{\psi}(u)$  is strongly consistent as the number of replicates drawn from the process  $\{X(\mathbf{s})\}$  approaches infinity. Furthermore, the length scale  $\text{ARE}_{\psi}(u)$  is, in our view, more interpretable than the perimeter of excursion sets. Also,  $\text{ARE}_{\psi}(u)$  is closely tied to the bivariate  $\chi$  measure, which further bridges spatial extremes to applications in other fields.

## D XVAE details

In this section, we will illustrate the details of Eqs. (5) and (8). Recall the encoder in the XVAE encodes the information in  $\mathbf{x}_t$ ,  $t = 1, \dots, n_t$ , using a three-layer perceptron neural



network. The three-layer perceptron neural network has the form of:

$$\begin{aligned}
\mathbf{h}_{1,t} &= \text{relu}(\mathbf{W}_1 \mathbf{x}_t + \mathbf{b}_1), \\
\mathbf{h}_{2,t} &= \text{relu}(\mathbf{W}_2 \mathbf{h}_{1,t} + \mathbf{b}_2), \\
\log \zeta_t^2 &= \mathbf{W}_3 \mathbf{h}_{2,t} + \mathbf{b}_3, \\
\boldsymbol{\mu}_t &= \text{relu}(\mathbf{W}_4 \mathbf{h}_{2,t} + \mathbf{b}_4).
\end{aligned} \tag{D.1}$$

The weights  $\{\mathbf{W}_1, \dots, \mathbf{W}_4\}$  and biases  $\{\mathbf{b}_1, \dots, \mathbf{b}_4\}$  combined are denoted by  $\phi_e$  and are shared across time replicates. Here,  $\mathbf{W}_1$  is a  $K \times n_s$  weight matrix and  $\mathbf{W}_2, \dots, \mathbf{W}_4$  are all  $K \times K$  matrices, and  $\mathbf{b}_1, \dots, \mathbf{b}_4$  are all  $K \times 1$  vectors. Then we use a Gaussian encoder  $\mathbf{z}_t \sim N\{\boldsymbol{\mu}_t, \text{diag}(\zeta_t^2)\}$  and we have

$$q_{\phi_e}(\mathbf{z}_t | \mathbf{x}_t) = \frac{1}{(2\pi)^{n/2} \prod_{k=1}^K \zeta_{kt}} \exp \left\{ - \sum_{k=1}^K \frac{(z_{kt} - \mu_{kt})^2}{2\zeta_{kt}^2} \right\}. \tag{D.2}$$

For the decoder, we also use a three-layer perceptron neural network:

$$\begin{aligned}
\mathbf{l}_{1,t} &= \text{relu}(\mathbf{W}_5 \mathbf{z}_t + \mathbf{b}_5), \\
\mathbf{l}_{2,t} &= \text{relu}(\mathbf{W}_6 \mathbf{l}_{1,t} + \mathbf{b}_6), \\
(\alpha_t, \boldsymbol{\gamma}_t^T)^T &= \text{relu}(\mathbf{W}_7 \mathbf{l}_{2,t} + \mathbf{b}_7), \\
\mathbf{y}_t &= (\boldsymbol{\Omega}^{1/\alpha_t} \mathbf{z}_t)^{\alpha_0},
\end{aligned} \tag{D.3}$$

in which  $\boldsymbol{\Omega} = (\mathbf{w}_1, \dots, \mathbf{w}_{n_s})^T$  is a  $n_s \times K$  matrix with its  $j$ th row being  $\mathbf{w}_j^T = (\omega_{1j}, \dots, \omega_{Kj})$ . The weights  $\{\mathbf{W}_5, \dots, \mathbf{W}_7\}$  and biases  $\{\mathbf{b}_5, \dots, \mathbf{b}_7\}$  combined are denoted by  $\phi_d$ , in which  $\mathbf{W}_5$  and  $\mathbf{W}_6$  are both  $K \times K$  matrices while  $\mathbf{W}_7$  is a  $(K+1) \times K$  matrix, and  $\mathbf{b}_5$  and  $\mathbf{b}_6$  are  $K \times 1$  vectors while  $\mathbf{b}_7$  is a  $(K+1) \times 1$  vector.

## D.1 Reparameterization trick

Recall that the ELBO is defined as

$$\mathcal{L}_{\phi_e, \phi_d}(\mathbf{x}_t) = \mathbb{E}_{q_{\phi_e}(\mathbf{z}_t | \mathbf{x}_t)} \left\{ \log \frac{p_{\phi_d}(\mathbf{x}_t, \mathbf{Z}_t)}{q_{\phi_e}(\mathbf{Z}_t | \mathbf{x}_t)} \right\},$$

which can be approximated using Monte Carlo as shown in Eq. (2). However, it is not straightforward to approximate the partial derivative of the ELBO with respect to  $\phi_e$  (denoted by  $\nabla_{\phi_e} \mathcal{L}_{\phi_e, \phi_d}$ ), which is needed in the stochastic gradient descent algorithm. Since the expectation in ELBO is taken under the distribution  $q_{\phi_e}(\mathbf{z}_t | \mathbf{x}_t)$ .

$$\nabla_{\phi_e} \mathcal{L}_{\phi_e, \phi_d}(\mathbf{x}_t) \neq \mathbb{E}_{q_{\phi_e}(\mathbf{z}_t | \mathbf{x}_t)} \left\{ \nabla_{\phi_e} \log \frac{p_{\phi_d}(\mathbf{x}_t, \mathbf{Z}_t)}{q_{\phi_e}(\mathbf{Z}_t | \mathbf{x}_t)} \right\},$$

To simplify the gradient of the ELBO with respect to  $\phi_e$ , we express  $\mathbf{Z}_t$  in terms of a

random vector  $\boldsymbol{\eta}_t$  that is independent of  $\mathbf{x}_t$  and  $\boldsymbol{\phi}_e$ :

$$\mathbf{Z}_t = \boldsymbol{\mu}_t + \boldsymbol{\zeta}_t \odot \boldsymbol{\eta}_t,$$

in which  $\boldsymbol{\eta}_t = (\eta_{1t}, \eta_{2t}, \dots, \eta_{Kt})^T$  and  $\eta_{kt} \stackrel{\text{i.i.d.}}{\sim} N(0, 1)$ . As a consequence, the Jacobian of the transformation from  $\mathbf{Z}_t$  to  $\boldsymbol{\eta}_t$  is

$$J(\boldsymbol{\eta}_t) = \frac{\partial \mathbf{z}_t}{\partial \boldsymbol{\eta}_t} = \text{diag}(\boldsymbol{\zeta}_t),$$

and we can apply a change-of-variable formula to the multiple integral in the ELBO:

$$\begin{aligned} \mathcal{L}_{\phi_e, \phi_d}(\mathbf{x}_t) &= \int \log \frac{p_{\phi_d}(\mathbf{x}_t, \mathbf{z}_t)}{q_{\phi_e}(\mathbf{z}_t | \mathbf{x}_t)} q_{\phi_e}(\mathbf{z}_t | \mathbf{x}_t) d\mathbf{z}_t \\ &= \int \log \frac{p_{\phi_d}(\mathbf{x}_t, \boldsymbol{\mu}_t + \boldsymbol{\zeta}_t \odot \boldsymbol{\eta}_t)}{q_{\phi_e}(\boldsymbol{\mu}_t + \boldsymbol{\zeta}_t \odot \boldsymbol{\eta}_t | \mathbf{x}_t)} q_{\phi_e}(\boldsymbol{\mu}_t + \boldsymbol{\zeta}_t \odot \boldsymbol{\eta}_t | \mathbf{x}_t) |\det\{J(\boldsymbol{\eta}_t)\}| d\boldsymbol{\eta}_t \\ &= \int \log \frac{p_{\phi_d}(\mathbf{x}_t, \boldsymbol{\mu}_t + \boldsymbol{\zeta}_t \odot \boldsymbol{\eta}_t)}{q_{\phi_e}(\boldsymbol{\mu}_t + \boldsymbol{\zeta}_t \odot \boldsymbol{\eta}_t | \mathbf{x}_t)} \prod_{k=1}^K \frac{\exp(-\eta_{kt}^2/2)}{2\pi} d\boldsymbol{\eta}_t = \mathbb{E}_{p(\boldsymbol{\eta}_t)} \left\{ \log \frac{p_{\phi_d}(\mathbf{x}_t, \boldsymbol{\mu}_t + \boldsymbol{\zeta}_t \odot \boldsymbol{\eta}_t)}{q_{\phi_e}(\boldsymbol{\mu}_t + \boldsymbol{\zeta}_t \odot \boldsymbol{\eta}_t | \mathbf{x}_t)} \right\}. \end{aligned}$$

On the last line, we plugged  $\mathbf{Z}_t = \boldsymbol{\mu}_t + \boldsymbol{\zeta}_t \odot \boldsymbol{\eta}_t$  in Eq. (D.2) to obtain the clean form, and  $p(\boldsymbol{\eta}_t)$  denotes the joint density of  $K$  independent standard normal variables. Therefore, we can now form simple Monte Carlo estimators of  $\mathcal{L}_{\phi_e, \phi_d}$ ,  $\nabla_{\phi_e} \mathcal{L}_{\phi_e, \phi_d}$ , and  $\nabla_{\phi_d} \mathcal{L}_{\phi_e, \phi_d}$ . More specifically,

$$\begin{aligned} \mathcal{L}_{\phi_e, \phi_d}(\mathbf{x}_t) &\approx \frac{1}{L} \sum_{l=1}^L \log \frac{p_{\phi_d}(\mathbf{x}_t, \boldsymbol{\mu}_t + \boldsymbol{\zeta}_t \odot \boldsymbol{\eta}^l)}{q_{\phi_e}(\boldsymbol{\mu}_t + \boldsymbol{\zeta}_t \odot \boldsymbol{\eta}^l | \mathbf{x}_t)} \\ &= \frac{1}{L} \sum_{l=1}^L \log p_{\phi_d}(\mathbf{x}_t | \mathbf{Z}^l) + \frac{1}{L} \sum_{l=1}^L \log p_{\phi_d}(\mathbf{Z}^l) - \frac{1}{L} \sum_{l=1}^L \log p(\boldsymbol{\eta}^l) + \sum_{k=1}^K \log \zeta_{kt}, \end{aligned}$$

where  $\boldsymbol{\eta}^l$ ,  $l = 1, \dots, L$ , are independent draws from  $N(\mathbf{0}_K, \mathbf{I}_{K \times K})$  and  $\mathbf{Z}^l = \boldsymbol{\mu}_t + \boldsymbol{\zeta}_t \odot \boldsymbol{\eta}^l$ . Also,  $p_{\phi_d}(\mathbf{x}_t | \mathbf{z}^l)$  and  $p_{\phi_d}(\mathbf{z}^l)$  are defined in Eqs. (7) and (6). Furthermore,

$$\nabla_{\phi_e} \mathcal{L}_{\phi_e, \phi_d}(\mathbf{x}_t) \approx \frac{1}{L} \sum_{l=1}^L \nabla_{\phi_e} \log p_{\phi_d}(\mathbf{x}_t | \mathbf{Z}^l) + \frac{1}{L} \sum_{l=1}^L \nabla_{\phi_e} \log p_{\phi_d}(\mathbf{Z}^l) + \sum_{k=1}^K \nabla_{\phi_e} \log \zeta_{kt}$$

and

$$\nabla_{\phi_d} \mathcal{L}_{\phi_e, \phi_d}(\mathbf{x}_t) \approx \frac{1}{L} \sum_{l=1}^L \nabla_{\phi_d} \log p_{\phi_d}(\mathbf{x}_t | \mathbf{Z}^l) + \frac{1}{L} \sum_{l=1}^L \nabla_{\phi_d} \log p_{\phi_d}(\mathbf{Z}^l).$$

---

**Algorithm 1** Derive data-driven knots

---

**Input:**  $\kappa$ : number of possible clusters from each time replicate

$\{\mathbf{x}_t : t = 1, \dots, n_t\}$ : observed  $n_t$  spatial replicates

$\{\mathbf{s}_j : j = 1, \dots, n_s\}$ : coordinates of the observed sites in the domain  $\mathcal{S} \forall \dagger$

$u$ : a high quantile level between 0 and 1

$\lambda$ : minimum distance between knots

**Result:**

$K$ : number of data-driven knots

$\{\tilde{\mathbf{s}}_1, \dots, \tilde{\mathbf{s}}_K\}$ : the coordinates of data-driven knots

$r$ : basis function radius shared by all knots

$x^* \leftarrow$   $u$ th quantile of the concatenated vector  $(\mathbf{x}_1^T, \dots, \mathbf{x}_{n_t}^T)^T$ ; // A high threshold

$Knots \leftarrow$  list(); // Empty list for the chosen knot locations

**for**  $t \leftarrow 1, n_t$  **do**

$\mathcal{E}_t \leftarrow$  where( $\mathbf{x}_t > x^*$ ); // Indices of the locations exceeding the threshold

$wss\_vec \leftarrow$  repeat(NA,  $\kappa$ ); // Vector for the total within-cluster sums of squares

**for**  $nclust \leftarrow 1, \kappa$  **do**

$init\_centers \leftarrow$  sample( $\{\mathbf{s}_j : j \in \mathcal{E}_t\}$ ,  $nclust$ ); //  $nclust$  initial centers

$res\_tmp \leftarrow$  kmeans( $\{\mathbf{s}_j : j \in \mathcal{E}_t\}$ ,  $init\_centers$ ); // [Hartigan and Wong \(1979\)](#)

$wss\_vec[nclust] \leftarrow res\_tmp["tot.withinss"]$ ;

**end**

$best\_nclust \leftarrow$  which.max( $wss\_vec$ ); // Determine the best number of clusters

$init\_centers \leftarrow$  sample( $\{\mathbf{s}_j : j \in \mathcal{E}_t\}$ ,  $best\_nclust$ );

$res \leftarrow$  kmeans( $\{\mathbf{s}_j : j \in \mathcal{E}_t\}$ ,  $init\_centers$ );

$Knots \leftarrow$  append( $Knots$ ,  $res["centers"]$ ); // Cluster centers as knots

**end**

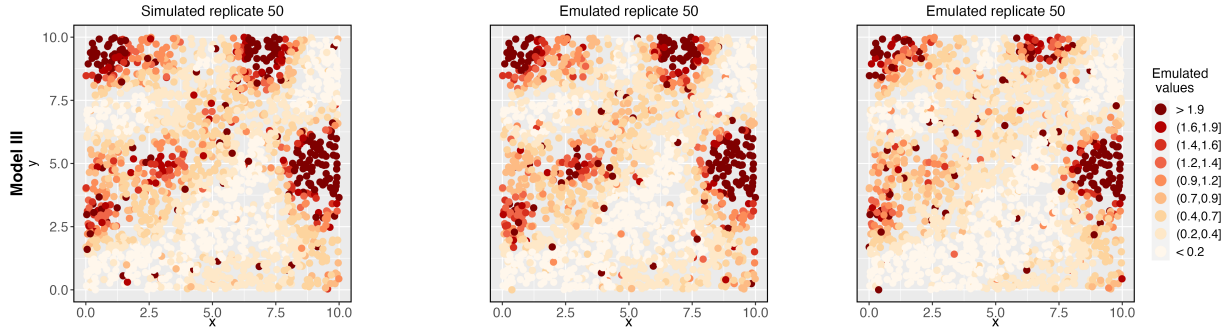
$Knots \leftarrow$  remove points from  $Knots$  so that all knots are no closer than  $\lambda$ ;

$K \leftarrow$  length( $Knots$ );

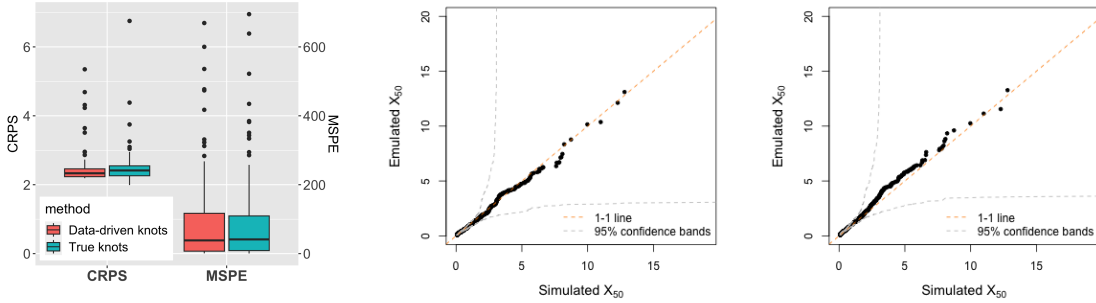
$\{\tilde{\mathbf{s}}_1, \dots, \tilde{\mathbf{s}}_K\} \leftarrow Knots$ ;

$r \leftarrow$  the minimum radius such that any  $\mathbf{s} \in \mathcal{S}$  is covered by at least one basis function.

---



(a) Input replicate at time 50      (b) Emulation with the true knots      (c) Emulation with the data-driven knots



(d) Spatial predictions      (e) QQ-plot with the true knots      (f) QQ-plot with the data-driven knots

Figure D.1: Comparing the emulation results from initializing the XVAE with the true knots and data-driven knots for data simulated from Model III.

## D.2 Effect of knot locations

Algorithm 1 outlines how we derive the data-driven knots. First, we perform  $k$ -means clustering on each time replicate of the data input to determine how many clusters of high values ( $u > 0.95$ ) there are, and we then train XVAE with  $K$  being the number of clusters combined for all time replicates. Second, the cluster centroids are used as knot locations  $\{\tilde{\mathbf{s}}_1, \dots, \tilde{\mathbf{s}}_K\}$ . To initialize  $\Omega$  (defined in Eq. (D.3)) using the Wendland basis functions  $\omega_k(\mathbf{s}, r) = \{1 - d(\mathbf{s}, \tilde{\mathbf{s}}_k)/r\}_+^2$ ,  $k = 1, \dots, K$ , we pick  $r$  by looping over clusters and calculating the Euclidean distance of each point within one cluster from its centroid, and we set the maximum of all distances as the initial  $r$ . If  $r$  is not large enough for all  $\omega_k(\mathbf{s}, r)$  to cover the entire spatial domain, we gradually increase  $r$  until the full coverage is met.

Figure D.1 displays the results from emulating the data set simulated from Model III while initializing the weights differently using the true knots and the data-driven knots. Figures D.1(b) and D.1(c) show one emulation replicate from the decoder for the 50th time replicate. We see that both figures exhibit a striking resemblance to the original simulation,

and from visual examination, we can see little difference in the quality of the emulations. Figure D.1(d) compares the spatial predictions on the 100 holdout locations from the two emulations. The CRPS and MSPE values are again very similar for emulations based on the true knots and data-driven knots.

Figures D.1(e) and D.1(f) compare the simulated and emulated spatial fields of the 50th replicate by plotting their quantiles against each other (when pooling the spatial data into the same plot). We see that both emulations align very well with the simulated data set. Although this might not be the most appropriate way of evaluating the quality of the emulations because there is spatial dependence and non-stationarity within each spatial replicate, QQ-plots still provide value in determining whether the spatial distribution is similar at all quantile levels, which is complementary to the empirical  $\chi_{ij}(u)$  described in Section 2.2.

Overall, Figure D.1 demonstrates that emulation based on data-driven knots performs similarly to using the true knots. This justifies applying the XVAE on a data set stemming from a misspecified model (i.e., Models I or V, for which the data-generating process does not involve any Wendland basis functions). Thus, we will use the XVAE with data-driven knots in all remaining simulation experiments and the real data application.

### D.3 Stochastic gradient descent optimization

A major advantage of approximating the ELBO as presented in Eq. (2) lies in the ability to perform joint optimization over all parameters ( $\phi_e$  and  $\phi_d$ ) using stochastic gradient descent (SGD). This optimization is efficiently implemented using a tape-based automatic differentiation module called `autograd` within the R package `torch` (Falbel and Luraschi, 2023). Built on PyTorch, this package offers rapid array computation, leveraging robust GPU acceleration for enhanced computational efficiency. It stores all the data inputs and VAE parameters in the form of `torch` tensors, which are similar to R multi-dimensional arrays but are designated for fast and scalable matrix calculations and differentiation.

Algorithm 2 outlines the pseudo-code for the ELBO optimization of our XVAE. As the ELBO is constructed within each iteration of the SGD algorithm, the `autograd` module of `torch` tracks the computations (i.e., linear operations and ReLU activation on the tensors) in all layers of the encoding/decoding neural networks, and then performs the reverse-mode automatic differentiation via a backward pass through the graph of tensor operations to obtain the partial derivatives or the gradients with respect to each weight and bias parameter (Keydana, 2023).

The iterative steps of Algorithm 2 involve advancing in the direction of the gradients on the ELBO  $\sum_{t=1}^{n_t} \mathcal{L}_{\phi_e, \phi_d}(\mathbf{x}_t)$  (or a minibatch version  $\sum_{t \in \mathcal{M}} \mathcal{L}_{\phi_e, \phi_d}(\mathbf{x}_t)$ ,  $\mathcal{M} \subset \{1, \dots, n_t\}$ ). This is guided by a user-defined learning rate  $\nu > 0$ . To enhance stability, a convex combination of the prior update and the current gradient incorporates a momentum parameter  $\zeta_m$  into the optimization process (Polyak, 1964). Notably, our experiments indicate that setting the number of Monte Carlo samples  $L$  to 1 suffices, provided the minibatch size  $|\mathcal{M}|$  is adequately large, aligning with the recommendation by Kingma and Welling (2013). Upon successful training of  $\phi_e$  and  $\phi_d$ , the encoder and decoder can be efficiently executed

as needed. Leveraging the amortized nature of our estimation approach, these processes generate an ensemble of numerous samples, all originating from the same (approximate) distribution as the spatial inputs.

Importantly, our XVAE algorithm can scale efficiently to massive spatial data sets. The existing max-stable, inverted-max-stable, and other spatial extremes models are limited to applications with less than approximately 1,000 locations using a full likelihood or Bayesian approach; see Section A for more details on these alternative approaches. By contrast, our approach can fit a globally non-stationary spatial extremes process, with parameters evolving over time, to a data set of unprecedented spatial dimension of more than 16,000 locations, and also facilitates data emulation in such dimensions. See Section 4 for details.

## D.4 Finding starting values

In finding a reasonable starting values of parameters in XVAE, we choose  $\alpha_0 = 1/4$  and  $\tau = 1$  for the white noise process, and  $\alpha = 1/2$  for the latent exponentially-tilted PS variables. From Eq. (4),  $(\mathbf{y}_1^{1/\alpha_0}, \dots, \mathbf{y}_{n_t}^{1/\alpha_0}) = \mathbf{\Omega}^{1/\alpha}(\mathbf{z}_1, \dots, \mathbf{z}_{n_t})$ , in which  $\mathbf{\Omega}$  is defined in Eq. (D.3). Since  $\{\epsilon_t(\mathbf{s}) : t = 1, \dots, n_t\}$  are treated as error processes, we have  $\mathbf{x}_t \approx \mathbf{y}_t$  and thus a good approximation for  $\mathbf{z}_t$  can be obtained via projection:

$$\hat{\mathbf{z}}_t \approx \{(\mathbf{\Omega}^{\frac{1}{\alpha}})^T \mathbf{\Omega}^{\frac{1}{\alpha}}\}^{-1} (\mathbf{\Omega}^{\frac{1}{\alpha}})^T \mathbf{x}_t^{\frac{1}{\alpha_0}}, \quad t = 1, \dots, n_t.$$

We use QR decomposition to solve the following linear system to get the initial value  $\mathbf{W}_1^{(0)}$ :  $(\hat{\mathbf{z}}_1, \dots, \hat{\mathbf{z}}_{n_t})^T = (\mathbf{x}_1, \dots, \mathbf{x}_{n_t})^T \mathbf{W}_1^T$ . Also, set  $\mathbf{b}_1^{(0)} = (0, \dots, 0)^T$ . The initial values of  $\mathbf{h}_{1,t}$  in Eq. (D.1) satisfy  $\mathbf{h}_{1,t} \approx \hat{\mathbf{z}}_t$ ,  $t = 1, \dots, n_t$ .

Furthermore, we set  $\mathbf{W}_2^{(0)}$  and  $\mathbf{W}_4^{(0)}$  to be identity matrices. All remaining parameters, both variational and generative, were initialized by random sampling from  $N(0, 0.01)$ .

To optimize the ELBO following the steps outlined in Algorithm 2, we monitor the convergence of the ELBO via calculating the difference in the average ELBO values in the latest 100 iterations (or epochs) and the 100 iterations before that. Once the difference is less than  $\delta = 10^{-6}$ , we stop the stochastic gradient search.

## E Additional figures from the simulation study

We show additional figures that are complementary to those included in Section 3. Figure E.1 displays the simulated data sets from Models I, II, IV and V and their emulated fields using both XVAE and hetGP. See Figure 2 for comparison for Model III. Figure E.2 displays QQ-plots from the spatial data to compare the overall distributions of the simulated and emulated data sets. Figure E.3 compares the empirically estimated  $\chi_h(u)$  as described in Section 2.2 from the data replicates simulated from Models I, II, IV and V and their emulations at three different distances  $h = 0.5, 2, 5$  under the working assumption of stationarity. Figure E.4 shows the estimates of  $\text{ARE}_\psi(u)$  defined in Eq. (13),  $\psi = 0.05$ , for both simulations and XVAE emulations under Models I, II, IV and V. See Figure 4 for

---

**Algorithm 2** Stochastic Gradient Descent with momentum to maximize the ELBO defined in Eq. (2). We set  $|\mathcal{M}| = n_t$  and  $L = 1$  in our experiments.

---

**Input:** Learning rate  $\nu > 0$ , momentum parameter  $\zeta_m \in (0, 1)$ , convergence tolerance  $\delta$

$\{\mathbf{x}_t : t = 1, \dots, n_t\}$ : observed  $n_t$  spatial replicates

$q_{\phi_e}(\mathbf{z}_t | \mathbf{x}_t)$ : inference model

$p_{\phi_d}(\mathbf{x}_t, \mathbf{z}_t)$ : generative data model

**Result:** Optimized parameters  $\phi_e, \phi_d$

$j \leftarrow 0$ ;

$K \leftarrow$  Number of data-driven knots;

$\{\tilde{\mathbf{s}}_1, \dots, \tilde{\mathbf{s}}_K\} \leftarrow$  Specify knot locations; // See Section D.2 for details

$r \leftarrow$  Basis function radius shared by all knots;

$(\phi_e^{(j)}, \phi_d^{(j)})^T \leftarrow$  Initialized parameters; // See Section D.4 for details

$\mathbf{v} \leftarrow \mathbf{0}$ ; // Velocity

$\mathbf{L} \leftarrow \text{repeat}(-\text{Inf}, 200)$ ; // A vector of 200 negative infinite values

**while**  $|\text{mean}\{\mathbf{L}[(j - 200) : (j - 101)]\} - \text{mean}\{\mathbf{L}[(j - 100) : j]\}| > \delta$  **do**

$\mathcal{M} \sim \{1, \dots, n_t\}$ ; // Indices for the random minibatch

$\eta_{kt} \stackrel{\text{i.i.d.}}{\sim} \text{Normal}(0, 1)$ ,  $k = 1, \dots, K$ ,  $t \in \mathcal{M}$ ; // Reparameterization trick

**for**  $t \in \mathcal{M}$  **do**

$(\boldsymbol{\mu}_t^T, \log \boldsymbol{\zeta}_t^T)^T \leftarrow \text{EncoderNeuralNet}_{\phi_e^{(j)}}(\mathbf{x}_t)$ ;

$\mathbf{z}_t \leftarrow \boldsymbol{\mu}_t + \boldsymbol{\zeta}_t \odot \boldsymbol{\eta}_t$ ;

$(\boldsymbol{\alpha}_t, \boldsymbol{\gamma}_t^T)^T \leftarrow \text{DecoderNeuralNet}_{\phi_d^{(j)}}(\mathbf{z}_t)$ ;

        Calculate  $q_{\phi_e^{(j)}}(\mathbf{z}_t | \mathbf{x}_t)$ ,  $p_{\phi_d^{(j)}}(\mathbf{x}_t | \mathbf{z}_t)$  and  $p_{\phi_d^{(j)}}(\mathbf{z}_t)$ ; // See Eq. (5)-(6)

**end**

    Obtain the ELBO  $\mathcal{L}_{\phi_e^{(j)}, \phi_d^{(j)}}(\mathcal{M}) = \sum_{t \in \mathcal{M}} \mathcal{L}_{\phi_e^{(j)}, \phi_d^{(j)}}(\mathbf{x}_t)$  and its gradients  $\mathbf{J}_{\mathcal{L}} =$

$\{\nabla_{\phi_e, \phi_d} \mathcal{L}_{\phi_e, \phi_d}(\mathcal{M})\}(\phi_e^{(j)}, \phi_d^{(j)})$ ;

    Compute velocity update:  $\mathbf{v} \leftarrow \zeta_m \mathbf{v} + \nu \mathbf{J}_{\mathcal{L}}$ ;

    Apply update:  $(\phi_e^{(j+1)}, \phi_d^{(j+1)})^T \leftarrow (\phi_e^{(j)}, \phi_d^{(j)})^T + \mathbf{v}$ ;

$\mathbf{L} \leftarrow (\mathbf{L}^T, \mathcal{L}_{\phi_e^{(j)}, \phi_d^{(j)}}(\mathcal{M}))^T$ ; // Add the latest ELBO value to the vector  $\mathbf{L}$

$j \leftarrow j + 1$ ;

**end**

---

$\chi_h(u)$  and  $\text{ARE}_\psi(u)$  estimates for Model III. Lastly, Figure E.5 shows coverage probabilities of  $\{\gamma_{kt} : k = 1, \dots, K\}$  for  $t = 1$  from fitting Model III. Coverage probabilities when  $\gamma_k = 0$  are poor, though upper bounds of credible intervals are consistently less than  $10^{-6}$ .

## F Red Sea Dataset

### F.1 Removing seasonality

For any site  $\mathbf{s}_j$ , we combine daily observations across all days as a vector and denote it by  $\mathbf{v}_j = (v_{j1}, \dots, v_{jN})^T$  where  $N = 11,315$  is the number of days between 1985/01/01 and 2015/12/31. Following Huser (2021), we remove the seasonality from the Red Sea SST daily records at a fixed  $\mathbf{s}_j$  via subtracting the overall trend averaged within its neighborhood of radius  $r = 30$  km, and then we repeat the same procedure for every other location.

More specifically, denote the index set of all location with the neighborhood of  $\mathbf{s}_j$  by  $\mathcal{N}_j = \{i : \|\mathbf{s}_i - \mathbf{s}_j\| < r, i = 1, \dots, n_s\}$ . To get rid of the seasonality in  $\mathbf{v}_j$ , we first concatenate all records in the neighborhood  $\{\mathbf{v}_i : i \in \mathcal{N}_j\}$  to get a flattened response vector  $\mathbf{V}_j$ ; that is,  $\mathbf{V}_j = (\mathbf{v}_{i_1}^T, \mathbf{v}_{i_2}^T, \dots, \mathbf{v}_{i_{|\mathcal{N}_j|}}^T)^T$  where  $\{i_1, \dots, i_{|\mathcal{N}_j|}\}$  include all elements of  $\mathcal{N}_j$ . Thus, the length of the vector  $\mathbf{V}_j$  is  $|\mathcal{N}_j| \times N$ . Second, we construct the matrix  $\mathbf{M} = (\mathbf{1}_N, \mathbf{t}, \mathbf{B}_{N \times 12})$ , where  $\mathbf{t} = (1, \dots, N)^T$  is used to capture linear time trend and the columns of  $\mathbf{B}$  are 12 cyclic cubic spline bases defined over the continuous interval  $[0, 366]$  evaluated at  $1, \dots, N$  modulo 365 or 366 (i.e., the day in the corresponding year). These basis functions use equidistant knots over of  $[0, 366]$  that help capturing the monthly-varying features. Then, we vertically stack the matrix  $\mathbf{M}$  for  $|\mathcal{N}_j|$  times to build the design matrix  $\mathbf{M}_j$ . Through simple linear regression of  $\mathbf{V}_j$  on  $\mathbf{M}_j$ , we get the fitted values  $\hat{\mathbf{V}}_j = (\hat{\mathbf{v}}_{i_1}^T, \hat{\mathbf{v}}_{i_2}^T, \dots, \hat{\mathbf{v}}_{i_{|\mathcal{N}_j|}}^T)^T$ .

To model the residuals  $\mathbf{V}_j - \hat{\mathbf{V}}_j$ , we only use an intercept and a time trend which are the first two columns of  $\mathbf{M}_j$  (denote as  $\mathbf{M}_j^\sigma$ ). The model for the residuals is

$$\begin{aligned} \mathbf{V}_j - \hat{\mathbf{V}}_j &\sim N(\mathbf{0}, \text{diag}(\boldsymbol{\epsilon}_j^2)), \\ \log \boldsymbol{\epsilon}_j &= \mathbf{M}_j^\sigma \times (\beta_1, \beta_2)^T. \end{aligned}$$

Hence we can estimate parameters  $(\beta_1, \beta_2)^T$  via optimizing the multivariate normal density function, i.e.,

$$(\hat{\beta}_1, \hat{\beta}_2)^T = \underset{(\beta_1, \beta_2)^T}{\text{argmin}} \left\{ -\frac{1}{2} \log \mathbf{1}^T \boldsymbol{\epsilon}_j^2 - \frac{1}{2} (\mathbf{V}_j - \hat{\mathbf{V}}_j)^T \text{diag}(\boldsymbol{\epsilon}_j^{-2}) (\mathbf{V}_j - \hat{\mathbf{V}}_j) \right\}.$$

Let  $\hat{\boldsymbol{\epsilon}}_j = \exp\{\mathbf{M}_j^\sigma \times (\hat{\beta}_1, \hat{\beta}_2)^T\} \equiv (\hat{\boldsymbol{\epsilon}}_{i_1}^T, \hat{\boldsymbol{\epsilon}}_{i_2}^T, \dots, \hat{\boldsymbol{\epsilon}}_{i_{|\mathcal{N}_j|}}^T)^T$ . Note that in defining the neighborhood of site  $\mathbf{s}_j$ , we also include the  $j$ th site. By an abuse of notation, we denote the fitted values corresponding to the  $j$ th site by  $\hat{\mathbf{v}}_j$  and  $\hat{\boldsymbol{\epsilon}}_j$ , which correspond to the mean trend and residual standard deviations at site  $\mathbf{s}_j$ , respectively. Finally, the daily records at



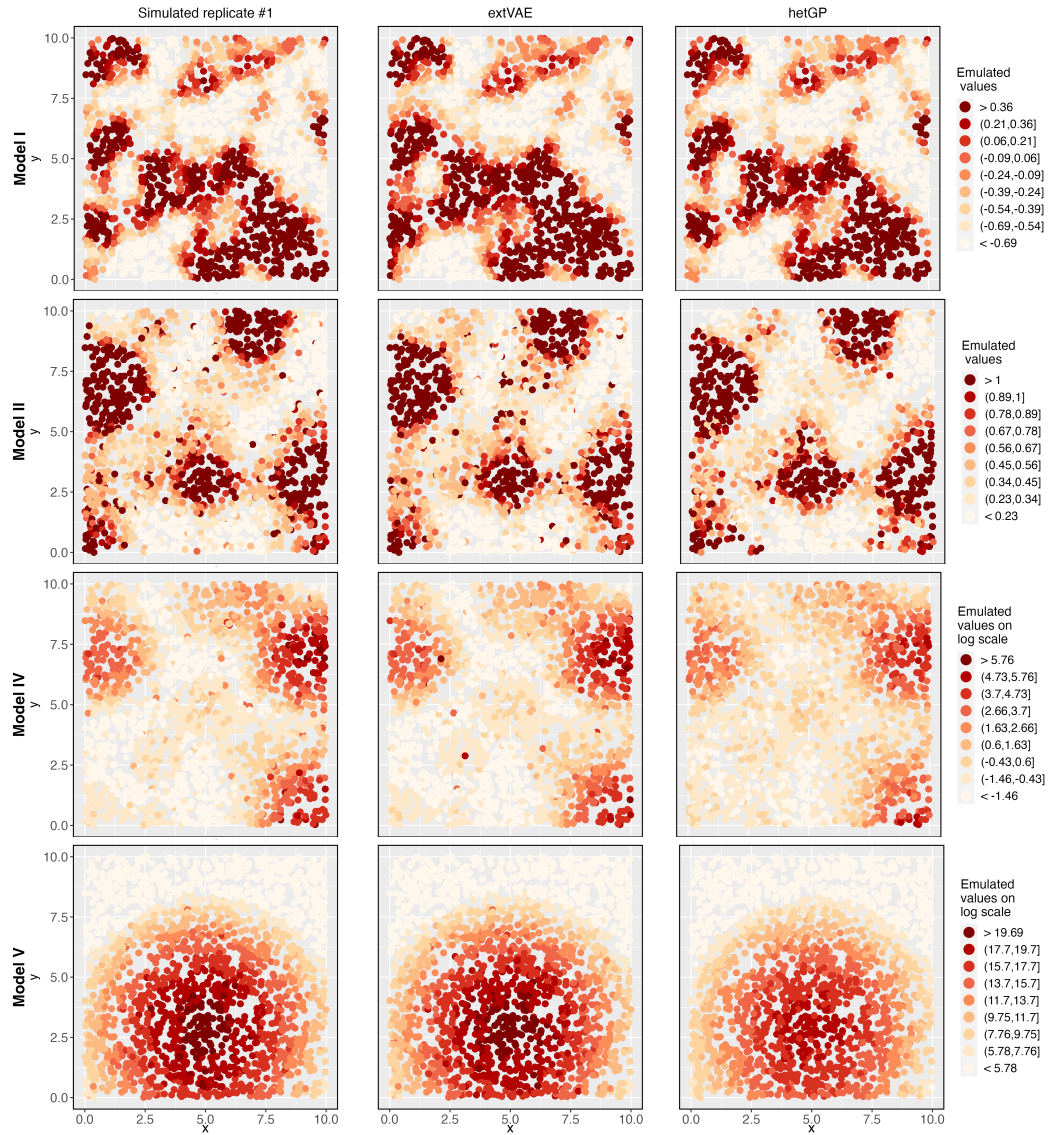


Figure E.1: Simulated data sets (left column) and emulated fields (XVAE, middle column; hetGP, right column) from Models I, II, IV and V (top to bottom). In all cases, we use data-driven knots for emulation using XVAE. See Figure 2 for comparison for Model III.

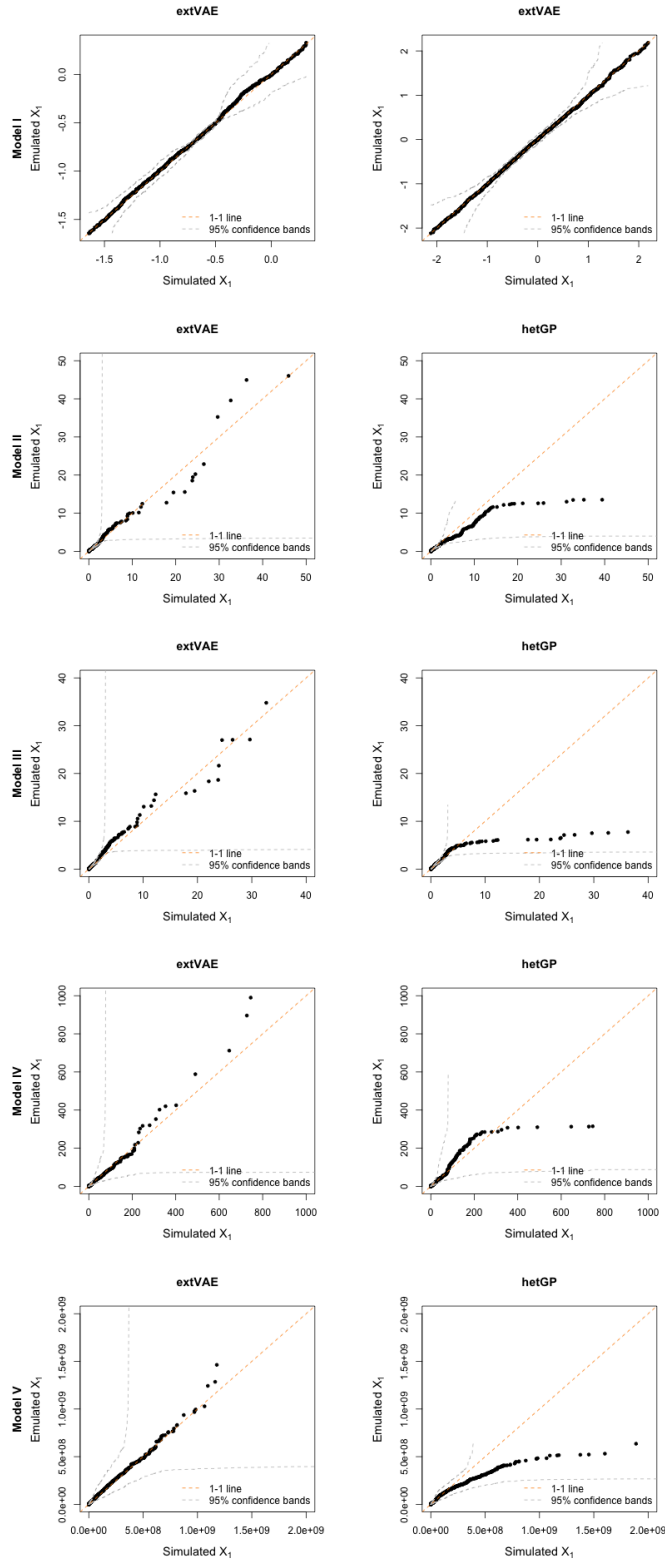


Figure E.2: QQ-plots comparing simulated data sets and emulated fields from XVAE (left), and hetGP (right) based on Models I–V (top to bottom).

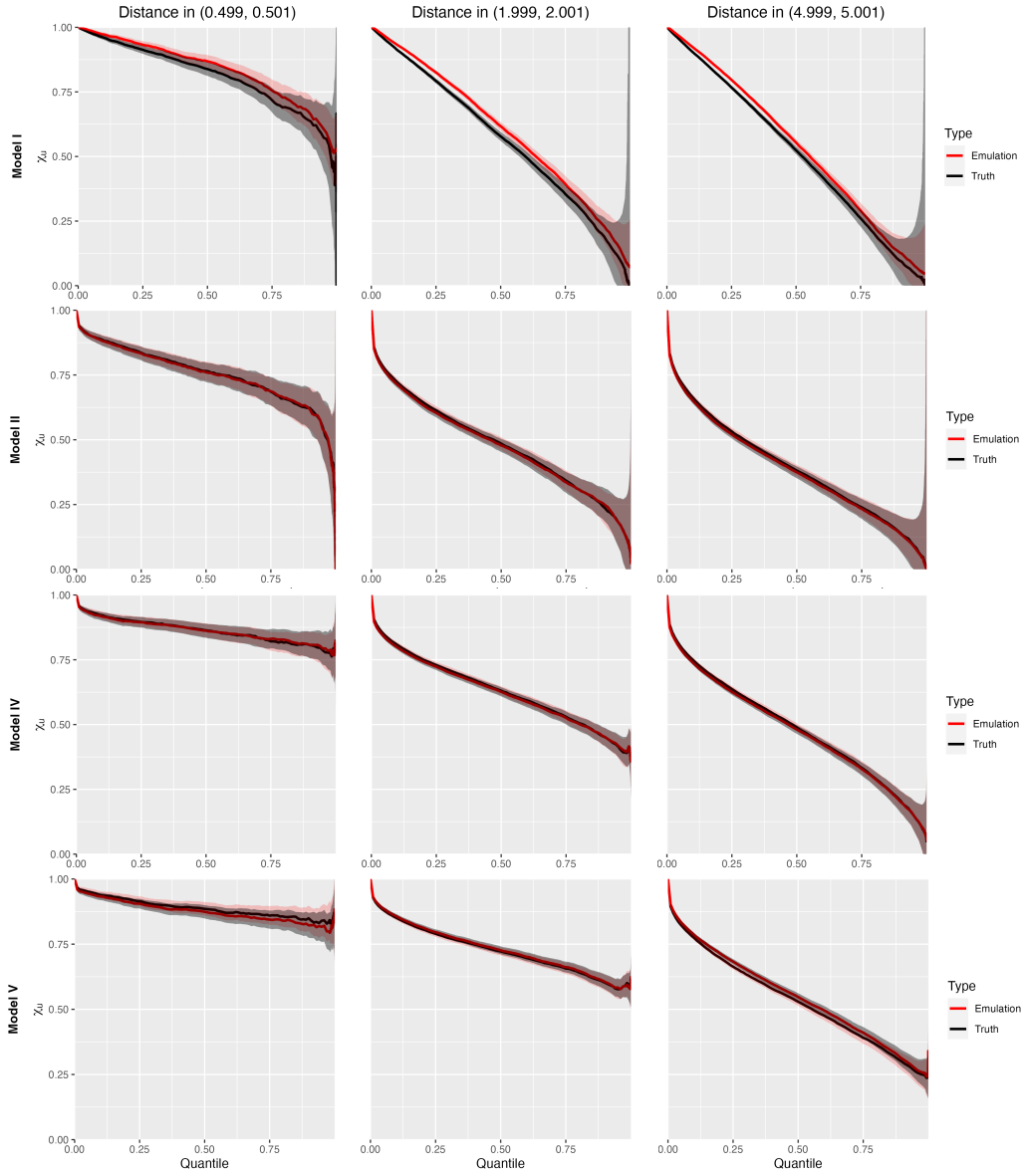


Figure E.3: The empirically-estimated tail dependence measure  $\chi_h(u)$  at  $h = 0.5$  (left), 2 (middle), 5 (right) for Models I, II, IV and V (top to bottom), based on simulated (black) and XVAE emulated (red) data. See Figure 4 for  $\chi_h(u)$  estimates for Model III.

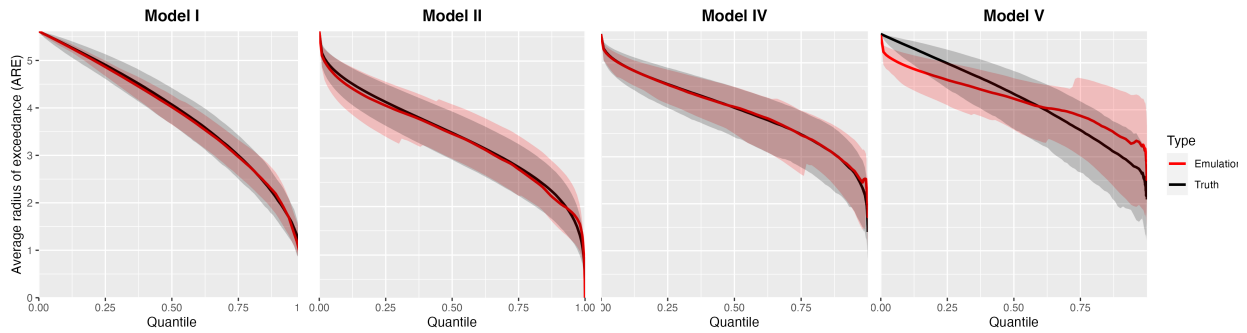


Figure E.4: Estimates of  $\text{ARE}_\psi(u)$ ,  $\psi = 0.05$ , for both simulations (black) and XVAE emulations (red) under Models I, II, IV and V (left to right). See the right panel of Figure 4 for  $\text{ARE}_\psi(u)$  estimates for Model III.

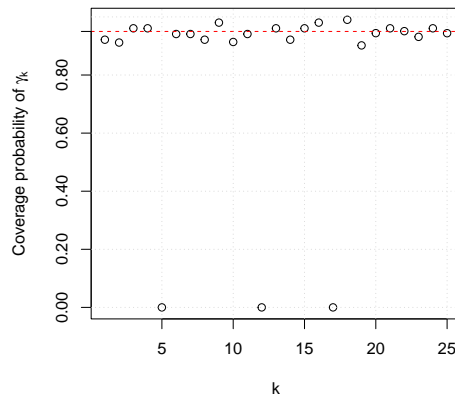


Figure E.5: Coverage probabilities for each of the parameters  $\gamma_k$ ,  $k = 1, \dots, K = 25$ , from emulating 100 simulated data sets of Model III, in which  $n_s = 2,000$  and  $n_t = 100$ . The nominal levels of the credible intervals are 0.95 (red dashed line). Zero probabilities correspond to  $\gamma_k = 0$ ,  $k = 5, 12, 17$ .

$\mathbf{s}_j$  can be de-trended by calculating

$$\mathbf{v}_j^* = \frac{\mathbf{v}_j - \hat{\mathbf{v}}_j}{\hat{\mathbf{e}}_j}, \quad (\text{F.1})$$

in which the subtraction and division are done on a elementwise basis. We repeat the procedure described above to remove the seasonal variability from all other locations.

## F.2 Marginal distributions of the monthly maxima

After removing seasonality by normalization (see Eq. F.1), we extract monthly maxima from  $\mathbf{v}_j^*$  at site  $\mathbf{s}_j$  and denote them as  $\mathbf{m}_j = (m_{j1}, \dots, m_{jn_t})$ , in which  $n_t = 372$  is the number of months between 1985/01/01 and 2015/12/31 and  $j = 1 \dots, n_s$ . Before applying our proposed model, we need to find a distribution which fits the monthly maxima well so we can transform the data to the Pareto-like distribution shown in Eq. (10). Given prior experience in analyzing monthly maxima, we propose two candidate distributions: the generalized extreme value (GEV) distribution and the general non-central  $t$  distribution. To choose between them, we choose to perform  $\chi^2$  goodness-of-fit tests due to its flexibility in choosing the degrees of freedom as well as the size of intervals.

The  $\chi^2$  goodness-of-fit test at a site  $\mathbf{s}_j \in \mathcal{S}$  proceeds as follows. First, we calculate the equidistant cut points within the range of all monthly maxima at  $\mathbf{s}_j$  to get  $n_I$  intervals. Second, we count the number of monthly maxima falling within each interval and denote them by  $O_i$  ( $i = 1, \dots, n_I$ ). Third, we fit the GEV and  $t$  distributions to the block maxima series at  $\mathbf{s}_j$  to get the parameter estimates. Then the expected frequencies  $E_i$  ( $i = 1, \dots, n_I$ ) is calculated by multiplying the number of monthly maxima at each site (i.e.,  $n_t$ ) by the probability increment of the fitted GEV or  $t$  distribution in each interval (denoted by  $p_i$ ). Treating the frequencies as a multinomial distribution with  $n_t$  trials and  $n_I$  categories, we can derive the generalized likelihood-ratio test statistic for the null hypothesis  $H_0$  that  $(p_1, \dots, p_{n_I})^T$  are the true event probabilities. Specifically, under the null hypothesis  $H_0$ , Wilk's Theorem guarantees

$$\sum_{i=1}^{n_I} O_i \log(O_i/E_i) \xrightarrow{d} \chi_\nu^2 \text{ as } n_t \rightarrow \infty,$$

in which  $\nu = n_I - 4$  when  $H_0$  corresponds to the GEV model which has three parameters (i.e., location, scale, and shape) and  $\nu = n_I - 3$  when  $H_0$  corresponds to the  $t$  model which has two parameters (i.e., non-centrality parameter and degrees of freedom). Since  $n_t = 372$  in the Red Sea SST data, we can safely assume that the asymptotic distribution is a good approximation of the true distribution under  $H_0$ , which is then used to calculate the  $p$ -value to evaluate the goodness-of-fit.

We repeat the procedure and obtain a  $p$ -value for each location. Figure F.1 shows the spatial maps for  $p$ -values along with the binary maps signifying whether the null hypothesis is accepted or not with significance level 0.05. In Figure F.1(c), the goodness-of-fit tests

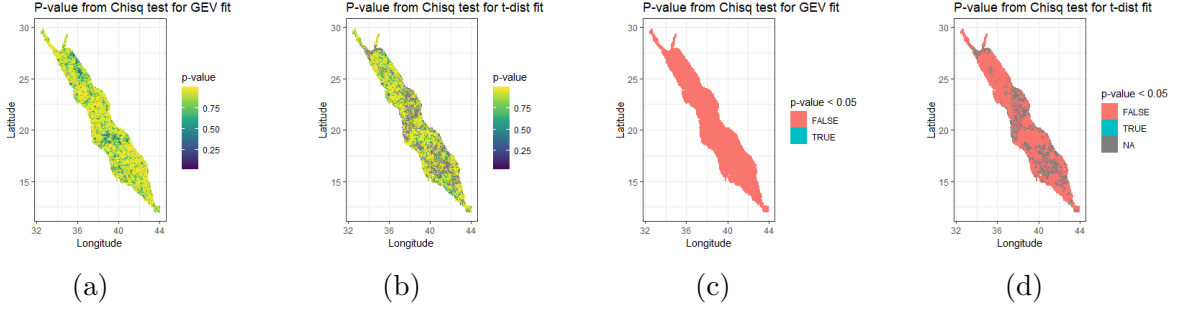


Figure F.1: In the left two panels, we show heatmaps of  $p$ -values from  $\chi^2$  goodness-of-fit tests under the GEV model in (a) and the  $t$  model in (b). In the right two panels, we show binary  $p$ -values maps from  $\chi^2$  goodness-of-fit tests under the GEV model in (c) and the  $t$  model in (d).

result in  $p$ -values greater than 0.05 at all locations, indicating GEV distribution is a good fit for all monthly maxima time series. For the shaded locations in Figure F.1(b) and F.1(d), the `fitdistr(., "t")` function from the MASS package in R failed to converge when optimizing joint  $t$  likelihood, and we were not able to obtain parameter estimates of the  $t$  distribution at these locations which were needed for the subsequent  $\chi^2$  tests. For the locations that have valid fitted  $t$  distributions in Figure F.1(b), the  $p$  values are mostly less than those in Figure F.1(a). This indicates that the GEV distribution, the asymptotic distribution for univariate block maxima, is a better choice to describe the marginal distribution of the monthly maxima, as expected.

### F.3 Marginal transformation

Before applying our model to monthly maxima, certain transformations need to be done to match our marginals in Section 1.3.1. When performing the goodness-of-fit tests, we already obtained the sitewise GEV parameters:  $\mu_j$ ,  $\sigma_j$ , and  $\xi_j$  for  $j = 1, \dots, n_s$ . Since monotonic transformations of the marginal distributions do not alter the dependence structure of the data input, we define  $x_{jt} = F_{jt}^{-1}\{F_{\text{GEV}}(m_{jt}; \mu_j, \sigma_j, \xi_j)\}$ ,  $t = 1, \dots, n_t$ ,  $j = 1, \dots, n_s$ , in which  $F_{jt}$  is the marginal distribution function of  $X_t(\mathbf{s}_j)$  displayed in Eq. (10), the function  $F_{\text{GEV}}(\cdot; \mu_j, \sigma_j, \xi_j)$  is the distribution function of  $\text{GEV}(\mu_j, \sigma_j, \xi_j)$ , and  $m_{jt}$  is the monthly maximum at site  $\mathbf{s}_j$  from  $t^{\text{th}}$  month. Further, we have  $\mathbf{x}_t = (x_{1t}, x_{2t}, \dots, x_{n_s t})^T$ ,  $t = 1, \dots, n_t$ , which will be treated as the response in Algorithm 2. It should be noted that  $F_{jt}$  is defined with the parameters  $\alpha_t$ ,  $\boldsymbol{\gamma}_t^T$  and  $\boldsymbol{\Omega}$ . Recall that the matrix  $\boldsymbol{\Omega}$ , defined in Eq. (D.3), contains the basis function evaluations at all locations. After updating these parameters in each iteration of the stochastic gradient descent algorithm, we need to update the values of  $\{x_{jt} : t = 1, \dots, n_t, j = 1, \dots, n_s\}$  before continuing the next iteration.

## F.4 Empirical $\chi_h(u)$ estimates

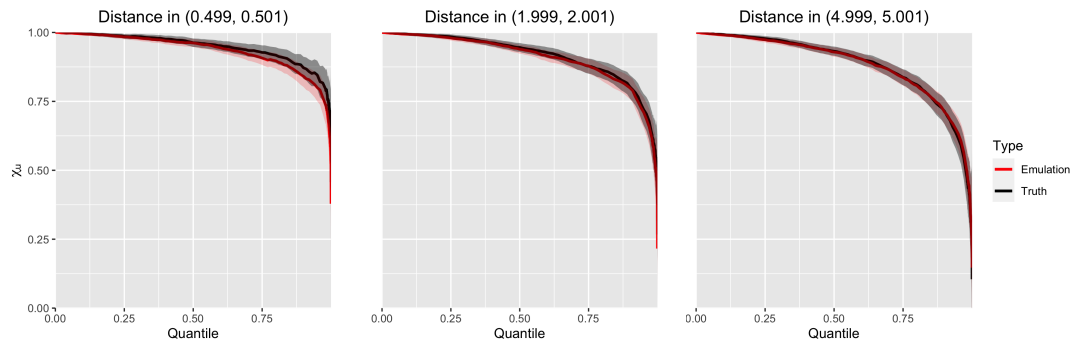


Figure F.2: Empirically-estimated  $\chi_h(u)$  for  $h = 0.5, 2, 5$  ( $\approx 50\text{km}, 200\text{km}, 500\text{km}$ ) for the Red Sea SST monthly maxima (black) and the XVAE emulations (red).